Scalable Spray Deposition of Carbon Nanotube based Electronic Devices

Florin-Cristian Loghin

To my parents Mami & Tati

To my siblings Maria & Francisc

To my family & friends

Thank you for your never-ending support and patience

Abstract

English

In this work, we aim to develop processing techniques for the development and fabrication of spray deposited carbon nanotube (CNT) based devices, in particular thin-film transistors (TFTs) and gas sensors. This goal is separated into smaller sub-goals, namely: the development of a spray deposition process that delivers a stable framework, which can be easily integrated into other existing processes, We initially focus on the development of CNT sprayable ink based with the aid of dispersants. Subsequently a spray deposition process is introduced with the according characterization to provide pristine CNT films on arbitrary samples. Afterwards we pattern and functionalize the prepared films, specifically by means of laser ablation and modification. Next, we present the development and characterization of CNT TFTs followed by the coupling with indium gallium zinc oxide transistors to fabricate functional flexible logic gates and a common source amplifier. Finally, we present a process for the fabrication and characterization of resistive CNT based gas sensors, additionally coupling this with the TFT technology to fabricate chemical field-effect transistors (chemFET).

Deutsch

Ziel dieser Arbeit ist die Entwicklung von Verarbeitungstechniken für die Entwicklung und Herstellung von Bauteilen auf der Basis von aufgesprühten Kohlenstoffnanoröhren (CNT), insbesondere Dünnschichttransistoren (TFTs) und Gassensoren. Dieses Ziel gliedert sich in kleinere Teilziele, nämlich die Entwicklung eines Sprühabscheidungsprozesses, der ein stabiles Gerüst liefert, das sich leicht in andere bestehende Prozesse integriert lässt. Wir konzentrieren uns zunächst auf die Entwicklung von CNT-Sprühtinten auf Basis von Dispergiermitteln. Anschließend wird ein Sprühabscheidungsprozess mit der entsprechenden Charakterisierung eingeführt, um makellose CNT-Filme auf beliebigen Proben bereitzustellen. Anschließend strukturieren und funktionalisieren wir die vorbereiteten Filme gezielt mittels Laserablation und Modifikation. Als nächstes präsentieren wir die Entwicklung und Charakterisierung von CNT-TFTs, gefolgt von der Kopplung mit Indium-Gallium-Zink-Oxid-Transistoren, um funktionelle flexible Logikgatter und einen gemeinsamen Source-Verstärker herzustellen. Schließlich stellen wir ein Verfahren zur Herstellung und Charakterisierung von resistiven CNT-basierten Gassensoren vor, das zusätzlich mit der TFT-Technologie zur Herstellung chemischer Feldeffekttransistoren (chemFET) gekoppelt wird.

Contents

Chapter 1

Introduction

1.1 Background and Motivation

During the last two decades, significant developments in the field of printed and organic electronics have been done with a wide range of focus pertaining but not limited to materials, deposition integration and devices. Key advantages characteristic to the field being low-cost, flexible and in certain areas an environmentally friendlier solution to conventional electronics. In addition, it has also given rise to new devices that were previously not feasible with conventional techniques. Narrowing down the field, printed electronics, in particular solution based organic compounds [1] has found a wide range of applications: thin-film transistors (TFTs) [2], thin conducting films (TCFs) [3], chemical and bio sensors [4], [5], organic photovoltaics (OPVs) [6] as well as organic photo detectors (OPDs) [7].

One specific and unique material in the organic electronics portfolio is the carbon nanotube, CNT for short. CNTs, descriptively described, as a rolled up sheet of graphene exhibit extraordinary properties. Due to these unique properties of CNTs, a wide applicability, as active and passive material in a wide range of applications, can be observed. Two of these applications are TFTs and gas sensors.

While the use for transistors covers most of the electronic world, as they are one of the base building block, the use of gas sensors is similarly important. The detection of foreign particles in the atmosphere is of great interest in various fields, such as environmental pollution, industrial emission control, indoor air quality monitoring and medical diagnostics. Besides real time monitoring and a good sensing performance, miniaturization and portability are key aspects in developing sensor to detect gas analytes in the desired

environment. Due to their large width-to-length ratio, CNTs show great adsorptive capacities. In addition, sensors based on nanomaterials are easy to customize, as altering the size and composition of the material tunes the electrical properties of the nanostructure. Moreover, nanomaterial gas sensors are well suited for the implementation in low-power microelectronic devices.

From a processing point of view a wide range of processes have been employed in the printed electronics world. One such technique is the spray coating. Although spray technology has a variety of applications ranging from humidification to combustion, the more relevant for printed electronics is its use as surface coating. In the last decade, however, due to reasons such as process scaling, the possibility of using all dissolvable materials or the determination of layer thicknesses, the process has gained increasing interest in organic solution-processed devices such as organic solar cells [8]–[14]. The advantage of spray coating is the high throughput and the low material waste for large-area deposition and it is fully roll-to-roll (R2R) compatible, which allows low-cost fabrication of sprayed devices.

In this framework, this thesis hopes to merge the spray coating technology and the unique material properties of CNTs for the development of CNT TFTs, gas sensors and the combination of the two in the form of chemical field effect transistors (chemFETs)

1.2 Outline of the Thesis

In the subsequent chapters, we will dive deeper into multiple facets of spray deposited CNT devices and aim to provide an overview of both various direct applications of such devices as well as processing techniques pertaining to the modification of CNT films.

Chapter 2 provides a brief history of CNTs, how they were discovered as well as the initial developed devices. Further, we will look at the unique characteristics of CNTs and the theoretical phenomenon responsible these characteristics. A short overview of synthesis techniques is also provided as well as purification processes employed. Reviewing state of the art devices, we will gain a better knowledge of what has already been achieved and where this thesis expands on already gained knowledge. Particularly concerning CNT gas sensors and CNT thin-film transistors. The second part of the chapter introduces the key processing techniques employed in this thesis and where these have been successfully applied in the printed electronics world.

Chapter 3 presents our developed framework for the spray deposition process of CNT based devices. The initial challenge is of bringing the CNTs into solution with a time stable ink and a good dispersion reducing bundle width. For this step, we use two dispersing agents in

the form of carboxymethyl cellulose (CMC) and sodium dodectyl sulfate (SDS). There exist a tradeoff between dispersion quality and ease of dispersant removal post deposition. As part of this investigation, an effort is made to improve the dispersion capabilities of SDS due to it being directly removal able with deionized water. In order to guarantee a pristine film post deposition free of unwanted dispersant, we investigated our processes with the aid of field enhanced scanning electron microscopy, X-ray photoelectron spectroscopy and Raman spectroscopy. Doing so allows us to make measurement-backed statements as to the complete removal of dispersants. In addition we will also show that annealing treatments allow for the desorption of unwanted gas molecules adsorbed during the post deposition treatment are desorbed.

The following chapter attempts to show that with the aid of a femtosecond laser we can reduce some of the shortcoming that are generated by our approach in using randomly aligned CNT networks. One such shortcoming is inherent to the spray deposition as to it being a coating technique, which results in non-sharply defined areas. The second shortcoming is that due to the random nature of the networks we have both undesired CNT alignment, which increase effective channel length as well as introducing tube-tube resistance that affect device performance, as well as differing CNT electrical behavior in the shape of semiconducting as well as metallic. In order to address these issues we initially investigate the interaction between laser and CNT film in both a single as well as multi pulse regime as to better understand the interaction. From these results, we then develop a process to pattern CNT films effectively doing so alleviating the drawback of the coating technique. A unique aspect of the femtosecond laser is its interaction with the CNT film while polarized. Investigating this effect allows us to show that it is possible to selectively ablate CNT based on the angle to the polarization plane of the laser. This is possible in part due to the unique nature of the femtosecond laser as to the reduced energy provided to the system but as well due to the high aspect ratio of the CNTs and their small diameter. This technique allows for a quasi-post-deposition alignment of CNTs. Such alignment was previously restricted to direct growth of CNTs by means of chemical vapor deposition. A further characteristic unique to CNT in relation to laser ablation is that due to the electrical behavior being defined by the radii of the CNT and arrangement of carbon atoms along the tube, they exhibit differing absorption spectra. As such we will show as a proof of concept that it is possible to selectively ablate, for example metallic CNTs from a random network.

Moving away from patterning and functionalizing the film we will look at specific devices. In the first case: TFTs. In chapter 5, we will present our concept for CNT TFTs. Initially a short overview of general organic TFTs (OTFTs) is given and then the particulars than pertain to CNT TFTs. We will then introduce I-V characteristics for OTFTs and key characteristics defining figure of merits such as field effect mobility, transconductance and subthreshold swing. Following the theoretical aspects, we will introduce our fabrication

protocol for CNT TFTs. To highlight the robustness of our process we will investigate the fabricated transistors both in terms of yield, homogeneity and transistor performance. In order to better understand the critical parameters of our process we will also investigate the dependence of transistor behavior on the CNT density. As this point, we will also introduce our newly developed SDS based ink as to show its feasibility in comparison to the CMC process, again displaying the device performance and distribution. In the final section of the chapter, we will demonstrate that the proposed process is easy to integrate into existing more demanding possesses. As such, we will present the results of combining our technology with that of a collaboration partner in fabricating flexile CMOS structures starting with basic gate structures. We will show the mechanical stability and resistance of our devices. Finally, we will show a record setting flexible common source amplifier.

In chapter 6 of this thesis, we will look at the second focal device of this thesis namely CNT based gas sensors. In this chapter, we will present the design and fabrication of CNT based gas sensors in both a resistive configuration as well as chemFET configuration. Initially we will describe the interaction between CNTs and gas molecules pertaining specifically to the electrical properties. We summarize what has currently been presented in literature as the possible mechanisms for interaction. The initial fabrication will focus on resistive devices. For the architecture, we will use interdigitated electrodes and will test our fabricated devices when exposed to ammonia and carbon dioxide. We will show the long-term stability of our devices over a period of four years. In an attempt to reduce the cost of our sensors as well as increase functionality we will show the efforts in fabricating full CNT gas sensors and their performance in comparison to metal electrode devices. Before moving on to the chemFETs we will introduce a newly emerging technique in printed electronics. For this, we are using our developed ink in conjuncture with a roller ball pen to directly write gas sensors on poster foil. The results presented show comparable results to previously presented sensors. The second part of the chapter will merge the knowledge gained from the TFTs and the gas sensors to fabricate chemFETs. Here we will develop from ground up both a sensor architecture as well as measuring protocol for the extraction of sensor response. Extracting the response from transistor characteristics such as on-off ratio, threshold voltage, transconductance and sub threshold swing. The results will show a higher sensor response in comparison to the resistive sensors, particularly when investigating the extracted field effective mobility.

Finally, chapter 7 will summarize the findings of the thesis and provide a possible outlook to further investigations.

Chapter 2

CNT Based Electronics

For more than three decades, CNTs are the subject of research and development. Their unique structure equips them with numerous remarkable properties, such as excellent thermal and electrical conductivity. As a result, they are suited for various areas of application, such as energy management, computer science and medical and chemical engineering. There are different production methods enabling low-cost and large-scale synthesis of CNTs. However, the synthesis is still challenging.

In the following sections, we introduce the different types and structures of CNT and discuss three widely used synthesis techniques. Furthermore, we provide a short insight in the topic of purification, which is followed by a section dedicated to the properties of CNTs and comparing them to characteristics of materials, which used to be outstanding in their respective field. The section concludes with a summary of potential fields of application for CNTs.

2.1 General Aspects

CNTs initially aroused public interest in 1991, as the physicist S. Iijima observed the formation of "needle-like tubes" during the synthesis of fullerenes [15]. Fullerenes are spheres of at least 12 pentagonal and several hexagonal aromatic rings of sp^2-hybridized carbon atoms [16]. Different from fullerenes, CNT have a similar structure as graphene, where sp^2- hybridized carbon atoms form hexagonal aromatic rings concatenated into a 2-dimensional honeycomb lattice. The body of a CNT can be envisioned as rolling a graphene

sheet into a cylindrical shape, while the hexagonal rings at the intersection unite smoothly. The caps however are formed of two fullerene semi-spheres with dimensions matching the diameter of the CNT [17]. As body and tips of a CNT are curved, the carbon double bonds (C = C) in the aromatic rings are no longer aligned planar. Therefore, it is presumed that a few are sp^3-hybridized rather than sp^2-hybridized. This could be part of the explanation for the increased reactivity compared to graphene and the unique electrical properties of CNTs [18]

There are two types of CNTs: MWCNT (multi-walled carbon nanotube) and SWCNT. The CNTs synthesized by Iijima were MWCNTs with diameters of a few nanometers [15]. MWCNTs possess at least two shells with different diameters nested into each other [19]. Two years later, in 1993, the synthesis of CNTs with a single shell was reported [20].

The structure of a SWCNT is dependent on the chirality angle Θ and the chiral vector $\overrightarrow{C_h}$= (n,m) that also determine the electrical behavior of the CNT. Θ is measured with respect to the x-axis and specifies how the hexagonal carbon rings are oriented with respect to each other. Feasible Θ are between 0° to 30°. The chiral vector is given by:

$$\vec{C}_h = n \cdot \overrightarrow{a_1} + m \cdot \overrightarrow{a_2} \tag{1}$$

Where $\overrightarrow{a_1}$ and $\overrightarrow{a_2}$ are the graphene lattice vectors and n and m their corresponding length. The names of the three layouts of CNTs are zigzag, armchair and chiral and result from their structural appearance. CNTs with armchair structure are usually metallic, however zigzag and chiral CNTs are either metallic or semiconducting, depending on their chiral vector. As a result about one-third of all CNTs exhibit metallic behavior, while the rest are semiconducting [21], [22]

Compared to SWCNT the structure of MWCNTs is more complex. Generally, there are three layouts of MWCNTs: concentric, herringbone, and bamboo. For further information regarding the structure and properties of MWCNTs see [1],[4]. Due to their complex structure, MWCNTs mostly exhibit metallic behavior due to charge transport being dominated by metallic shells.

2.1.1 Synthesis of CNTs

Since their discovery, the synthesis of CNTs was constantly investigated. Depending on the catalyst and the environmental conditions, CNTs grow either from the tip or from the root, also referred to as tip growth and root growth. Today, the aim is still to find a large-scale but low-cost production method, while controlling purity, selectivity and dispersibility of the CNTs. Besides the type, SWCNT or MWCNT, the production method also determines the

structure and the physical properties of the CNTs [18], [23], [24]. Today various methods are known for the synthesis of CNT. The most commonly used are summarized in the following sections.

Electric Arc Discharge

The electric arc discharge method is well-known for decades, as it is the most common technique to synthesize fullerenes. In this method two graphite electrodes are arranged in a distance of a few mm in an inert atmosphere, usually He or Ar, at high temperatures around 4000K and in the high vacuum regime. A low voltage around 30 - 35 V and high current between 100-150 A is applied, resulting in a current arc between the electrodes. The discharge sublimates the carbon atoms of the anode, which subsequently accumulate at the surface of the cathode and the reactor walls. Up to 70% of the deposits on the cathode can be CNTs, the remaining residues are graphitic nanoparticles such as fullerenes and graphene sheets. In contrast to the rod shaped deposit on the cathode, the soot condensing at the reactor walls is mainly composed of graphitic by-products [23]. The electric arc discharge method also enables the synthesis of MWCNTs by vaporizing pure graphitic electrodes. Filling the anode with a metal catalyst, e.g. Fe, Co or Ni and graphite powder generates SWCNTs. Here the function of the catalyst is similar to a scaffold. Generally, CNT growth in the electric arc seems to favor the chiral structure rather than the armchair or zigzag texture. Furthermore, the lack of catalyst nanoparticles at the tips suggest a root growth of the tubes, however growth mechanisms of CNTs are still under investigation [25]. Quality and quantity of the nanotubes are dependent on the experimental setup and conditions, such as temperature, pressure, kind of gas and nature of the catalyst. The yield of CNTs with the electric arc discharge methods is estimated between 70 - 90%, however the quality is often poor [18], [25]

Laser Ablation

With the laser ablation method, CNTs are synthesized by vaporizing graphite with a strong laser pulse. High processing temperatures of 1500K and an inert atmosphere of He or Ar are crucial. An inert gas flow transports the sublimated carbon atoms to a cooled collector, where they condense. Besides the collector, soot-containing CNT covers the walls of the reactor as well as the graphite rod. The implementation of two slightly delayed laser beams promise even more uniform vaporization of carbon [18], [23]. Similar to the electric arc method, laser ablation of pure graphite generates MWCNTs. Adding metal particles such as Fe, Co or Ni to the graphite target yields SWCNTs. CNTs fabricated with laser ablation appear to grow from the root and this method tends to create chiral structure, as well. Interestingly, laser ablation seems to favor the synthesis of metallic CNTs [25]. However, the yield and quality fluctuates with the experimental setup and the additives. Although laser ablation enables the

synthesis of high quality CNTs, the quality is accompanied by low yields. Thus, this technique is unsuitable for mass production and is mainly applied in research.

Chemical Vapor Deposition

The synthesis of CNTs with CVD (chemical vapor deposition) involves the catalytic decomposition of a carbon feedstock on a metallic substrate, either with solid substrates or in gas phase. Carbon-compounds such as carbon monoxide or hydrocarbon are thermally cracked in an inert atmosphere of H_2 or Ar and the presence of catalytic metals, e.g. Fe, Co or Ni at atmospheric pressure. Compared to laser ablation and electric arc discharge the processing temperature is lower and ranges between 900 - 1300K [18], [23], [24]. Depending on the catalyst, the nanotubes grow from either the tip or the root. While Ni seems to favor tip growth, Fe and Co rather support root growth of CNTs. Additionally, the size and the nature of the catalyst seems to affect the type, thus either the growth of MWCNTs or SWCNTs or the diameter of the tubes. Although it is not yet possible to define the structure, CNTs forming one bundle, synthesized by CVD exhibit the same chirality [25]. The mild conditions of CVD allow a high level of growth control, such as the growth of aligned nanotubes or defined networks. Especially SWCNTs are synthesized in good quality with high structural perfection. Simultaneously CVD enables low-cost and large-scale synthesis and is well qualified for mass production of CNTs [23], [25]. Different research groups reported the synthesis of SWCNTs and MWCNTs from 1 μm to a few hundred μm in length, fabricated with CVD [17], [26], [27].

CNT Purification

Since there is no method to synthesize CNTs of one single type or structure yet, purification is a main challenge besides the synthesis. The purpose of purification is to remove all by-products, such as impurities and graphitic and catalytic residues. In addition, the different types of CNTs are separated according to their structure and dimensions. Purification methods include chemical treatments, e.g. oxidation, acid treatment and annealing, as well as physical techniques, such as filtration, chromatography and centrifugation. While oxidation removes the carbonaceous impurities, acid treatment decomposes the metal residues in the CNT-soot. Annealing allows both, with the beneficial side effect of rearranging the CNTs and consuming defects in their structure. However, high temperatures also pyrolysis fullerenes and short nanotubes. Generally the disadvantage of chemical purification is that these methods attack the nanotube structure and usually destroys usable by-products, such as fullerenes or graphitic carbon layers [25], [28].

Compared to chemical treatments, physical techniques are less harmful for the structure of CNTs. During filtration or chromatography, for example CNTs and large carbon nanoparticles remain in a filter system, while catalytic residues and small impurities are

transferred further. Centrifugation takes advantage of the different densities and deposits individual material compounds in different phases. However CNTs are barely soluble and form bundles after synthesis, which complicates the physical techniques substantially [25], [28].

2.1.2 Properties of CNTs

The type of the nanotube mainly defines the properties of CNTs: single-walled or multi-walled. Both, the properties of SWCNTs as well as MWCNTs, are affected by the perfection of the lattice and the structure of the tube. Thus, the quality of a CNT is dependent on the number of defects embedded in the honeycomb structure during synthesis, such as foreign particles or pentagonal, instead of hexagonal carbon-rings. However, while the chirality of the nanotube strongly influences the characteristics of SWCNTs, the properties of MWCNTs are determined by the orientation of the tube-tube graphene layers. Additionally, the number of tubes considered strongly influence the properties. In the following section, some important properties of CNTs are outlined.

One characteristic making CNTs an appreciated material in research and development is their huge width-to-length aspect ratio. The dimensions of a CNT are defined by the synthesis technique and the environmental conditions during the synthesis such as temperature and presence or type of catalytic particles [18]. Theoretically, there is no restriction in maximal diameter of a CNT, as well. However, practice has demonstrated, that single tube diameters less than 2.5 nm are energetically more favorable [29]. Considering MWCNTs Benoit et al. experimentally observed inner tube diameters from 1 - 4 nm and outer tube diameters from 4 - 45 nm based on the number of walls [30]. In either case, the result of a nanotube with a few nanometers in diameter but several micrometers in length is a huge aspect ratio. Proportionally a human hair would need 40m in length to achieve a similar aspect ratio as a SWCNT [31].

Another exceptional property of CNTs is their low density due to the hollow interior of the tube. For SWCNTs, it amounts to about 1.3 g/cm^3 and for MWCNTs to about 2.1 g/cm^3 [32], [33]. For comparison: the densities of copper and aluminum are 8.96 g/cm^3 and 2.7 g/cm^3, respectively. In consequence of the huge aspect ratio as well as the low density, CNTs are physically considered as a 1-dimensional system. This characteristic initiates new approaches and advantages regarding electrical and thermal conductivity, stability, chemical reactivity etc. [17], [34].

As mentioned in section 2.1 the electrical properties of CNTs are dependent on the lattice structure of the nanotube. Due to the delocalized electrons from the π-bonds in the honeycomb lattice, metallic SWCNTs show similar electrical conductivity as typical

conductors, such as copper and aluminum. Simultaneously, considering their low density in opposite to the dense crystal structure of metallic conductors the cost of material for a CNT conductor with similar electrical conductivity is much lower [35]. In an experimental study, Zhou et al. investigated the resistance of copper nanowires and SWCNTs. They compared 40nm x 40nm bundles of Cu-nanowires with (5,5)-armchair SWCNTs and found a resistance of R_{Cu} = 14 Ω, without taking into account surface scattering of electrons and R_{Cu} = 53 Ω with surface scattering. This is one order of magnitude greater than the resistance of the SWCNT bundles R_{sw} = 4 Ω [36].

Semiconducting SWCNTs show p-type conduction in ambient conditions and depending on the tube dimensions the charge carrier transport is either diffusive or ballistic [37]–[39]. Additionally they were found to exceed the field effect mobility of conventional silicon semiconductors [37], [38]. Besides electrical conductivity, CNTs demonstrate excellent thermal conductivity, as well. Their structure ensures a large mean free path for phonons, which expresses in a thermal conductivity similar to that of a high purity diamond around 6000 W/m K at room temperature [39].

In terms of mechanical stability: The strong covalent carbon bonds expressed by a very short inter-atom spacing of 0.142 nm of CNTs enable high stability against deformation. For comparison, the interatomic spacing of diamond is 0.154 nm. With a tensile modulus of 1-1.3 TPa CNTs are additionally at least 5 times as robust as steel [40]. While the stability of SWCNTs is mainly dependent on the tube-size and the chirality, the elastic modulus of MWCNTs is rather correlated to the quality of the graphene lattice than to the nanotube diameter [19]. Due to their mechanical stability, CNTs are ideally suited for high-tensile components. Despite the large surface area of CNTs and the slightly sp3-hybridized carbon, atoms are CNTs barely reactive. The arrangement of atoms in the lattice leaves no room for dangling bonds. Only defects in the structure or opening in the tips could slightly enhance the chemical reactivity of CNTs. Nevertheless, the hollow structure of CNTs enables adhesion of molecules by physisorption. Studies have shown that adsorption, onto the surface or inside bundles, is even better than on individual tubes. Molecules and compounds can either nest inside a tube, at the outer surface of a tube or in the groove between neighboring tubes [18].

2.2 CNT Thin-Film Devices: Case Studies

Due to their unique properties, CNTs have been used in a wide range of application. Nomura et al. also took advantage of the high capacitance of CNTs and applied them as CNT electrodes in lithium-air batteries [41]. They achieved areal cell capacities up to 30 mA

h/cm^2, far exceeding the capacity of conventional lithium-ion battery cells. Another approach in developing power sources of CNTs was published by a group from MIT. To enable power sources of nontoxic material they fabricated a thermopower wave device of CNT-wires coated with a combustible material [42]. With this approach they achieved energy densities similar to Li ion batteries and chemical-to-electrical conversion efficiency over 1%. Pan et al. reviewed the contribution of CNTs to the efficiency of super capacitors for energy storage. The high capacitance, low resistance and high stability of CNTs as well as CNT composites qualifies them as excellent electrode materials for super capacitors [43]. Additionally, the flexibility of CNTs networks enhances the durability of the air-electrodes, as they tolerate the mechanical stress during discharge solid deposition without damage [41].

2.2.1 Field Effect Transistors

The first transistors based on a semiconducting CNTs has been reported by Tans et al. in 1998. They fabricated and characterized a FET with an individual semiconducting CNT as active material between drain and source contact at room temperature [44]. Similar approaches followed over the next few years and confirmed their findings [38], [39], [45].

In the early devices, fabricated by Martel et al., the hole mobility μ_p in the linear regime amounted to ca 20 cm^2/Vs at a transconductance of 1.7 $^{10.9}$ A/V [37]. Today typical field effect mobility in SWCNT-FETs range from 1000 to 10 000 cm^2/Vs at room temperature [46], although unusually high mobility exceeding 100 000 cm^2/Vs have also been reported by Dürkop et al. [38]. While the average of the devices outperform conventional Si-MOSFETs, their mobility are at least three times smaller than those of graphene layers are. This finding supports the theory of diffusive charge transport in SWCNTs due to scattering sites and defects in the tube [37], [38]. These mobility values are for aligned CNTs without the CNT-CNT tube junctions that are prevalent in random CNT networks.

Snow et al. [47] found effective mobility μ_{eff} around 7 cm^2/Vs in a random network CNT-TFT. Additionally, their device showed an excellent on-off-ratio of I_{on}/I_{off} ca 105 and a threshold voltage of $V_{th} = 2$ V. For comparison, the effective mobility of a conventional amorphous Si-TFT is about one order of magnitude smaller $\mu_{eff,a-Si}$ ca 1 cm^2/Vs. Increasing the density resulted in enhanced mobility up to 1 cm^2/Vs, but simultaneously the gate effect diminished and the CNT-TFT behaved as a resistor. This indicates a reliance of the field effect in random network CNT-TFT to the density. A similar approach was pursued by Mousavi et al. [48], where they deposited 99% semiconducting SWCNTs on an IDE (interdigitated electrode) structure. They achieved mobility of μ_{eff} 40.75 cm^2/Vs and an on-off-ratio of $I_{on}/I_{off} = 2$ x 10^3 at a channel length of $L_{ch} = 8$ μm. The threshold voltage of the device was shifted towards $V_{th} = 4.8$ V and the maximum transconductance amounted for

$g_{max} = 91$ μS. These results suggest an increased CNT density compared to the TFT presented by Snow et al.

2.2.2 Gas Sensors

Although CNTs are chemically inert, CNTs were successfully examined as gas sensors. Physisorption enables gas molecules, such as NO_2, CO_2 or NH_3 to interact with individual nanotubes or random CNT networks in chemical FETs [49] or chemical resistors [50]. In either case the electrical conductivity of the CNTs was altered with the gas concentration, measured as shift in the resistance or as variation of the transfer characteristic. While the response and recovery time as well as the sensitivity are comparable to common gas sensors, such as high performance metal-oxide sensors, the selectivity was found to be the main drawback [49], [50].

Similar to CNT-FETs there are many studies regarding individual CNTs as gas sensing material [51], [52]. However, transistors based on individual nanotubes are unsuited for industrial applications, as for high quantities high-quality fabrication is expensive and reproducibility is minimal. Therefore, several teams focused on random SWCNT networks in chemFETs as demonstrated in [53], [54]. To achieve a gate effect, special attention should be devoted to the network density, which should be less than the metallic tube percolation threshold and a distance between the electrodes far beyond the length of the nanotubes [55].

Another team led by Novak [53] investigated the response of random network CNT-TFT to the nerve agent simulant DMMP (dimethyl methylphosphonate). Upon exposure the threshold voltage of the device shifted by approximately - 2 V, due to charge transfer from the electron donor DMMP to the nanotube network. In the linear regime at $V_{GS} = 0$ V they noted a 1.5-fold increase in sensitivity after 40 min of 1 ppb DMMP flow, with a response time of $t_{rsp} = 10$ s. The sensor was recovered by applying a positive bias of $V_{GS} = 3$ V which resulted in a recovery time of $t_{rec} = 200$ s.

Mudimela et al. [54] fabricated a SWCNT-chemFET for humidity detection. They reported an approximate two-fold decrease in the on-current after less than 20 min exposure to H_2O enriched air. The significant reduction of the on-current of the sensor as response to increased humidity is in accordance with the work of Zhao et al. [51]. H_2O is a donor molecule and induces electrons in the SWCNT film, which reduces the conductivity of the p-type material. Furthermore Mudimela et al. recognized a dependence of the recovery time on the applied gate voltage. At high gate voltages around V_{GS} -10 V, the recovery of the sensor is prolonged as the molecules diffuse further into the nanotube network due to the enhanced electric field.

In an attempt to enhance, the selectivity and sensitivity of a gas sensing TFT based on a random SWCNT network Star et al. [56] prepared a device functionalized with metal nanoparticles. After 5 min exposure to NH_3, H_2 and H_2S the sensor conductance decreased by 30%, 300% and 200%, respectively at $V_{GS} = 0V$, indicating that these gases induce electrons to the network. In contrast, NO_2 molecules enhanced the conductivity by 30% at the same gate voltage.

2.2.3 Thin Conductive Films

Due to their high flexibility and conductance, CNTs are suited for flexible and transparent electronics. Aguirre and his team examined the performance of SWCNT electrodes as substrate for OLEDs (organic light emitting diodes). They determined a luminance efficiency of 1.4 cd/A, which is comparable to the luminance efficiency of ITO-OLEDs of 1.9 cd/A. For further experiments, they suggest to enhance the transparency/conductivity ratio in order to improve the performance of CNT-OLEDs above that of ITO-OLEDs [57]. In 2006 Rowell et al. fabricated organic solar cells with electrodes of SWCNTs on plastic substrate. At the time efficiencies, 2.5% at AM 1.5 G, similar to conventional organic solar cells, they outperformed in flexibility [58].

2.3 Relevant Processing Techniques

The following subsections a brief overview of the relevant coating and deposition techniques is given.

2.3.1 Spin Coating

Spin coating is an effective technique for applying flat thin (<200 nm thick) films on flat substrates and has established itself as the primary process for coating polymer films [59], [60] and is widely used for applications of devices in microelectronics and optoelectronics [61]–[63].
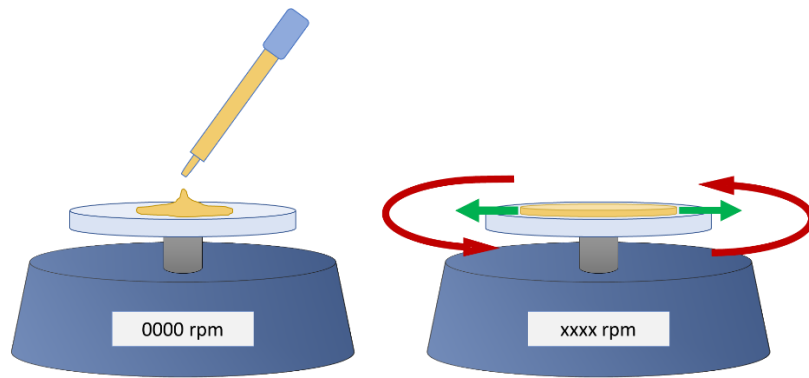
Figure 2-1 Schematic displaying the deposition of a material in liquid with the subsequent operation. The red arrows display the directional spin of the substrate. The green arrows display the movement of material during deposition

The substrate placed on the chuck of the spin coater and is held in place by vacuum. The material to be coated can then be applied in liquid form to the center of the substrate with a pipette. After application of the material or, depending on the spin method, also during the application, the chuck begins to rotate, forces the liquid outwards due to centrifugal forces and spinning off excess material until only a thin film remains on the substrate. The process is shown in Figure 2-1. The rotation phase can be subdivided into three stages: The deposition and spin up phase in which the speed of the chuck gradually increases to the desired speed and spreads the liquid over the entire substrate, which after most of the liquid is centrifuged off at the substrate edges; The spin off phase on which the desired rotation speed and rotation time (at least 30 seconds) determine the thickness of the film by a combination of convection and solution evaporation; And lastly the dry phase where the final film is only thinned by the loss of the solvent. [64] The rotation speed is usually given in rpm (rounds per minute). Mathematical models allow the calculation of polymer film thicknesses by the process and material parameters [65].

2.3.2 Physical Vapor Deposition

Thermal evaporation is a process, which is assigned to the group of physical vapor deposition. It is a well-studied and established method that is used for several decades in terms of deposition of metals, carbon, metal oxides and even organic materials [66]–[70].

The deposition process can be explained very simply: The substrate is hung upside down in a high vacuum system and the material to be evaporated is filled into a resistive boat at the bottom of the system. After evacuating the system to high vacuum, the material is heated up by the high current applied to the boat until it sublimates. The extremely low pressure of less than 10-6 mbar lowers the melting and boiling point of the material and increases the mean free path length of the sublimated material so that it resublime on the substrate. Several

materials can be co-evaporated at the same time if more than one boat is used in the system. By using a shadow mask, the substrate can be deposited in a patterned manner. [71]

2.3.3 Spray Deposition

Although spray technology has a variety of applications ranging from humidification to combustion, the more relevant for printed electronics is its use as surface coating. In industry, we are familiar with this process, e.g. for car body painting. In the last decade, however, due to reasons such as process scaling, the possibility of using all dissolvable materials or the determination of layer thicknesses, the process has gained increasing interest in organic solution-processed devices such as organic solar cells [8]–[14]. The advantage of spray coating is the high throughput and the low material waste for large-area deposition and it is fully roll-to-roll (R2R) compatible, which allows low-cost fabrication of sprayed devices.

The process of atomized spray coating can be seen in Figure 2-2. The coating liquid or ink is decomposed into small droplets (atomization) at the nozzle of the spray head with the aid of a compressed air stream, such as oxygen or nitrogen, creating a continuous drop-let flow, which is directly applied on the substrate. The most relevant parameters for the atomization process are the surface tension, viscosity and liquid density of the ink, as well as the atomizing pressure of the gas, solution flow pressure and the opening of the nozzle. The substrate itself lies on a heating plate, which has a specific constant temperature. Ideally, the droplets fuse together on the substrate surface and dry out to a homogeneous thin film. The quality of the coated layer is determined by the wetting behavior of the ink, the surface characteristic of the substrate, the spray distance to the substrate, the spray speed, the temperature of the heating plate, the droplet size that is determined by the previous mentioned atomization process parameters and the quantity of the sprayed layers.

Air-assisted nozzles make use of a high velocity gas stream to produce atomization. The liquid is fed into the nozzle either under pressure or as a gravity fed alternative. At the orifice, the liquid is mixed with the gas stream, which disrupts the liquid causing atomization. Fi displays a standard air assisted nozzle with the inset displaying the point of atomization. The droplet size is dependent on many factors such as the velocity of the gas stream, the ratio of gas to fluid, fluid properties as well as nozzle dimensions.
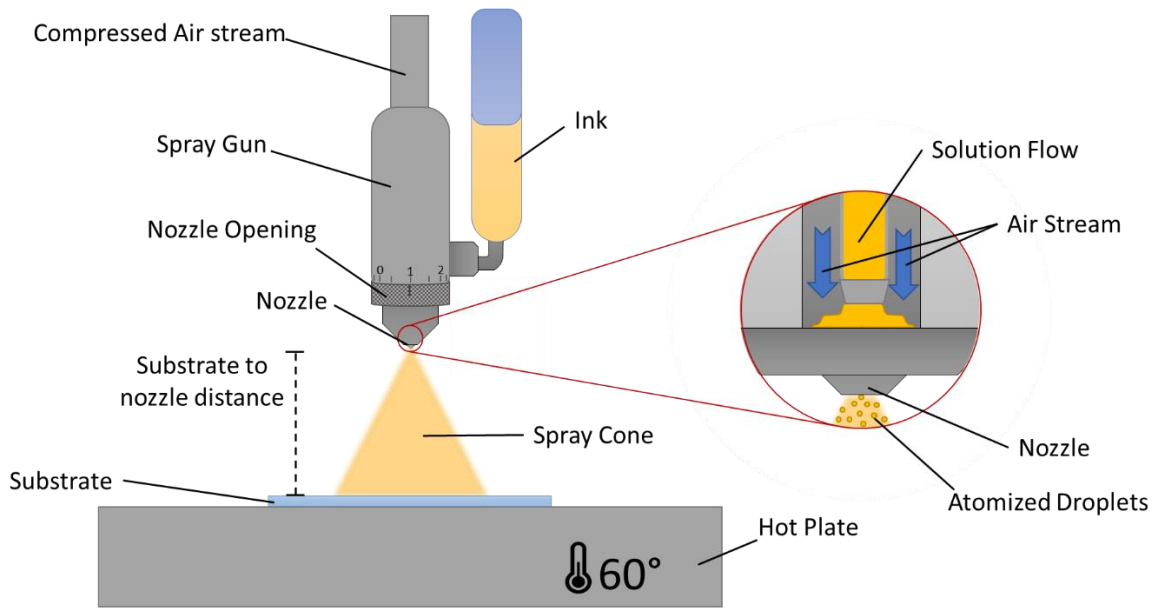
Figure 2-2 Schematic displaying a typical air-assisted atomization nozzle including key elements in a spray deposition setup. The insert displays the point of atomization.

Ultrasonic-assisted nozzles utilize a vibrating body based on a piezoelectric transducer that vibrates at ultrasonic frequencies. When this body is brought into contact with the body of fluid the liquid becomes unstable generating a mist of droplets. In most cases, this mist is mixed with a carrier gas that transports the droplets to the surface. Based on the applied frequency the droplet size can be varied. As with air-assisted nozzles the droplet formation also depends on a multitude of factors, both nozzle as well as fluid related. For further detail on spray technology, the reader is referred to the work of Lefebvre [72].

In terms of printed electronics, spray deposition has been used for a multitude of device. Both conducting as well as semiconducting devices being produced. Some of these devices include TFTs [73], TCFs [74], chemical/bio sensors [75], [76], OPVs [77] as well as OPDs [78] to name a few. Falco et. al. [79] presented a fully spray deposited, TCO free, flexible OPD based on a blend of P3HT/PCBM. It demonstrated the feasibility of spray deposition as a method for printed organic electronics especially since all layers were successively deposited by the same technology.

2.3.4 Screen Printing

Screen printing is a technique to transfer ink through a screen onto an arbitrary substrate. The screen is usually made of a permeable synthetic polymer mesh, which is partly coated with an impermeable photo-emulsion to realize a desired structure on the mesh. In order to

print the screen is mounted 1 to 2 mm above a substrate and covered with ink. Then, a squeegee is moved along the surface, pushing the mesh on the substrate and pressing ink particles through the openings. Due to the tension of the mesh, the screen lifts off the substrate after the squeegee passed and leaves the substrate covered in ink with the desired structure [43]. The basic principle of screen printing is shown in Figure 2-3.
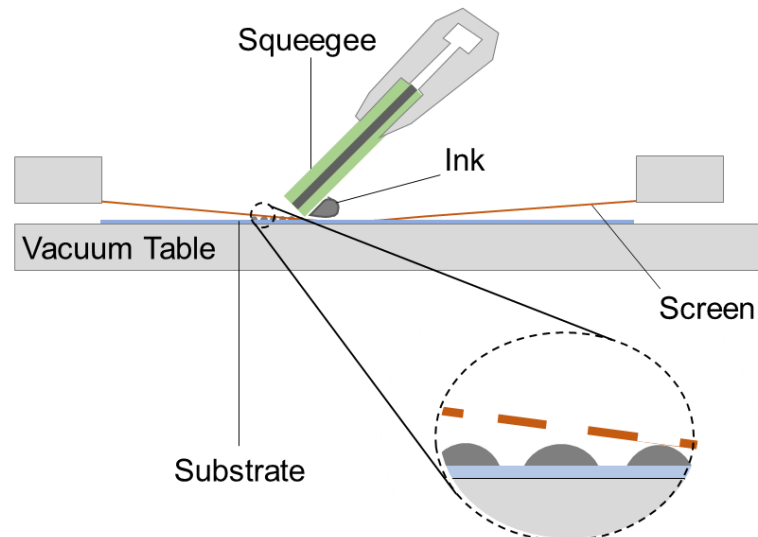

Figure 2-3 Schematic representation of the basic principle of screen-printing. The ink is pushed through the openings in the screen by moving a squeegee along the surface. The magnification shows the deposition of ink particles at the substrate after the screen lifted from the surface.

2.3.5 Summary

In this chapter, we introduced carbon nanotubes. After a short historical introduction, we described key characteristics of CNTs which makes them unique both in terms of functionality as well as characteristics, electrical and physical. We shortly discussed chemical composition of CNTs as well as transport mechanisms. We displayed common fabrication techniques for the synthesis of CNTs and the corresponding purification techniques. Following that, we presented state of the art devices from literature relevant to the work presented in this thesis, namely gas sensors, thin-film transistors and thin conducting films. These devices give an impression as to the wide range of application in which CNTs find application. Finally, we gave a short overview of the key processing techniques used in this thesis: spin coating, spray deposition and screen printing. The key benefits as well as drawbacks of each method was highlighted along with a short review of the areas where each method was successfully used in the printed electronic ecosystem.

Chapter 3

CNT Thin-Film Technology: Spray Deposition

In this chapter, all aspects pertaining to the spray deposition of carbon nanotube (CNT) thin films will be investigated. Initially a brief framework will be presented highlighting the key challenges and goals of the process as well as the strategic decisions taken. Following will be a breakdown of the individual key process blocks in the form of solution preparation, spray deposition and post treatment in order to more thoroughly explain and understand the critical aspects of the entire process.

3.1 Process Framework

The goal of the process presented is to develop a method that at its core allows for the large area deposition of CNTs on arbitrary surfaces. The focal point being the arbitrary surfaces. Due to the many applications to which CNTs lend themselves, the proposed process should be as integration compatible as feasible.

Dissecting this goal into smaller more specific targets: Initially the target material, in this case CNTs, needs to be brought into a spray able medium, which constitutes the first task namely solution preparation. A liquid medium lends itself best to this due to the extensive knowledge existent from other research fields and industries. In terms of solvents, due to the enveloping goal of arbitrary surfaces, it would be ideal to select a weak solvent with a low boiling point. A negative example of such a solvent would be the, in organic photovoltaics used, dichlorobenzol (DCB). A high processing temperature limits the choice of substrates while the solvent limits the materials on which the film can be deposited on without the probability of dissolving underlying layers. As such, the targeted solvent is deionized water (DI H_2O). In addition to the low boiling point, and low solvent power DI H_2O is both

environmental friendly and non-toxic to humans as such rendering it a perfect candidate as the solvent of choice. The second decision was the target concentration of the resulting solution. An overlap exists to the next block were a trade-off exists between material deposition rate and quality of deposition. Furthermore, it is to be noted that solutions with very low CNT concentrations tend to exhibit local inhomogeneity. As such, the approach taken was to prepare a solution with a higher than required concentration and dilute down to match the required application. This approach also yields solutions with longer shelf lives.

The second main task is the actual spray deposition of the prepared solution. In order to be able to deposit the solution over a large area the deposition system should either itself or the target be mobile. Due to available equipment, a sheet fed system was selected where the spray head is moved over the target. A critical aspect of this approach is to guarantee the uniformity of the deposited film over the entire target area. Multiple factors play a role in the quality of the resulting film such that we will go into further detail in the corresponding section.

The final block is the post deposition treatment of the films. Here the main goal is to remove any undesired materials, in most cases the dispersing agent and any residual solvent. The ideal scenario is a pristine film consisting solely on CNTs. In this area, we will have a look at the chemical and thermal treatments proposed in literature and by means of various characterization techniques determine their success.

3.2 Solution Preparations

The initial task of spray deposing CNT is to bring these into a liquid solution. What is else an advantageous characteristic also poses the greatest challenge in dispersing the CNT namely the high aspect ratio. Due to the large aspect ratio and strong Van der Waals forces CNTs [80] naturally bind into rope like bundles post synthesis. In these rope-like bundles metallic CNTs dominate charge transport [81], [82] posing a huge challenge when a semiconducting behavior is desired. A further negative characteristic of poorly debundled films include high film roughness, which increases the difficulty of integration into other material systems such as OPV due to possible shorting of the thin layers present in such systems. In addition, bundled CNTs strongly decreases their actual aspect ratio as such having a negative effect on its capabilities as a TCF due to the increase in absorbance. Resulting from this is that bundling is an undesired quality and a higher degree of dispersion is preferred. A main goal of the solution preparation is to overcome the van der Waal forces binding the CNTs together and isolate the individual tubes as to prevent a recombining.

Strano et al. [83] have proposed a debundling mechanics where under the addition of mechanical energy, usually in the form of ultrasonic waves, in the presence of a dispersing agent, which binds to the CNTs in order to prevent rebinding, it is possible to create a stable dispersion. The working principle is that under the effect of sonication the CNTs begin to entangle at the bundle ends creating binding sites for the dispersant molecules to attach. Most dispersing agent molecules are designed in such a way that the non-binding side repel each other. The dispersing agent creates an effective wedge that pries open further binding sites with assistance of the ultrasonic waves. This process continues until the CNTs are fully separated and coated with the dispersion molecule. Figure 3-1 displays schematic of the bound dispersant molecule (specifically carbomethyl cellulose (CMC)) to the CNT post dispersion. Hu et al. [84] have provided an extensive review of viable dispersing agents describing advantages and disadvantaged as well as viability.

 A non-negligible side effect that can occur due to prolonged ultrasonic agitation is that severing of the CNTs can occur [85]. This severing results to significant shortening of the tubes resulting in reduced aspect ratios and a negative impact on the performance of the films post deposition. An additional well known technique from chemistry is the centrifugation of the solution to aid in the separation of the separated tubes from the remaining bundled CNTs. Here due to the heavier mass of the bundled CNTs these will effectively be forced to the bottom of the vial due to centripetal force.
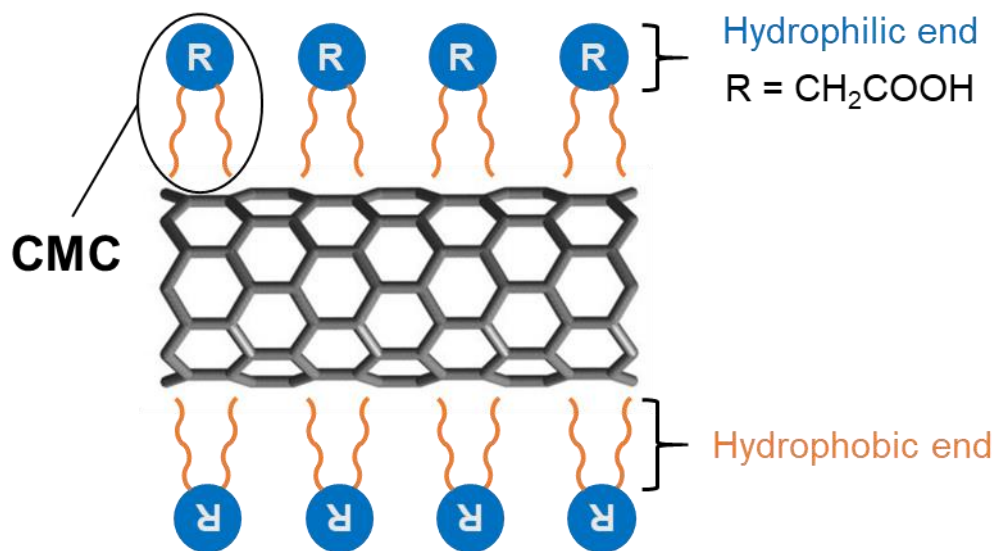

Figure 3-1 Schematic representing bound dispersant molecule (CMC specifically) to CNT post dispersion. The hydrophobic end is bound to the CNT, depicted as the orange tail, thile the carboxylic end, depicted as the blue circle, faces outward.

In terms of the decision as to which dispersing agents we would use, two were selected in order to provide a wider process space. The selected agents are the aforementioned CMC,

which is a cellulose derivative and sodium dodectyl sulfate (SDS) a reagent most commonly used in soap. CMC provides the better dispersion of the two but is significantly more difficult to remove, as the usual procedure is a prolonged bath in dilute nitric acid while the SDS solely requires a short bath in DI H_2O. As such depending on the target application a trade-off between dispersion quality and process, integrability can be made.

3.2.1 Material and Methods

The solutions prepared and used in this thesis are all aqueous based. This choice of solvent is in line with the aforementioned goal of creating a process that allows for the coating of arbitrary surfaces due to it low invasivity and low boiling point. For the solution preparation a base aqueous solution is mixed consisting of the dispersing agent dissolved in DI H_2O. Depending on the dispersing agent varying weight percentages (%wt) are used. For CMC (Sigma Aldrich) 0.5 %wt while 1 %wt sodium dodectyl (SDS)(Sigma Aldrich) are used. The disparity in concentration is derived from the effectiveness of the two agents as dispersants. The solution is stirred overnight ($\geq$12h) to ensure the dispersant is completely dissolved. The CNTs are transferred in a N_2 atmosphere glovebox (MBRAUN) into solution. This process step is done as a safety precaution and has a limited effect on the CNTs as most resulting devices are not encapsulated. The %wt unless otherwise mentioned is 0.03 %wt. Although this concentration is far below the limit of what can be dispersed with the aforementioned dispersing agents [86] a strategic decision was made to try to maximize dispersion quality over other factors such as material deposition rates as these could always be aided during the deposition process. For the actual dispersion, a 300 W horn sonicator (Branson) was immersed at 60% into the beaker surrounded by an ice bath to reduce the effects of the heating during the sonication process. The regime in which the sonicator was operated was always in alternating 5 min periods of varying power. The optimal operating regime was investigated in a previous work [87]. It was found that rather than prolonged periods at high sonication powers a comparable degree of dispersion could be achieved with significantly less severing of the CNTs. For CMC a regime of 50%/30%/50% was employed while for SDS 50%/30%/50%/30%/50% was necessary due to the poorer dispersion properties of the dispersing agent. Subsequent to the sonication, the solution is centrifuged at 15000 rpm for 90 min. The top 80% of the resulting solution is decanted and used as stock solution. For SDS the process of sonication and centrifugation is repeated. This stock solution can be diluted down for different spray deposition processes for example for CNT thin film transistors where sub monolayer films are required while the stock solution can be used as is for example in thin conducting films that are employed as electrodes in optoelectronic devices which tend to be in the 100nm thickness range. Exact dilutions will be detailed in the corresponding device section.

3.2.2 SDS process optimization

In terms of solution characterization, the general approach was the preparation of the solution followed by a subsequent deposition of the solution, usually by spray deposition, and the corresponding post deposition treatment. The films were then analyzed by atomic force microscopy (AFM) and qualitative comparison to existing films were made. Due to the large work already done with regard to this aspect, this work focused on improving an existing process for SDS due to the large disparity in the quality between it and CMC [88]. The strategy employed here was to use the existing process and identify possible improvements to reduce the discrepancy between SDS and CMC. The main issue which was identified, was that the dispersion in itself was not sufficient as significant bundles were still present as can be observed in Figure 3-2 a. As known from previous experiments, a longer sonication period could further enhance the debundeling process however, this also brings a risk of severing CNTs. As such, a hybrid approach was taken. Rather than targeting to fully disperse all the CNTs present in the solution we would filter the bundles out which could not be separated. The resulting process of this approach was to take the stock solution that was prepared with the standard process and treat this as the initial solution. This solution was again sonicated at 50%/30%/50%/30%/50% of 300 W with each interval lasting 5 min followed by a centrifugation at 15000 rpm for 90 min. Once again decanting the top 80% to ensure that number of bundles present in the solution was minimized. The result of the additional processing step can be seen in Figure 3-2 b. This is an AFM image of a representative area of a spray deposited SDS solution displaying the noticeable difference between the standard preparation procedure and the enhanced process. Clearly visible is the reduction of prevalent bundles and a more homogeneous distribution of the CNTs. Due to the strong bundeling prior to the second preparation cycle it is not feasible to compare CNT length as to make any statements regarding the severance of the CNTs due to the additional sonication cycle. Based on coverage ratio it can also be seen that a thinning of the film is present. This is to be expected as the final CNT concentration is expected to decrease due to the additional centrifugation and decanting cycle.
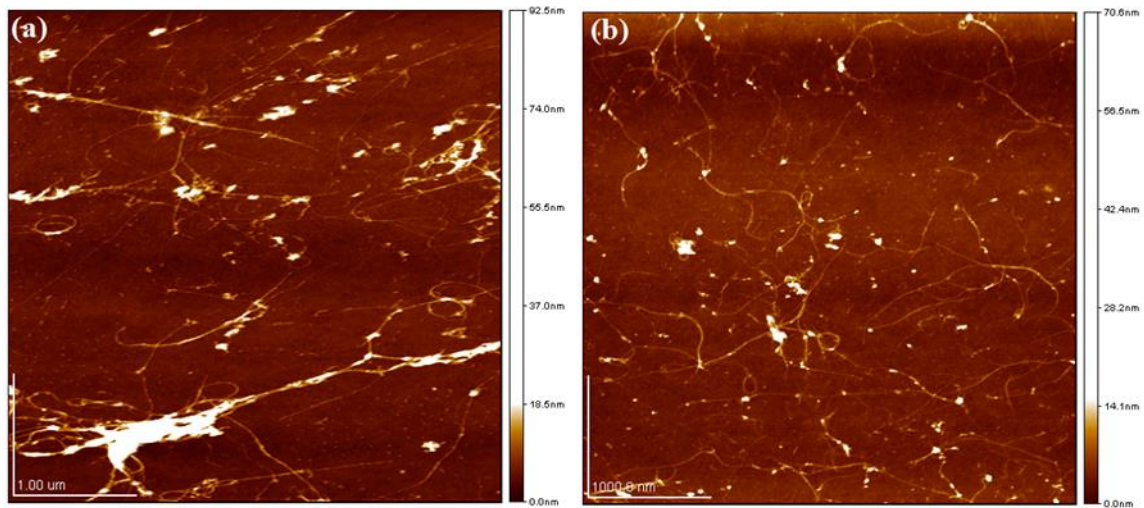
Figure 3-2 AFM images displaying 4 x 4 µm films deposited from 4L SDS solution (a) after first sonication and centrifugation and (b) after second sonication and centrifugation step.

3.3 Spray Deposition

For the deposition of the prepared solution, spray deposition is used. As the solution preparation process was tailored to the deposition technique, the solution can be deposited as is and does not require further alteration. For all fabricated devices in this thesis, the same system was used and as such, it is applicable to all further chapters.

While developing deposition protocols and adjusting parameters for a desired deposition it is essential, to start with a strategy as how to aboard the challenge of covering the immense parameter space that is available when it comes to spray deposition. With this proposition, the initial step was to identify the parameters that played a role in the deposition quality of the film as well as defining what constitutes a desirable result at a macroscopic and microscopic level. Following this, with knowledge from literature [89] and previously published work [50], [78], [90] a starting point can be established and with rough trial and error experiments accompanied by optical examination of the film, the process window can be significantly reduced. At this step, a significant number of processes parameters are fixed and optimization can take place with a more thorough post deposition characterization. In the following sub chapters, a more detailed report of this process development can be seen.

3.3.1 Material and Methods

For the deposition of the solution, an automated setup was used. The key elements of the automated setup are an industrial low pressure low volume atomizing spray valve (Nordson

EFD), a four axis automated motion platform (PVA) and an aluminum hotplate (Hillesheim). We operated the nozzle in the wet spraying regime with an orifice opening of 0.7mm and a nozzle-substrate distance of 5 cm. The atomizing and material pressure were adjusted to 0.5 bar and 0.03 bar. In order to achieve a complete thin film the hotplate temperature was set to 62 °C, to enable the evaporation and merging of water droplets on the substrate. We cover the substrates with CNT film thickness (denoted as xL), to achieve different network densities. Note, that one layer comprise one spraying process in x-direction followed by one spraying process in y-direction. In order to remove the dispersant CMC from the nanotube network we placed the samples in an acid bath. We diluted one part of HNO_3 with four parts of DI water and soaked the wafers for at least 12 h. In the last step, we removed our samples from the acid solution and dried them for 10 min at 100 °C on a hot plate, followed by a 10 min DI water bath and a subsequent drying step. For the removal of the SDS we submerged the as sprayed sample in DI water for 30 min followed by a subsequent drying step on a hotplate for 100 sec.

3.4 Post Deposition Treatment and Functionalization

In order guarantee a proper removal of the dispersant used we performed X-ray photoelectron spectroscopy (XPS) measurements as to track the removal of the CMC residues. In addition we also performed Raman spectroscopy measurements to evaluate the desorption oh remaining HNO_3 molecules from the CNT film. Accompanying these characterization techniques we took FESEM images as to have an optical confirmation of the results.

3.4.1 XPS Measurements of Dispersant Removal

X-ray photoelectron spectroscopy (XPS) measurements were performed at a base pressure of 5 x 10^{-10} mbar with a monochromatic aluminum K_α anode as x-ray source, at an operating power of 350W. The high-resolution spectra were acquired using a SPECS Phoibos hemispherical analyzer from SPECS Surface Nano Analysis GmbH (Berlin, Germany) at a pass-energy of 20 eV with an energy resolution of 0.05 eV. The raw data were processed using the software CasaXPS from Casa Software Ltd. The accompanying FESEM images were taken using an NVision40 from Carl Zeiss at an acceleration voltage of 7.0 kV and an extraction voltage of 5.0 kV. The working distance was adjusted in a range of 5–6 mm to achieve the best image quality.

The XPS measurement was taken of a 4L CNT-CMC, pre and post dispersal removal with the corresponding FESEM image, results can be seen in Figure 3-3. A) displays the survey

scans of (black) as deposited CNT-CMC film and (red) post dispersant removal and 100°C annealing to desorb HNO_3 residue.
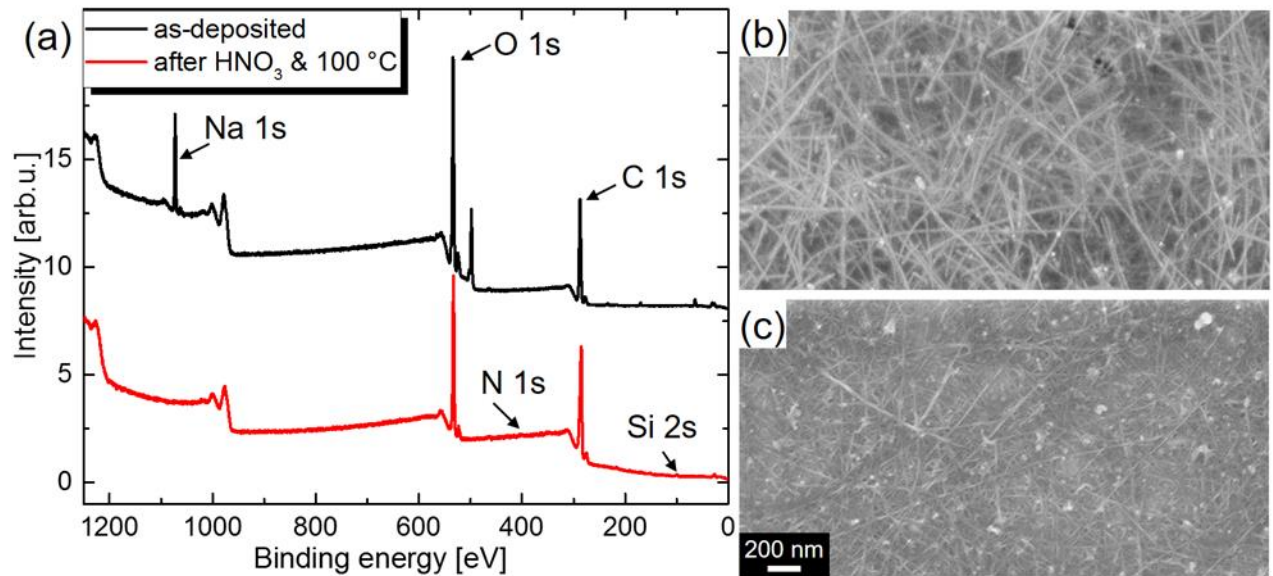

Figure 3-3 a) XPS survey scans of a 4L CNT-CMC layer (black) as deposited, (red) after 12h HNO_3 followed by a subsequent DI H_2O bath with an anealing step at 100 °C for 1h. FESEM images of b) as deposited 4L CNT-CMC film. c) 4L CNT-CMC film after 12h HNO_3 followed by a subsequent DI H_2O bath with an anealing step at 100 °C for 1h.[Results published in [91]]

From Figure 3-3 it can be recognized that the sodium Na 1s core-level peak and the lower binding energy O 1s-related peak vanish after the immersion treatment, which is accompanied by the appearance of a low Si-induced signal post treatment. This observation clearly indicates that the CMC matrix covering the CNT film is removed, and thus a small portion of the bare Si substrate is revealed. The structural formula for a CMC monomer that contains sodium atoms with the chemical formula $C_{28}H_{30}Na_8O_{27}$. Further, because of the immersion in HNO_3, a nitrogen-induced peak with a low signal occurs after the dispersant removal. Figure 3-4 shows the high-resolution spectra for C 1s, O 1s, Na 1s and N 1s for (I) pre treatment, (II) post treatment prior to annealing and (III) post annealing.
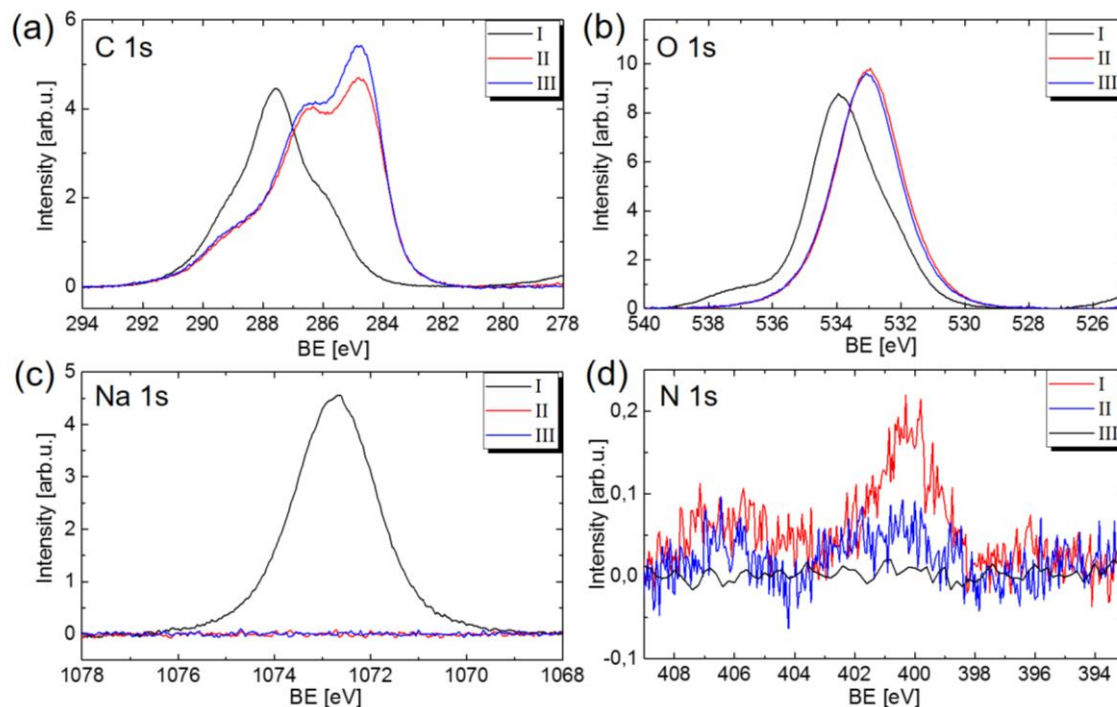
Figure 3-4 High-resolution spectra for High-resolution spectra for the different treatments and the core-level spectra (a) C 1s, (b) O 1s, (c) Na 1s, as well as (d) N 1s. The spectra are normalized with respect to the concentrations of the specific elements. (I) pre treatment, (II) post HNO_3 treatment prior to annealing and (III) post 100 °C 1 h annealing. [Results published in [91]]

From the high resolution spectra we can observe that post annealing the nitrogen peak disappears consistent with the assumption that the HNO_3 can be desorbed with a post treatment annealing step. Furthermore, due to changes in the C 1s and O 1s change, which indicate that the prominent carbon- and oxygen-containing compounds are altered after the immersion treatment. Lastly, the complete reduction of the sodium peak indicates an efficient removal of the CMC compound. In addition, the chemical shapes of the post deposition treatments were studied with the high resolution C 1s spectra seen in Figure 3-5.
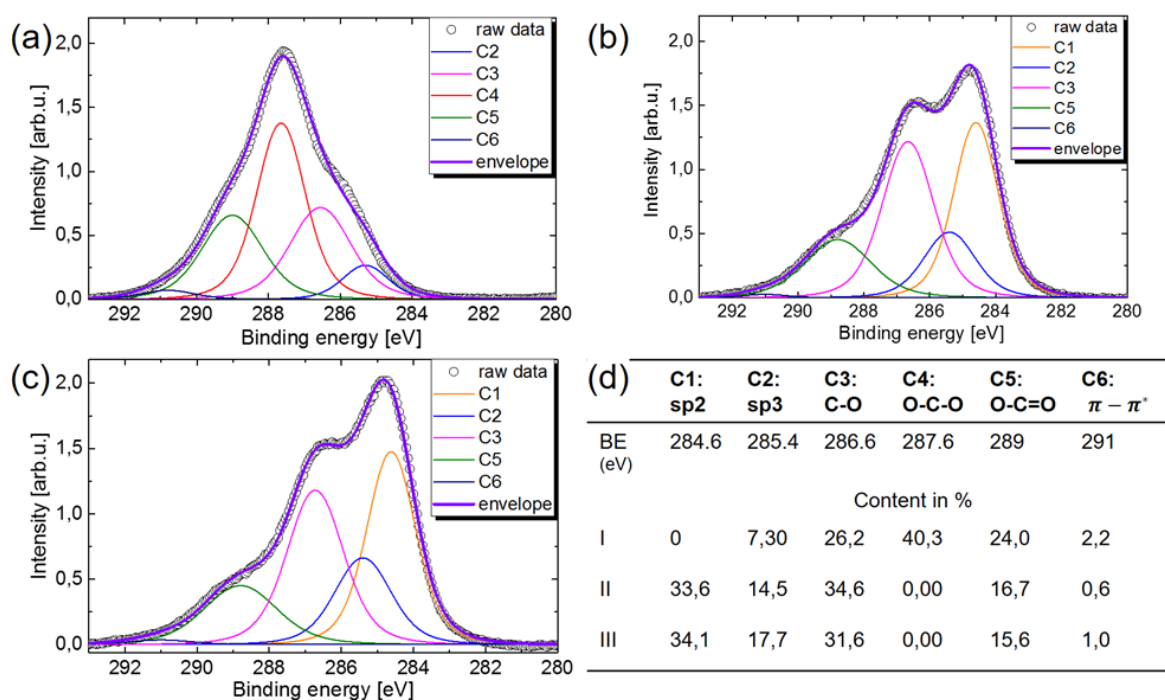
Figure 3-5 High resolution C 1s XPS spectra for the CMC-CNT films that were subjected to different treatments: (I) pre treatment, (II) post treatment prior to annealing and (III) post 100 °C 1 h annealing. The raw spectra were decomposed into different contributions by Lorentzian fits. (d) Table that summarizes the different contributions of carbon-containing species that add up to the spectra (a–c). BE—binding energy. [Results published in [91]]

The raw spectra were separated into six different contributions, in accordance with the chemical formula of CMC and the literature [92]. The contributions are labelled from C1–C6 which can be associated with different hybridizations of the carbon atoms in the CMC matrix and in the CNT film, as follows: C1s is mainly composed of sp2 hybridized carbon atoms that are characteristic for CNTs and graphene, C2 represents sp3 hybridized carbon that is present in graphite or organic molecules such as CMC, C3–5 denote carbon–oxygen compounds that are present in CMC or oxidized CNTs, and C6 denotes the π-π^* transition. The relative contributions that sum up to the overall C 1s signal are summarized in the table shown in Figure 3-5 d. Observable is that the post treatment leads to the removal of O–C–O and O–C=O groups that are present in the CMC molecule, whereas the relative contribution for sp^2 hybridized carbon increases significantly from around 0% for the as-deposited film to around 34% for the film after treatment. This result is further evidence that, for pre treatment, the CMC matrix entirely covers the CNT network and shields it from the XPS measurement, whereas after HNO$_3$ treatment, CMC is removed and the pure CNT-film is revealed. As the CNT film in its pristine form is known to be largely composed of sp^2 hybridized carbon atoms, the sp^2-percentage drastically increases after HNO$_3$ treatment. The remaining sp^3 hybridized carbon atoms that should not be present in an ideal CNT can be

ascribed to carbon-containing contamination and carbon–oxygen compounds in the nanotube [93], [94].

Only a small difference can be recognized for the shape of the C 1s signal for II and III. The removal of carbon–oxygen compounds that are associated with C–O groups can eventually be attributed to the removal of H_2O on the CNT film by evaporation. It should be noted that, similar to other groups, we have focused the main discussion of the high resolution scans on the C 1s spectra because the O 1s signal is usually superimposed by contamination and a thin water film that both add wide-band contributions to the spectra and partially obscure the alterations of the treatments [95], [96]. Nevertheless, similar conclusions as for the C 1s spectra shown in Figure 3-5 can be drawn from the O 1s spectra illustrated in Figure 3-5. Before the immersion treatment, the O 1s spectra is composed of a peak centered on a binding energy of 533 eV and higher binding energy contributions. The peak at 533 eV can be ascribed to a thin water film [97] that is present on all samples, whereas the higher binding energy contributions are associated with the oxygen atoms in the CMC matrix.

3.4.2 Thermal Annealing

In order to further assess the effects of doping or de-doping on the CNT network, Raman spectroscopy measurements are conducted shown in Figure 3-6. The features of interest for nanotube based composites are the G-band, along with the BWF line shape, and the G'-band, both characteristic for graphene-like structures. All measurements are normalized to the intensity of the G-band, to allow visual comparison. It is known from literature that doping due to HNO_3 leads to a blue-shift in the G-band and to downward shift for the G'-band [98]. For a more reliable measurement, a CNT film with higher density was selected. To evaluate the effect of the annealing, the plots for the as prepared (black) and the annealed (green) samples are compared. The inset shows that there is no shift in the peak for the G-band.. However, the BWF line shape shows a little change. The line shape is attributed to the loss of continuum states due to chemical modification [99]. Additionally, there is a slight line shape change in the G'-band (black arrow). To put this result in perspective, the red curve shows a sample doped with concentrated HNO3 for 1 h. The blue arrow in the inset indicates the reported blue shift in the G-band for doped CNTs. The BWF line shape is brought out from the other two samples and there is a significant downshift of the G'-band. The presented analysis is indicative of negligible HNO_3 doping due to the removal of the CMC.
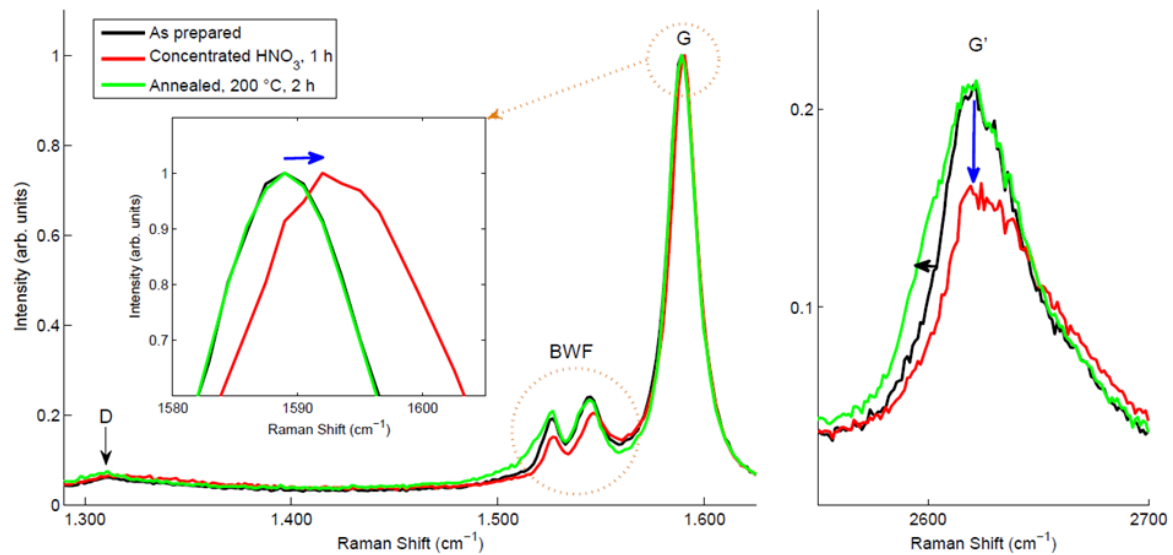
Figure 3-6 Raman spectra of the as-prepared 4L CNT-CMC layer(black), 1h concetrated HNO_3-doped (red), and 1h 100 °C annealed (green) CNT film at an excitation wave-length of 532nm. The inset shows a blue shift after doping. All Raman spectra were normalized by the G-band intensity. The arrows show the decrease of G'-band intensity after immersing in HNO3 and annealing, respectively. [Results published in [73]]

3.5 Summary

In summary, we presented a reliable and reproducible spray deposition process for the fabrication of uniform CNT films exhibiting state-of-the-art performance. Initially we laid out a framework and strategy for the spray deposition of the CNT films. We began with the description of key challenges and aspects of bringing carbon nanotubes into solution along with a brief description pertaining to key mechanics. We decided to use a dispersant aided approach with carboxymethyl cellulose (CMC) and sodium dodectyl sulfate (SDS) as candidates. We outlined the benefits and drawbacks of both dispersants. Following that, we described in detail both the preparation of the CNT inks as well as the spray deposition. For the SDS we enhanced the preparation process to reach a similar dispersion quality as CMC especially with regard to bundle minimization. The final part of the chapter showed with the aid of X-ray photoelectron spectroscopy as well as Raman spectroscopy that the proposed method of dispersant removal post deposition to be effective by displaying the total removal of dispersant elements. This was done with the use of a dilute HNO_3. In addition a post annealing allows for a desorption of the used HNO_3 which was verified by the used Raman spectroscopy.

Chapter 4

CNT Laser Assisted Ablation and Modification

4.1 Overview

Although the deposition of CNTs from solution by spray deposition offers significant advantages such as the reduced cost, scalability and non-stringent processing condition, this approach has certain shortcomings. Limitations include random alignment and non-definition of layer. We addressed the definition aspect in the previous sub chapter however the use of both shadow masking and photolithografical patterning have their limitations namely resolution and chemical contamination respectively. In this sub chapter, we will investigate a process strategy that promises to alleviate these problems. Laser assisted ablation offers an alternative to the above-mentioned processes. Specifically ultra-short laser pulse material ablation presents a precise subtractive patterning technique with a high resolution (10s nm) in addition to the characteristic small heat affected zone (HAZ). The HAZ is the area that is affected at a microscopic scale due to exposure from the heat of the laser pulse. Due to the sub-pico second pulse length, the interaction is limited with surrounding material and as such, precise material ablation can be performed. This is a critical characteristic as functional CNT films can have a thickness in the sub 10nm regime. Furthermore, it has been shown that a non-thermal ablation of material can be performed with the use of ultra-short laser pulses [100]–[102]. The ablation mechanism in such cases is strongly correlated to the subsequent thermal relaxation of the material after absorption of the laser pulse. Due to the random nature of our films, it will also be shown that by operating

the laser under the ablation threshold it is possible to modify the CNT film beyond binary ablation.

4.2 Material and Methods

For the experiments performed below films from stock SDS based solution, containing CNTs from Hanwha Nanotech Corp. were deposited in 10L. The laser processing was performed in collaboration with Max Spellauge at Prof. Huber's chair at the Lasercenter (LHM) at the Munich University of Applied Sciences (MUAS). Figure 4-1 represents a schematic of the laser setup used. The system consists of an Yb-doped solid-state laser with: wavelength λ=1030 nm, repetition rate $f_{rep} = 60$kHz and an average output of $P_{avg} = 1$ W. the laser is followed by a linear polarizer that is fed into a beam expander that allows for an enlargement of the beam diameter. A mirror system is used to guide the laser pulse to a half-wave plate (HWP) that enables the rotation of the polarization axis. The beam is finally focused by a focusing lens onto the sample, which is fixated on a motorized x-y stage.
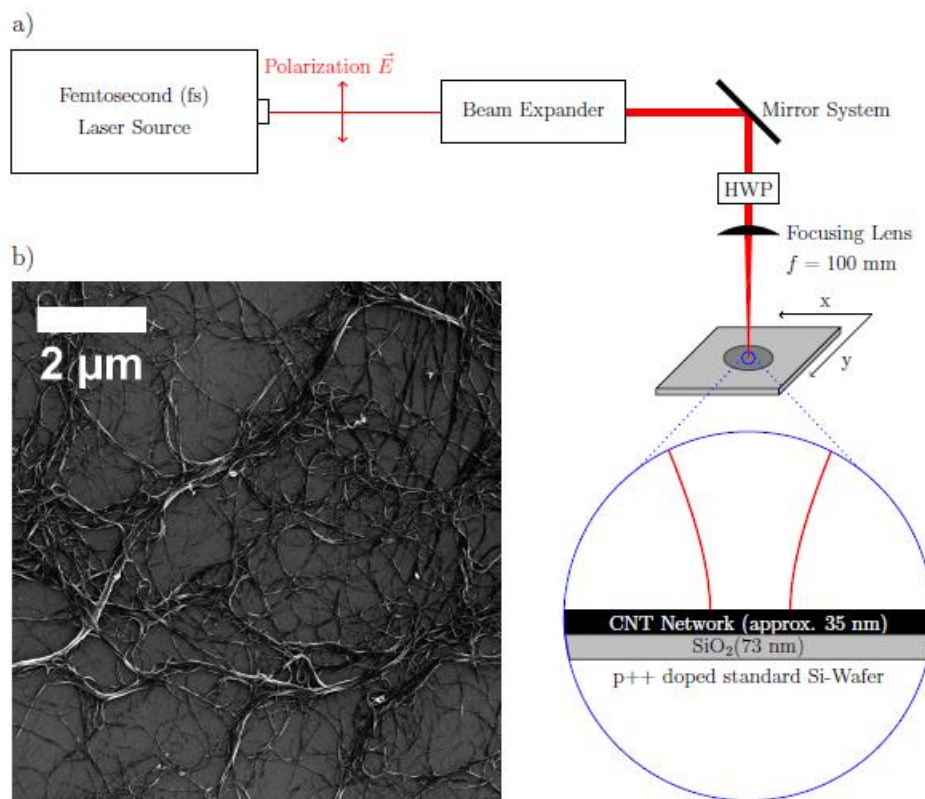

Figure 4-1 a) Schematic representing setup used for the ablation of the CNT network. System consists of a femtosecond laser, a polarizer, a beam expander, a mirror system, a half-wave plate and a focusing lens. The stage on which the sample is placed is mobile in x and y direction. b) FESEM image of a representative CNT network on a Si/SiO₂ substrate. [Results published in [103]]

A critical parameter concerning laser ablation is the peak fluence, which denotes the energy density of the beam at the focal plane. This is defined by (1) for a nearly diffraction limited Gaussian beam. Single pulse threshold fluence (Φ_{thr}) is a material dependent parameter defined as the minimal laser fluence required to introduce a modification at the material surface.

$$\Phi_0 = \frac{2\overline{P}}{f_{eff}\,\pi w_0^2} \tag{2}$$

Liu et al. [104] have suggested a method known as D^2 method for determining the threshold fluence. Based on the concept of energy conversion and assuming a Gaussian beam profile (2) is valid.

$$D^2 = 2w_0^2 \ln\frac{\Phi_0}{\Phi_{thr}} \tag{3}$$

D represents the diameter of the modified material area. By plotting the relation between D^2 and the Φ_0 on a half-logarithmic scale the liner relationship is visible and as such the threshold fluence can be extracted. As such, the threshold fluence is the intercept of, the linear fit of (3) to the experimental data and the x-axis. Each measurement point is a correlation of a peak fluence with a corresponding image and measured radii. A further concept that is required to understand the processing of CNT films by laser ablation is the spatial overlap of laser pulses for larger area modification. In order to achieve this the sample, which is placed on a x-y stage is moved at a speed v. To quantify the pulse overlap we define this as *OL* in % with the (3).

$$OL - 100\% \left(1 - \frac{v}{f_{eff}2w_0^2}\right) \tag{4}$$

Although to better understand the accumulated irradiation density, which is a more direct representation is the number of pulses per position (PPP). This is defined as (4). As such, the process window for the laser ablation/modification of a CNT film is given by the peak fluence and the PPP.

$$PPP - \frac{100}{100 - OL} \tag{5}$$

With a defined PPP, the threshold fluence can be extracted from (4). Here the diameter D is replaced for the width of the patterned line D_L and solving for Φ_{thr}.

$$\Phi_{thr} - \Phi_0 e^{\frac{D_L^2}{2w_0^2}} \tag{6}$$

4.3 Single Spot Laser Ablation

The initial characterization performed, to better understand, the interaction between laser and CNT film was to determine the different regimes in which we could operate the laser. A prerequisite of this process is that the ablation threshold for the material under investigation is below the threshold for the ablation of the underlying layers. The standard approach is for this is the above described D^2-method. Figure 4-2 displays (a)-(d) SEM images of a CNT film irradiated at different peak fluences in addition to the resulting plot for the D^2-method. The SEM images (a)-(d) show representative films in the different laser processing regimes. These regimes can be separated into four distinct categories: (a) at peak fluences between 0.057 J/cm^2 and 0.100 J/cm^2 a modification of the CNT layer can be observed. (b) At peak fluences between 0.100 J/cm^2 and 0.300 J/cm^2 an ablation of the CNT film is observed. Also visible is the larger diameter of the CNT modification regime (a) consistent with the Gaussian beam profile. This regime allows for the removal of CNTs without damaging the underlying substrate. It has been shown in previous works that the ablation threshold for CNT pellets is about 0.0025 J/cm^2 [105]. Other groups have found ablation threshold values ranging from 0.0025 J/cm^2 to 0.094 J/cm^2 [105], [106]
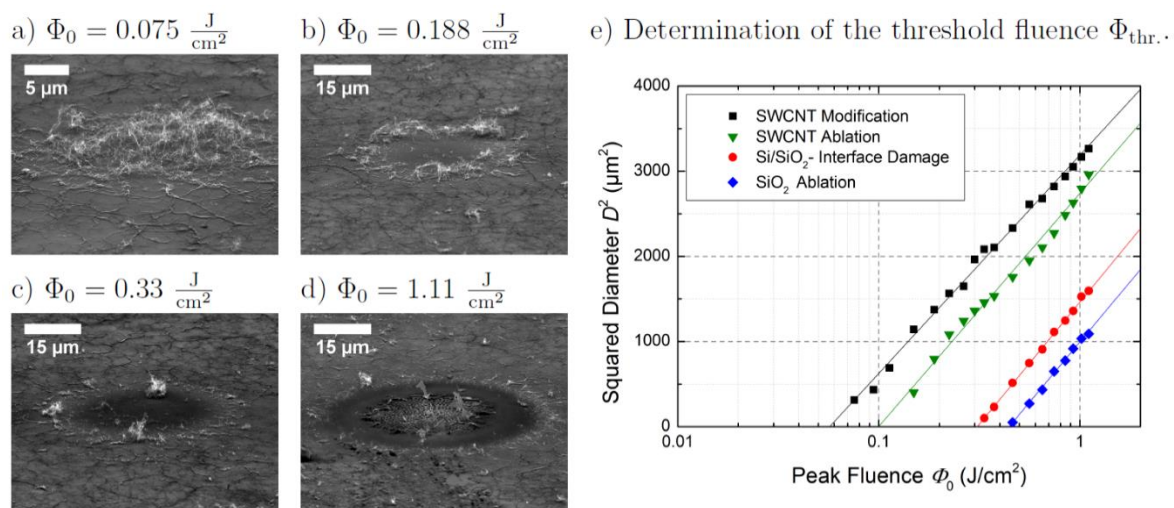

Figure 4-2 FESEM images at 70° to the surface of ablated areas at 4 different peak flueces representing the characteristic laser modification regime. (a) Visible modification of the CNT network without ablation. (b) ablation of the CNT network. (c) visible Si/SiO$_2$ damage at the interface. (d) Delamination of the SiO$_2$ layer. (e) Displays the threshold fluences determined for the aforementioned regimes, determined via the D^2 method. (Laser parameters: λ= 1030 nm, τ= 470 fs, ω$_0$ = 26 μm) [Results published in [103]]

This big variation in threshold results from varying laser wavelengths as well as pulse durations. At peak fluences between 0.300 J/cm^2 and 0.445 J/cm^2 results in irreversible damage to the SiO_2 at the film interface. This ablation threshold for SiO_2 was investigated in previous works [107], [108]. Beyond peak fluences of 0.445 J/cm^2 the SiO_2 is completely removed.

In order to better characterize the modification regime, $(0.0057 \ J/cm^2 \leq \Phi_0 < 0.100 \ J/cm^2)$ which exhibits a local debundling of CNT bundles and visible bulging of the film, higher magnification SEM images were taken. Figure 4-3 a displays a pristine film, where a homogenous CNT film is visible with some visible bundles. Figure 4-3 b displays a CNT film exposed to a single spot at $\Phi_0 = 0.075 \ J/cm^2$. Clear differences can be observed when compared to the stock film with the most dominant, from a top down perspective, being the local debundling.
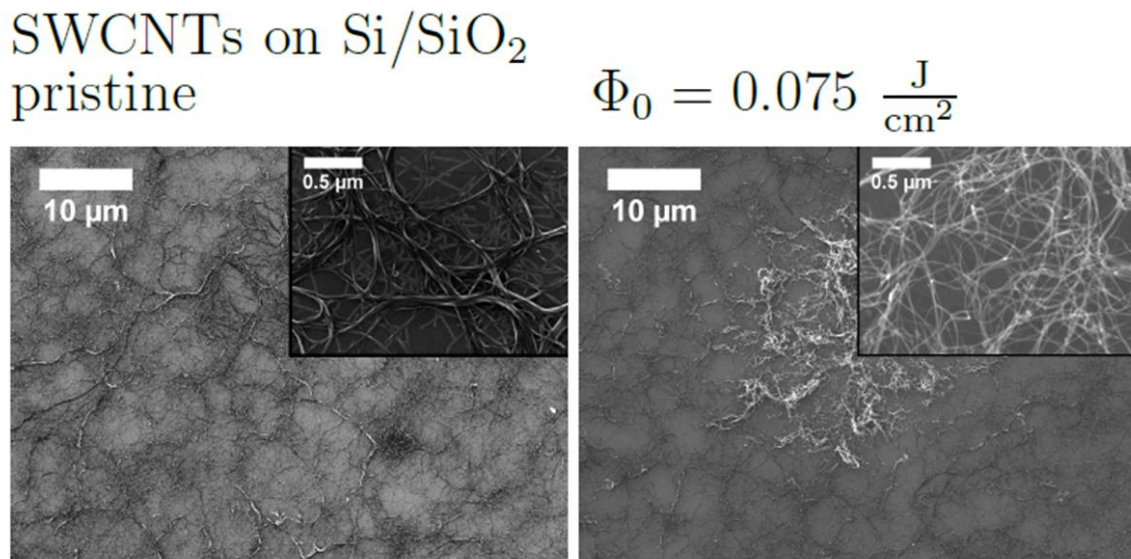

Figure 4-3 SEM images comparing (a) pristine and (b) irradiated films ($\Phi_0 = 0.075 \ J/cm^2$) CNT films on Si/SiO_2. Inlets show a higher magnification of the central area. Visible is a prevalent debundling in the irradiated film. (Laser parameters: $\lambda = 1030$ nm, $\tau = 470$ fs, $\omega_0 = 24$ µm) [Results published in [103]]

To better quantify the difference, bundle diameters d_B were extracted from the SEM image and plotted in Figure 4-4. Bundle diameters in the pristine network range from 3 to 40 nm with a peak (12%) at around 7 nm with a log normal distribution, which is consistent with literature [109]. The irradiated film at $\Phi_0 = 0.075 \ J/cm^2$ exhibits significantly smaller d_B ranging from 2 to 20 nm with a peak (26%) at 5 nm with a similar log normal distribution. The numerical values are consistent with the optical interpretation that a local debundling is performed. Rather than a shift in distribution, a reduction of the distribution range is seen. The implications being that a debundling can be performed post deposition in ambient

processing conditions. From a device engineering point of view this allows such processed films to show better electrical performance as shown in [110] where degree of debundling is strongly correlated to the optoelectrical performance of the film. Furthermore for semiconducting devices such as TFTs a better debundling could improve I_{ON}/I_{OFF} ratios as electrical transport is dominated by metallic tubes in bundles [82]. With regards to the bulging using an approach proposed by Peigney et. al. [111] to calculate surface area of bundles, we can calculate the increase in surface area due to debundling. Taking into account the decrease in diameter a surface area increase of ca 40% post laser modification. The assumption being that the number of CNTs remains constant.
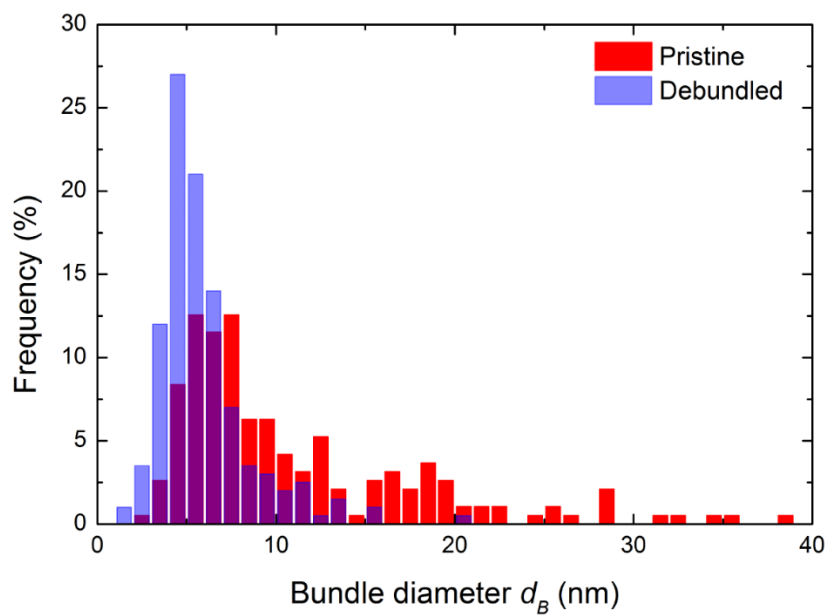

Figure 4-4 Histogram of bundle diameter distribution of pristine CNT (red) and an irradiated film Φ_0 = 0.075 J/cm^2 (blue) on Si/SiO$_2$. Bundle diameters for the pristine film exhibit values between 3 nm and 40 nm with a peak at around 7nm. The irradiated film exhibit values between 2 nm and 20 nm with a peak at around 5 nm. [Results published in [103]]

In order to move beyond a niche application on SiO$_2$ it is necessary to show a proof of concept on other underlying substrates. Due to the various possible ablation mechanisms as well as matter interaction, a simple ablation experiment on the blank substrates would not suffice. As such, we have selected a polyimide film (Kapton) onto which we deposited a CNT film on. Similarly, to SiO$_2$ using the D^2-method, threshold fluences are determined. . Figure 4-5 displays (a)-(d) SEM images of a CNT film irradiated at different peak fluences in addition to the resulting plot for the D^2-method. The SEM images (a)-(d) show representative films in the different laser processing regimes. These regimes can be separated

into three distinct categories: (a) at peak fluences between 0.038 J/cm^2 and 0.089 J/cm^2 a modification of the CNT layer can be observed. (b) At peak fluences between 0.089 J/cm^2 and 0.700 J/cm^2 an ablation of the CNT film is observed. Beyond peak fluences of 0.700 J/cm^2 the polyimide is visibly damage. Although not identical to the SiO$_2$ substrate, the ablation and modification regimes are closely matched.
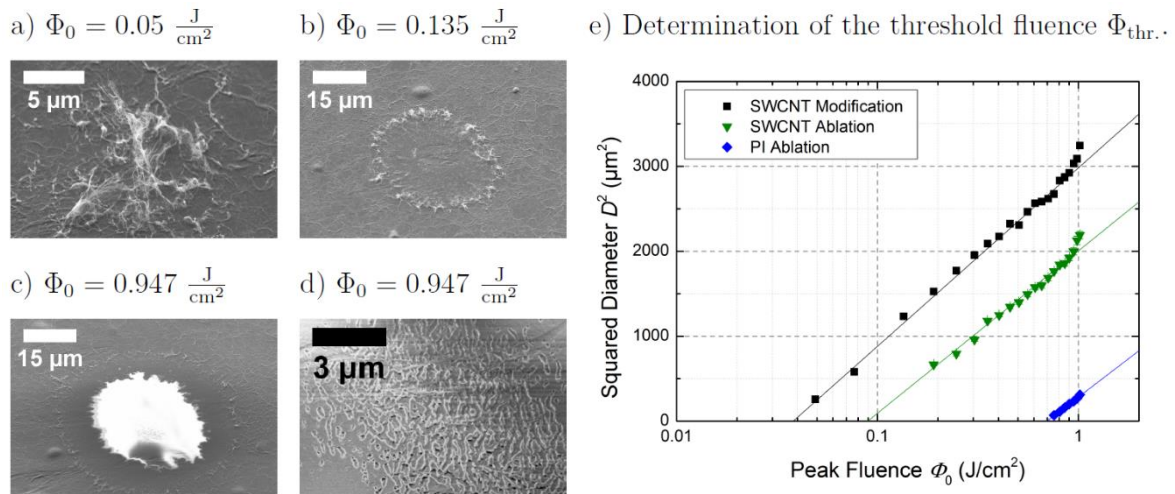

Figure 4-5 FESEM images at 70° to the surface of ablated areas at 3 different peak flueces representing the characteristic laser modification regime. (a) Visible modification of the CNT network without ablation. (b) ablation of the CNT network. (c) visible polyimide damage at the interface. (d) zoom in of center area of (d). (e) Displays the threshold fluences determined for the aforementioned regimes, determined via the D^2 method. (Laser parameters: λ= 1030 nm, τ= 470 fs, ω$_0$ = 24 μm) [Results published in [103]]

To summarize; both substrates exhibit similar results regarding the ablation and modification thresholds. In addition, it can be said that as long as the ablation threshold of the substrate is significantly above the ablation threshold of the CNT film laser processing could be a viable option, taking into account the limited sample size. Although these proof of concept experiments show the viability of the femtosecond single pulse ablation of CNTs a wide range of experiments need to be performed in order to fully comprehend the interaction between laser pulse and CNT film. Furthermore, the degree to which certain parameters affect the processing thresholds needs to be investigated.

4.4 Selective Ablation

As previously mentioned, one important factor regarding laser ablation is the laser wavelength. This ties in directly with the absorption spectrum of CNTs as this directly regulates the absorption and resulting ablation thresholds. In literature, it has been shown

that semiconducting and metallic CNTs display differing absorption spectra in addition to the diameter dependent absorption spectra [112], [113]. From an engineering point of view, this implies that it could be possible to selectively ablate CNTs based on diameter and/or CNT type, if operating the laser below ablation threshold and using a preferential wavelength. In order to investigate this we irradiated two samples on SiO_2, with two different wavelengths namely at near infrared (1030 nm) and green (520 nm). In concordance with absorption spectra from literature, a shift to lower ablation thresholds, in the D^2-Method, would be expected when switching near IR to green. This shift is also consistent with the composition of the CNT films that is in a ratio of 2:1 semiconducting to metallic. Figure 4-6 displays (a)-(d) SEM images of a CNT film irradiated at different peak fluences at λ= 1030 nm in addition to the resulting plot for the D^2-method. The SEM images (a)-(d) show representative films in the different laser processing regimes. These regimes can be separated into four distinct categories: (a) at peak fluences between 0.036 J/cm^2 and 0.076 J/cm^2 a modification of the CNT layer can be observed. (b) At peak fluences between 0.078 J/cm^2 and 0.210 J/cm^2 an ablation of the CNT film is observed. Beyond peak fluences of 0.330 J/cm^2 the SiO_2 is completely removed. The four distinct laser-matter interaction regimes are clearly separated and visible.
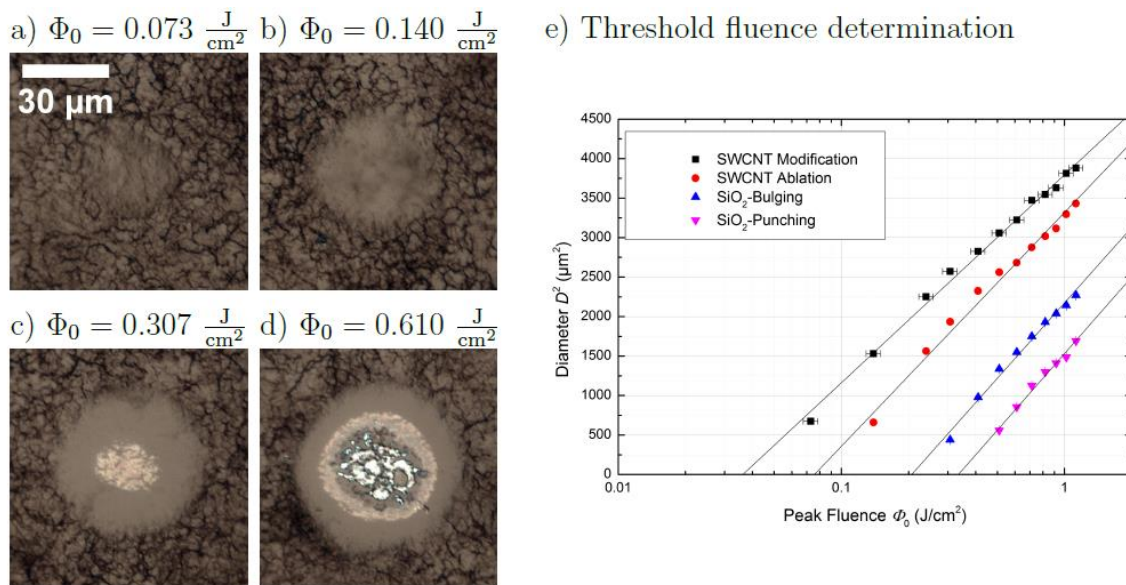

Figure 4-6 Microscope images of ablated areas at 4 different peak fluences representing the characteristic laser modification regime of a CNT network on Si/SiO_2 substrate when exposed to a near IR laser. (a) Visible modification of the CNT network without ablation. (b) ablation of the CNT network. (c) visible Si/SiO_2 damage at the interface. (d) Delamination and buldging of the SiO_2 layer. (e) Displays the threshold fluences determined for the aforementioned regimes, determined via the D^2 method. (Laser parameters: λ= 1030 nm, τ= 470 fs, ω_0 = 24 µm)

Figure 4-7 displays (a)-(d) SEM images of a CNT film irradiated at different peak fluences at λ= 520 nm in addition to the resulting plot for the D^2-method. The SEM images (a)-(d)

show representative films in the different laser processing regimes. These regimes can be separated into four distinct categories: (a) at peak fluences between 0.022 J/cm^2 and 0.054 J/cm^2 a modification of the CNT layer can be observed. (b) At peak fluences between 0.054 J/cm^2 and 0.120 J/cm^2 an ablation of the CNT film is observed. Beyond peak fluences of 0.220 J/cm^2 the SiO$_2$ is completely removed. In contrast to the 1030 nm D^2-Method regimes, a visible shift to lower thresholds for all regimes is visible. As previously mentioned, this observed shift is consistent with the absorption spectra of a film consisting of more semiconducting CNTs.
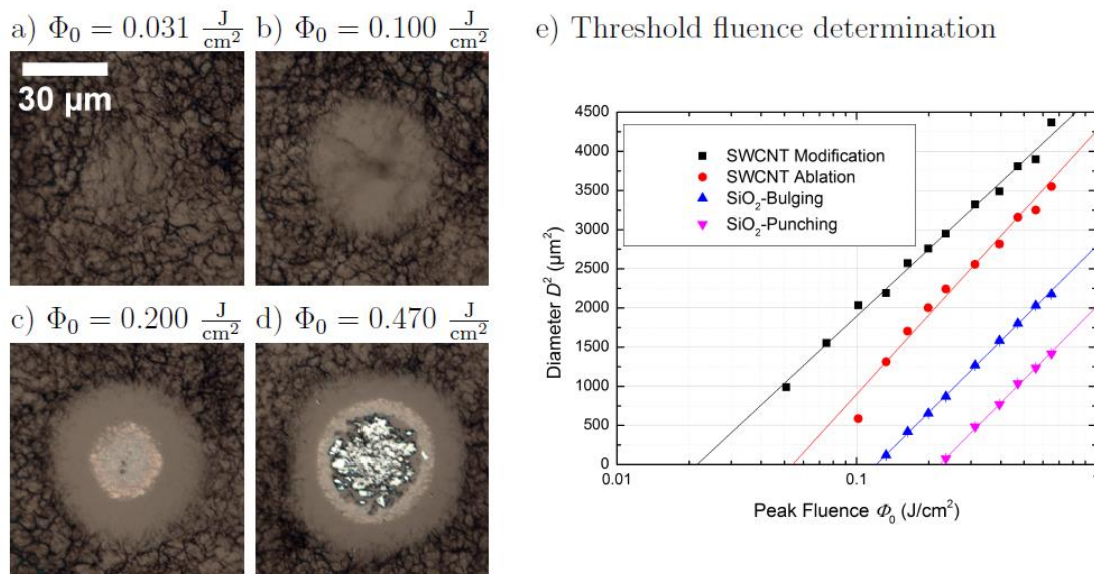

Figure 4-7 Miscroscope images of ablated areas at 4 different peak flueces representing the characteristic laser modification regime of a CNT network on Si/SiO$_2$ substrate when exposed to a green laser. (a) Visible modification of the CNT network without ablation. (b) ablation of the CNT network. (c) visible Si/SiO$_2$ damage at the interface. (d) Delamination and buldging of the SiO$_2$ layer. (e) Displays the threshold fluences determined for the aforementioned regimes, determined via the D^2 method. (Laser parameters: λ= 520 nm, τ= 470 fs, ω_0 = 25 µm)

Although the above presented results are indicative of a possible wavelength selective ablation, further investigation is required in order to make a more precise statement in addition to the effectiveness of this feature of the laser ablation method.

4.5 Multi Pulse Laser Ablation

After highlighting the single pulse laser ablation of CNT networks and identifying the various material ablation regimes, the focus will be shifted to multi pulse ablation. Multi pulse ablation is required for line processing and large area patterning. The core strategy if

to overlap single pulses to a certain degree. From previous laser ablation experiments it is known that overlapping laser pulses results in a decrease in ablation threshold fluences [114]–[116]. The reason for this decrease is due to thermal residues from previous pulses, as such energetically speaking, less energy is required of each individual pulse. For our multi pulse experiments the effective laser repletion rate f_{eff}= 1500 Hz which corresponds to a 0.7 ms temporal spacing between pulses. For the initial investigation, lines were patterned on both Si/SiO$_2$ and PI with widely varying PPP. Figure 4-8 shows optical microscope images of multi pulse from PPP= 1.66 to PPP= 20 with the peak laser fluences ranging in the previously determined ablation regimes namely peak fluences of 0.150 J/cm^2 to 0.300 J/cm^2 for Si/SiO$_2$ and 0.120 J/cm^2 to 0.300 J/cm^2 for PI. Visibly no real distinction for both substrates is visible other than the SiO$_2$ damage at 0.300 J/cm^2 onwards of 10 PPP. As such, we will limit ourselves to the Si/SiO$_2$ substrate for the more detailed discussion.
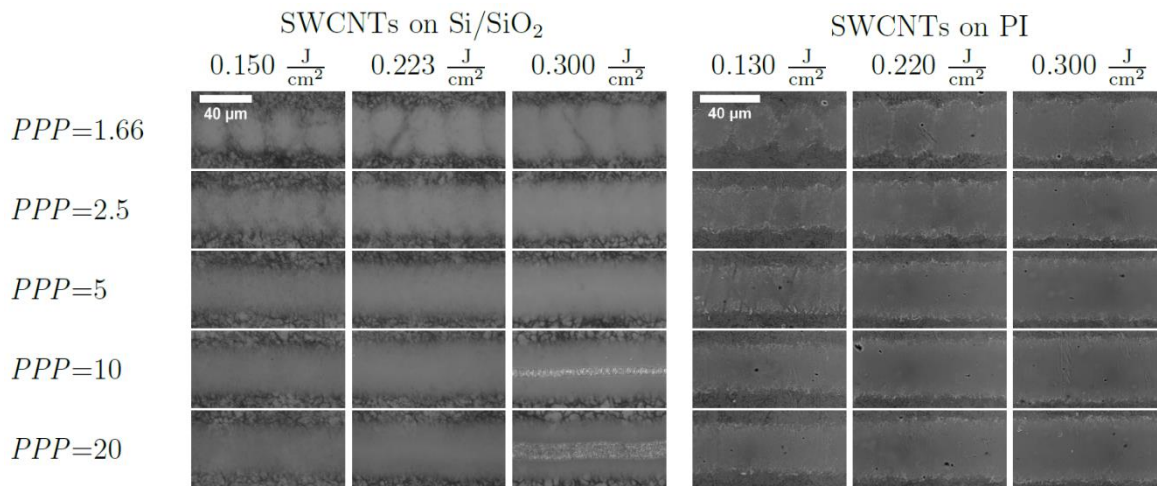

Figure 4-8 Optical microscope image of multi pulse ablation experiments on: left: CNTs on Si/SiO$_2$ right: CNTs of PI. Laser fluences (Φ_0) are labelled horizotally, while the PPP are labbeled vertically. The laser polarization is horizontal. (Laser parameters: λ= 1030 nm, τ= 470 fs, ω_0 = 24 μm, f_{eff}= 1500 Hz) [Results published in [103]]

With an increase in PPP a smoothing of the line can be observed with increase definition of the line edge. However, with increasing PPP the line width decreases. An example of this is the decrease from 24 μm at PPP = 2.5 at Φ_0 = 0.225 J/cm^2 to 18μm at PPP = 20 at Φ_0 = 0.225 J/cm^2. From this result, we can hypothesize that with increasing PPP the ablation threshold increases. This is contrary to previous laser ablation experiments performed on other materials [117], where as previously mentioned, with increasing PPP the ablation threshold should decrease. In order to further investigate this effect, we measure the ablated line width D_L for lines ablated at Φ_0 = 0.225 J/cm^2 with varying PPP and extract the threshold fluence. and compare them to threshold fluences from Si/SiO$_2$ abltation threshold fluences at Φ_0 = 0.316 J/cm^2. The results are summarized in Figure 4-9. For the Si/SiO$_2$ material system a decrease in threshold fluence from 0.310 J/cm^2 (1 PPP) to 0.140 J/cm^2 (20 PPP) is visible.

As mentioned before this is consistent with previous experiments and with the assumptions made as to the interactions of multi pulse ablation. For the CNT film the ablation threshold rises from 0.100 J/cm^2 (1 PPP) to 0.170 J/cm^2 (20 PPP). The increase in most pronounced from 1 PPP to 10 PPP with the effect saturating afterwards.
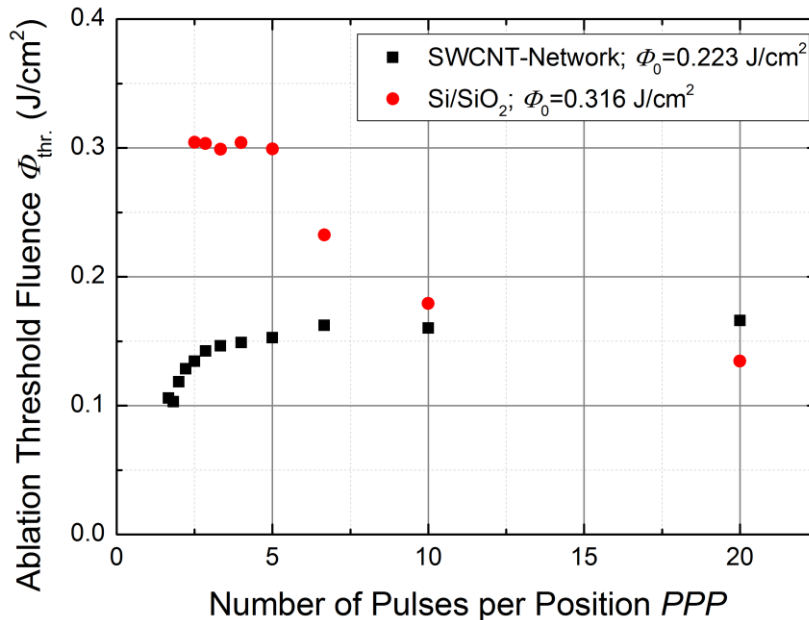

Figure 4-9 displays the calculated threshold fluence (Φ_{thr}) as a function of PPP. The red dots show the Φ_{thr} for Si/SiO$_2$ with the laser fluence (Φ_0) at 0.316 J/cm^2. Clearly visible is a decrease in ablation threshold with increasing PPP. The black dots show the Φ_{thr} for CNTs with Φ_0 at 0.223 J/cm^2. With increasing PPP the ablation threshold increases. (Laser parameters: λ= 1030 nm, τ= 470 fs, ω_0 = 24 µm, f_{eff}= 1500 Hz) [Results published in [103]]

We attribute the different varying behavior to a strong thermal annealing of individual CNTs, leading to healing of structural defects. Such a thermal assisted structure healing has been shown in literature [118]–[120], to help reestablish the honeycomb structure thus improving the structural stability of the CNTs. Such an increase in structural stability would increase the ablation threshold of the material. Thus, the initial pulses anneal the material, with subsequent pulses then interact with the healed material structure; as such higher energy levels are required. Another hypothesis, as to the increase in ablation threshold with increasing PPP, is that the initial pulse produces debundeling at the edge of the pulse, see 4.3. The debundeled regions present a higher number of tubes with higher number of interconnections to adjacent tubes. This network is better intertwined and as such would require higher energetic level to separate.

Taking both the decrease in ablation threshold with higher PPP of the Si/SiO$_2$ system and the increase in ablation threshold with higher PPP of the CNT network, the processing

window for line processing of CNTs on Si/SiO$_2$ becomes narrow. An additional caveat is that the ablation threshold for Si/SiO$_2$ under the CNT film is further decreased due to the field enhancing behavior exhibited by CNTs. This characteristic has been observed and reported in literature [106]. Taking the aforementioned effects into account the peak fluence was limited to 0.223 J/cm^2. The PPP range was selected between 5 and 20 PPP as this was the best tradeoff between line roughness, processing speed and risk to damage the substrate. Optical images can be reviewed in Figure 4-8 (a). The same experiment was performed on the PI substrate. In this case however due to the significantly higher threshold for substrate damage (0.700 J/cm^2), the peak fluence is not limited. Optical images of CNT films can be reviewed in Figure 4-8 (b). To ensure the complete ablation of the CNTs, electrical 2-point resistive measurements were performed resulting in open circuit measurements in the 10^{10} Ω range.

Having established the process window for the galvanic separation of films and as such the ability to pattern the CNT film on both Si/SiO$_2$ and PI substrates, a framework was also developed for future experiments on varying substrates. The following investigation was to observe if ultra-short laser ablation could provide further functionality beyond simple galvanic isolation of a larger scale.

4.6 Laser Assisted Functionalization

As mentioned in the previous section, the following investigation is focused on the ability to functionalize the CNT film with the assistance of ultra-short pulse laser irradiation. Due to the unique physical shape of CNTs, namely their extraordinary aspect ratio, the interaction between polarized laser light incident and the orientation angle of the CNT should vary greatly as the overlapping area greatly varies. Following this hypothesis we irradiated CNT films on Si/SiO$_2$ and PI close to the previously established modification threshold of 0.051 J/cm^2 for Si/SiO$_2$ and 0.031 J/cm^2 for PI. The expected result would be that CNT whose alignment matched the polarized the laser would be ablated while those perpendicularly aligned would remain on the substrate. SEM images were taken and are visible in Figure 4-10. In the top row, the laser is parallel polarized while in the bottom row perpendicular polarized. This has also been illustrated with a red arrow. Figure 4-10 a shows the Si/SiO$_2$ substrate with two peak fluences below and above the modification threshold namely 0.051 J/cm^2 and 0.084 J/cm^2 at 20 PPP. For the PI substrate in Figure 4-10 b peak fluences of 0.049 J/cm^2 and 0.129 J/cm^2 were used at 20 PPP. Clearly visible for all scenarios is the perpendicular alignment of the CNT to the polarization of the laser. Although an alignment is visible this is still a top down method as can clearly be seen due to the significantly lower CNT density when compared to the non irradiated area. In addition to the observed

alignment, while under the modification threshold the previously observed local debundling can be observed that was also present in the single pulse ablation (see 4.3)
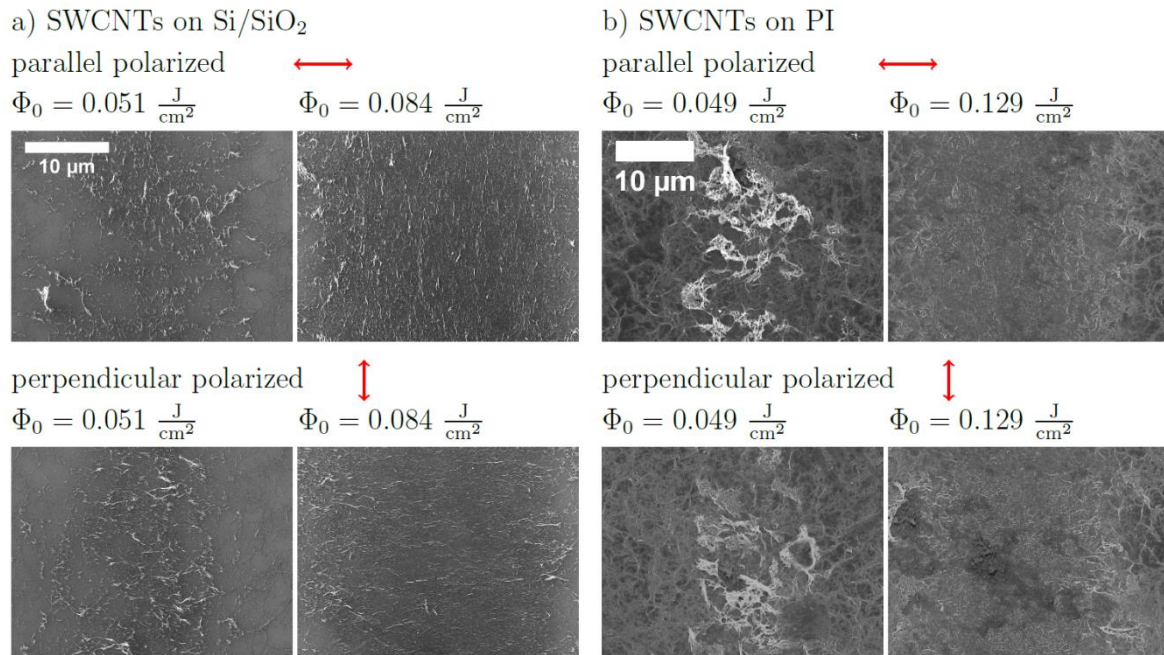

a) SWCNTs on Si/SiO$_2$
parallel polarized
$\Phi_0 = 0.051 \frac{J}{cm^2}$ $\Phi_0 = 0.084 \frac{J}{cm^2}$

b) SWCNTs on PI
parallel polarized
$\Phi_0 = 0.049 \frac{J}{cm^2}$ $\Phi_0 = 0.129 \frac{J}{cm^2}$

perpendicular polarized
$\Phi_0 = 0.051 \frac{J}{cm^2}$ $\Phi_0 = 0.084 \frac{J}{cm^2}$

perpendicular polarized
$\Phi_0 = 0.049 \frac{J}{cm^2}$ $\Phi_0 = 0.129 \frac{J}{cm^2}$

Figure 4-10 FESEM images of CNT networks on (a) Si/SiO$_2$ and (b) PI substrates. Varying peak fluences (0.051 and 0.084 J/cm^2 on Si/SiO$_2$) (0.049 and 0.129 J/cm^2 on PI) at 20 PPP and laser polarization (parallel and perpendicular polarization) were used to irradiate the CNT film. The red arrow indicates the polarization of the laser for the coresponding images. With a visible perpendicular allignement to the laser polarization. (Laser parameters: λ= 1030 nm, τ= 470 fs, ω_0 = 24 µm, f_{eff}= 1500 Hz) [Results published in [103]]

In order to characterize and better visualize the degree of alignment, the SEM images from Figure 4-10-a at 0.084 J/cm^2, for both parallel and perpendicular polarization, were analyzed using image processing software with respect to the orientation angle. Orientation angle of 0° corresponds to a horizontal alignment while 90° corresponds to a vertical alignment. Figure 4-11 a) represents the distribution angles of the remaining CNTs after irradiation with (red) perpendicular polarized laser and (black) parallel polarized laser. The peak values of the distributions are at 0° and 90° for the perpendicular polarization and perpendicular polarization respectively. The standard deviation from peak are 23° for the perpendicular and 24° for the parallel polarization. These numerical values coincide with the optical image of the SEM images. A further observation regarding the distribution is that the CNTs parallel to the laser light are not fully ablated. This has further implication for further applications as with a more complete ablation it would be possible to have in-situ alignment, which was previously only possible by complex in quartz trenches directional growth [121], [122].
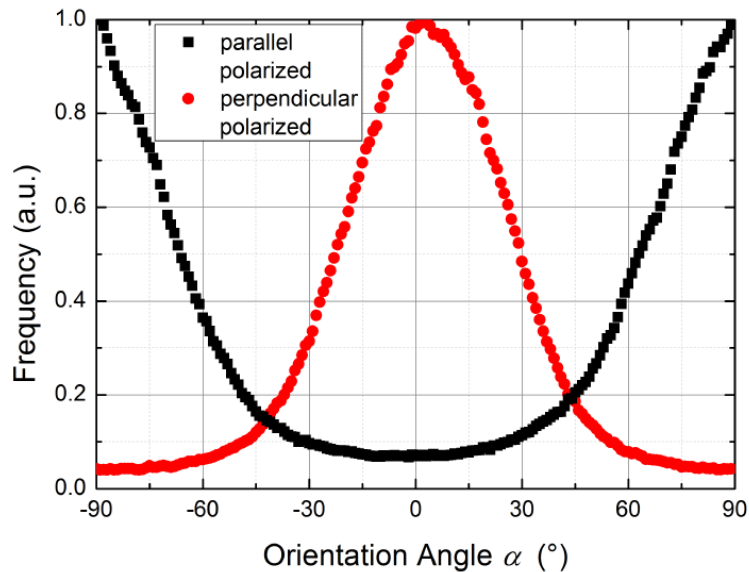
Figure 4-11 displays the normalized frequency density with respect to the orientation angle for (red) perpendicular and (black) parallel laser polarization irradiated CNT films on Si/SiO_2 at a peak fluence of 0.084 J/cm^2 at 20 PPP. 0° Corresponds to a horizontal CNT alignment. The distributions are extracted from fig 4-10 a. Standard deviations are 23° and 24° for perpendicular and parallel laser polarization respectively. [Results published in [103]]

In order to further investigate the degree to which it is possible to fully ablate CNTs in a given direction, we increased peak fluences from 0.015 J/cm^2 to 0.130 J/cm^2 at 20 PPP on the Si/SiO_2 substrate with parallel and perpendicular laser polarization. In addition from an electrical engineering perspective a key factor is the behavior development of the irradiated film with increasing alignment. As such we then subsequently performed 2-point DC resistive measurements and plotted the ratio in comparison to a pristine film $R_{pristine}/R_{aligned}$. Each point represents an average of ten devices. Figure 4-12 displays the plot summarizing the measured results. The aligned networks (red) perpendicular polarized laser and (black) parallel polarized laser both show an increase in the measured resistance with increasing peak fluence. Under 0.050 J/cm^2 the change in resistance is minimal with the ratio remaining close to 1 for both polarization. This is attributed to the irradiation energy being too small to ablate a significant number of CNTs to affect the percolation paths across the terminals. From 0.067 J/cm^2 a more pronounced difference between the polarizations is visible as the resistance for the parallel polarization increases to a factor of 2 while the perpendicular polarization is 1.12. Percolation paths are visibly interrupted from this threshold. From a geometrical perspective this is also consistent as vertically aligned CNT have a minimal contribution to the charge transport. The increase in ratio is consistent until the last peak fluence of 0.130 J/cm^2 with the ratio between the perpendicular irradiated film and the parallel irradiated film reaching a maximum of 10^4. This proves that it is possible to engineer directional electrical transport in previously randomly aligned films with the aid of ultra-short pulse laser ablation.
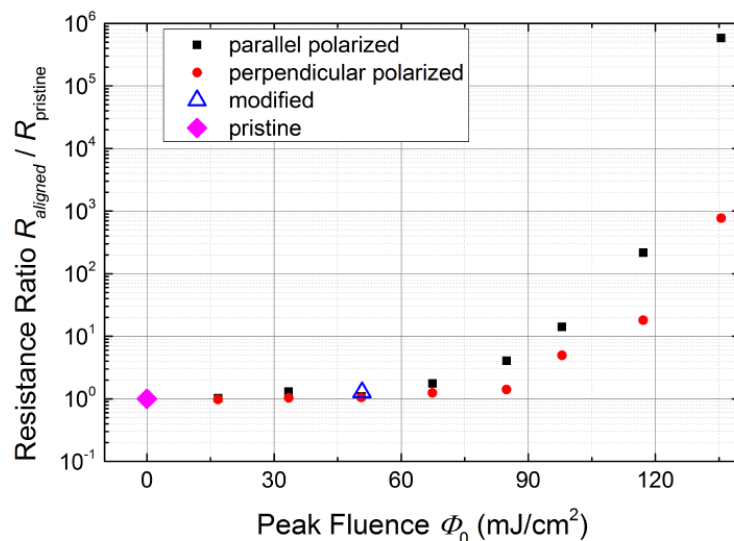
Figure 4-12 displays a semi logarithmic plot of the resistance ratio $R_{alligned}/R_{prisine}$ as a function of the peak incidental laser fluence (PPP = 20) with a parallel polarization (black) and perpendicular polarization (red). The CNT film is deposited on Si/SiO$_2$ with the resistance being measured as a 2-point across the irradiated line. Each point represents an average from 10 devices. (Laser parameters: λ= 1030 nm, τ= 470 fs, ω_0 = 24 µm, f_{eff}= 1500 Hz) [Results published in [103]]

Although the alignment of CNTs using polarized laser irradiation is effective it still is a destructive method as the increase in resistance in comparison to the pristine film at the peak fluence still represents an increase in resistance of almost 10^3. This process characteristic needs to be taken into account when designing future devices based on this technology and planning with a significantly higher starting CNT film thickness.

All multi pulse laser experiments until this point were performed with an infrared laser with a wavelength of λ = 1030 nm. With the previously expressed hypothesis (see 4.4) that it would be possible to ablate differing types of CNTs based on the wavelength of the laser, we repeated the polarization dependent ablation with an additional laser wavelength of λ = 520 nm. Due to the ratio of 2:1 semiconducting to metallic CNTs present in the fabricated films, it is to be expected that a varying characteristic based on the laser wavelength to be visible based on the varying absorption spectra. Figure 4-13 displays the results of the electrical characterization plotting the resistance ratio ($R_{pristine}/R_{aligned}$) in relation to the peak fluence. Each dot set represents a different polarization with the initial pristine network markes as reference. Figure 4-13 a) is consistent with the initial characterization as it is a replication of the initial experiment with a laser wavelength of λ = 1030 nm. The characteristic modifiactions regimes were evaluated and extracted from microscope images. Figure 4-13 b) displays the plot for λ = 520 nm. A clear distinction is visible with a strong shift towards lower fluences. The modification regime shifted by 14mJ/cm^2 corresponding to an approx. 40% decrease while the ablation threshold shifted by 22mJ/cm^2 corresponding

a) $\lambda_F = 1040$ nm   b) $\lambda_{SHG} = 520$ nm

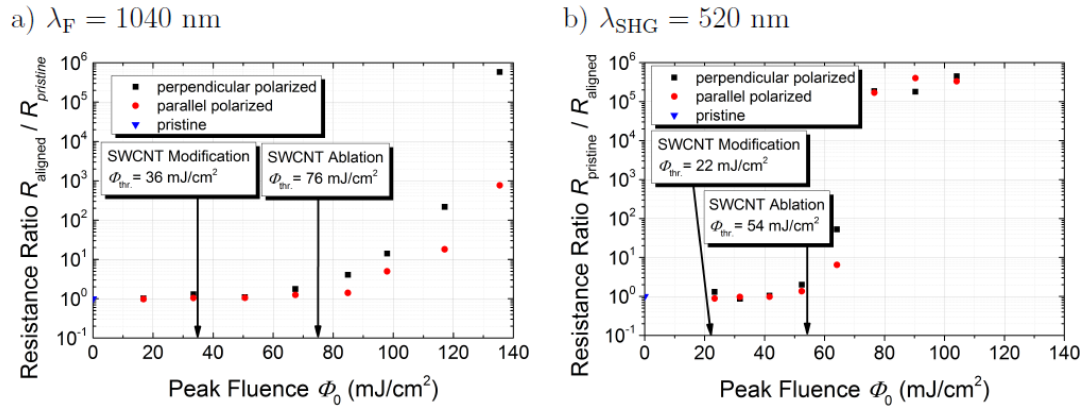Figure 4-13 Electrical measurements of pattened cuts made into a 2:1 semiconducting to metalic CNT film at wavelenghts of both 520 nm (a) and 1040 nm (b). Presented is the ratio between the patterned line both with perpendicular as well as parallel polarized laser with increasing laser fluences. The threshold fluences for both CNT modification and ablation are indicated. ((a) Laser parameters: λ= 1040 nm, τ= 550 fs, ω_0 = 24 µm and PPP =20) ((b) Laser parameters: λ= 520 nm, τ= 470 fs, ω_0 = 25 µm and PPP = 20)

to an approx. 29% decrease. This change is consistent with the previously stated hypothesis that a selective ablation is possible. A clear distinction is also the progression of the perpendicular and parallel polarization resistance ratios with increasing fluence. While for the λ = 1030 nm sample, a continuous increase in separation is distinct, for the λ = 520 nm sample this trend is only visible until 75mJ/cm^2 at which the film is no longer is conducting. This behavior is consistent with the formation of percolating paths based on CNT type. At λ = 1030 the metallic paths are preferentially ablated. These metallic paths are supplementary to the semiconducting paths and as such, more controlled and finer ablation is possible. So far, these experiments are only a proof of concept and require significant further investigation to make statements beyond the proof of viability.

4.7 Summary

In this chapter, we demonstrated the use of a femtosecond laser operated in both single and multi pulse regimes with and without polarization for the ablation and modification of spray deposited carbon nanotube films. Initially a brief summary of the previous fields in which this process has been successfully used in is given. The operation and key parameter extraction such as certain fluence thresholds are described. The investigation into the laser pulse CNT film interaction was performed both on SiO_2 and polyamide as to exclude a possible substrate limitation. In this investigation key regimes were identified: a) Visible modification of the CNT network without ablation. (b) ablation of the CNT network. (c) visible Si/SiO_2 damage at the interface. (d) Delamination of the SiO_2 layer. These regimes

were identified with the aid of a field enchanched scanning electron microscope. These experiments were also performed for the multi pulse regime with the surprising result of regime thresholds increasing in amplitude rather then decreasing as is common with more classic materials such as SiO_2. This is a result of the unique nature of CNT films were in-situ debundeling increases binding sites to neighboring tubes thus increasing the energy required to remove them form the film. Following this we showed that it is possible to galvanically separate films as such allowing for the use of this technique as a paterning tool. In addition to simple separation we investigated the effects of polarized laser light. Here we displayed the capability to ablate CNT based on orientation with a 90° corelation to the polarization of the laser light. This is due to the reduced absorption of the light when mis alligned to the incident laser. We characterized the efficency of this method both electrically with regard to the resistance of the remaining film as well as optically with the aid of SEM images. Here we perfored an angle analasys on the remaining films showing the peak values of the distributions at 0° and 90° for the perpendicular polarization and perpendicular polarization respectively. The standard deviation from peak are 23° for the perpendicular and 24° for the parallel polarization. This is a proof of concept for a post deposition alignment technique previously reserved to directed chemical vapor deposition growth, an expensive and complex process. Finally, we also introduced the possibility that CNTs could be ablated based on their electrical properties as these are correlated to the absorption spectra as such metallic CNTs would have a lower ablation threshold at 550 nm for example in contrast to semiconducting CNTs. This method requires further investigation but gives promise of a technique that could be used as an alternative for very expensive separation technique that lead to exponentially higher material prices. Furthermore it would allow for the improvement of thin-film transistors with the possibility to remove parasitic metallic CNTs post deposition.

Chapter 5

CNT Thin-Film: Field Effect Transistors

5.1 CNT Thin-film Transistors Overview

Thin-film transistors, short TFTs, belong to the family of IGFETs (insulated gate field-effect transistors) and are voltage controlled 3-terminal switching devices. They defining physical characteristic is the sub 50 nm active channel thickness. Conventional TFTs are fabricated with amorphous Si as semiconducting layer, but since the 1980s organic materials such as polymers or semiconducting CNTs and have been introduced [123]. The assembly is similar to the MOSFET (metal oxide semiconducting field-effect transistor)-structure: two electrodes, referred to as source and drain, are electrically connected via a semiconducting organic thin-film. A third electrode, the gate, is isolated from drain, source and semiconductor by the insulating gate dielectric. Compared to inorganic TFTs they are easy to process and can be fabricated at large scale and on flexible substrates, e.g. plastic.

5.1.1 Charge transport

Applying a voltage between gate and source contact V_{GS} across the dielectric generates mobile charge carriers in the semiconducting organic layer. A current flow between the drain and the source contact I_{DS} is enabled, if a second voltage V_{DS} is applied across the semiconductor. Since the active layer in OTFTs is usually intrinsic, the transistor operates in accumulation mode. For a p-type channel, holes are the charge carriers, which accumulate near the interface of dielectric and semiconductor, if a negative gate voltage is applied. For a n-type channel, electrons are the charge carriers, which accumulate near the interface of dielectric and semiconductor if a positive gate voltage is applied. Schematically the energy band diagram of an OTFT is depicted in Figure 5-1. Different from inorganic

semiconductors the energy levels in organic materials are referred to as HOMO (highest occupied molecular orbital) and LUMO (lowest unoccupied molecular orbital). E_F and Φ represent the Fermi level and the work function of the respective material. The diagram on the left a) shows the MIS (metal insulator semiconductor)-structure of $V_{GS} < 0$ V. Positive charge carriers accumulate near the dielectric interface. The diagram on the right b) shows the energy bands across the p-channel at $V_{GS} < 0$ V and $V_{DS} < 0$ V. Due to the potential difference of source and drain, positive charge carriers travel along the HOMO through the organic material. Electron transport in the semiconductor is blocked, as the energy barrier between the Fermi level of the drain contact $E_{F,D}$ and the LUMO of the semiconductor is large.
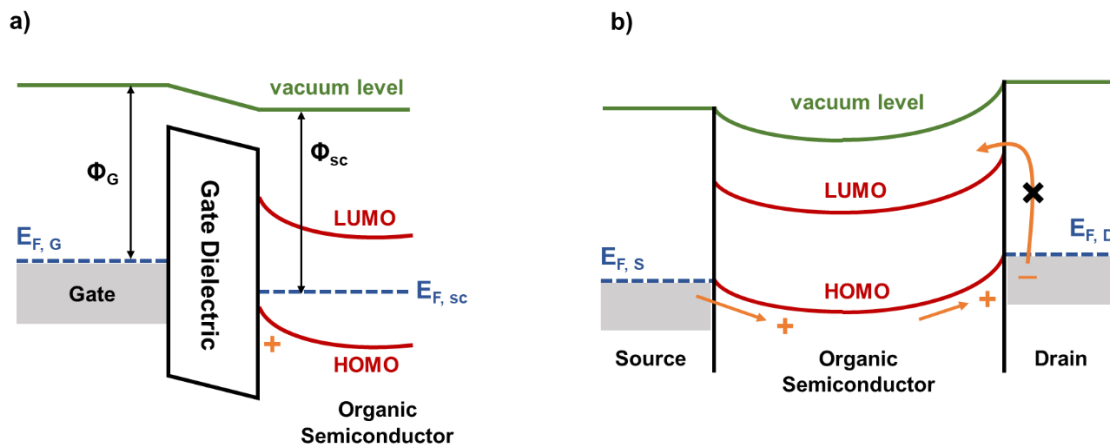

Figure 5-1 Energy-level diagrams of a p-channel OTFT: a) across the interface of the gate contact and the organic semiconductor. If $V_{GS} < 0$ positive charge carriers accumulate at the interface. b) along the active layer between source and drain electrodes. If $V_{GS} < 0$ and $V_{DS} < 0$ positive charge carriers travel from the source to the drain contact. The high energy barrier between the drain Fermi level and the LUMO prevents electron conduction.

From simulation models and experimental data the band gap between HOMO and LUMO of semiconducting CNTs was determined to:

$$E_G = \frac{2\gamma_0 a_{c\text{-}c}}{d} \approx 0.7 \, \frac{eV}{d} \tag{7}$$

With $\gamma_0 = 2.45$ eV being the nearest neighbor overlap integral, $a_{c\text{-}c} = 0.142$ nm being the inter-atomic spacing between to adjacent carbons and d being the tube diameter in nanometer [21]. Due to the spin degeneracy and the sub-lattice degeneracy of graphene CNTs have four 1D subbands in parallel. Thus the conductance is given by the 1D Landauer Formula:

$$G = \frac{4e^2}{h} \cdot T \tag{8}$$

Where T is the transmission coefficient of charge carriers through the tube, e is the electron charge and h is the Planck constant [46]. For ballistic transport, T becomes one and the tube resistance calculates to 6.5 k Ω. However, for nanotubes with a length $L_{nt} > 10$ nm the transport of charge carriers in CNTs appears to be rather diffusive than ballistic at ambient temperature due to scattering [37], [39]. For uniform diffusive scattering is the steady state tube resistivity given by:

$$R_{nt} = \frac{h}{4e^2} \cdot \frac{L_{nt}}{l} \qquad (9)$$

with L_{nt} being the length of the nanotube and l being the mean free path of an electron along the tube [124]. The mean free path l in CNTs is influenced by several parameters, such as the structure of the tube, the lattice perfection, the shape, the length of the tube and the environmental temperature. For example can the type of substrate alter the travelling distance of a charge carrier in CNTs, as suspended tubes show near-ideal transport characteristics. This indicates that disorders in a tube occur mostly due to interaction with the substrate. Indeed, CNTs adjust their shape to the topology of the substrate and rough substrates can add additional scattering sites to the nanotube [37], [124]. Moreover, the mean free path decreases non-linearly with increasing temperature. At low temperatures, scattering sites occur mostly due to defects in the atomic lattice, e.g. caused by the surface roughness of the substrate or insufficient growth control. With increasing temperature starts electron-phonon scattering, which is dominated by acoustic-phonon scattering at low energies and optical- or zone-boundary-phonon scattering at high energies [125]. Purewal et al. showed for metallic nanotubes a maximum mean free path of 10 µm at 20K. Semiconducting tubes are more sensitive to disorder, thus have a much shorter mean free path. Depending on the dimension of the semiconducting CNT ranges the length of the mean free path between 0.2 µm to 1 µm at temperatures between 20K to 300K [125].

At room temperature CNT-FETs show a similar current-voltage characteristic as p-type MOSFETs: the drain-source current in the channel increases up to a saturation level with increasing negative gate voltage and the channel insulates when applying positive gate voltages. This indicates that the charge carrier transport is dominated by holes in SWCNT-FETs. However, for large positive gate voltages the nanotube starts conducting again. According to McEuen et al. it is a typical observation that the conduction in the n-type region is weak compared to the conduction in the p-type region due to the work function of the contacts. As the Fermi level of the contact material, for example Au or Pt, aligns with the HOMO of the nanotube, a barrier is formed, inhibiting the injection of electrons. N-type conduction could be enhanced by altering the work function with different processing techniques or using contact materials with different work functions [124]. In addition, the processing techniques and environmental conditions during the synthesis of CNT-FETs are crucial for capturing stable measurement results. High humidity while synthesis, for

example, enhances the adsorption of dipoles, such as H_2O or O_2, which shift the work function of the materials [124]. Thus, the characteristics of a transistor fabricated at high humidity may differ from a transistor fabricated in an arid environment. There are different theories about the origin of holes in semiconducting CNTs. Odom et al. assume the formation of a Schottky barrier at the contact-nanotube interface [21]. Their theory is questioned by Tans et al., as they argue that in case of a Schottky barrier the CNT-FETs would show a stronger temperature dependence. They support the hypothesis of contact induced holes, however, instead of a Schottky barrier, they suppose that the HOMO band edges of the nanotube align with the Fermi energy level of the metal contacts, enabling a tunneling contact. Further away from the electrodes the HOMO bends towards lower energies due to the lower work function Φ_{nt} = 4.5 eV of CNTs, compared to the work functions of typical contact materials, such as Au or Pt. Applying a positive or negative gate voltage either distorts the HOMO further, or flattens it towards the Fermi level of the contacts, resulting in a metal-like conduction [44]. Martel et al. avert from the hypothesis of holes being injected in the nanotube through the contacts. They suppose that the majority carriers are inherent to the CNTs. Considering a homogeneous hole distribution they calculate a hole density p of 1 hole per 250 carbons from:

$$p = \frac{Q}{eL_{nt}} \qquad (10)$$

with e being the elementary charge, Q being the total charge and L_{nt} the length of the nanotube. The total charge of the nanotube can be determined from the following equation:

$$Q = C_{nt}V_{th} \qquad (11)$$

where the nanotube capacitance C_{nt} is given by

$$\frac{C_{nt}}{L_{nt}} \approx \frac{2\pi\varepsilon\varepsilon_0}{\ln\left(\frac{2t}{r}\right)} \qquad (12)$$

sε and ε 0 are the dielectric constants of the device and of vacuum, t is the thickness and L_{nt} and r the length and radius of the nanotube. As the calculated hole density of 1 hole per 250 carbons is 40 times greater than that of graphene, Martel et al. conclude that the nanotube is either degenerated or was doped with holes during synthesis [37]. In contrast established the research team of Zhou [126] the theory of holes occurring in nanotubes due to electrostatic effects. They assume that charged species or particles are embedded in the surface of the substrate or bulk, which interact with the tube and alter the electronic properties. However, the electronic properties are not only defined by the charge carriers in the nanotube, but also by the channel-contact interface. The total resistance in a CNT-FET calculates from the tube resistance R_{nt} and the contact resistance R_c to

$$R_{tot} = R_{nt} + 2R_{ch} \tag{13}$$

where R_{nt} is dependent on the applied gate voltage. For large negative gate voltages the drain-source current saturates and the contact resistance Rch dominates the total resistance of the CNT-FETs. In this regime the corresponding contact resistance was determined to $R_{ch} = 1M\,\Omega$, which matches the contact resistance measured in metallic tube devices [39], [44].

5.1.2 Current- Voltage Characteristics

Although the transport mechanisms of organic and inorganic semiconductors differ, the current- voltage characteristics are described similarly. The I-V, or transfer curve, of an OTFT is divided in a linear regime and a saturation regime, whereat the threshold voltage Vth marks the transition between both regimes. In the linear regime the drain current I_D increases linearly with the applied gate voltage V_{GS}, while the relation of gate and drain voltage is given by $|V_{GS} - V_{th}| > |V_{DS}|$. At a device dependent magnitude of the gate voltage V_{GS}, the drain current starts to saturate. The overall resistance of the OTFT is then dominated by the resistance of the drain and source contacts. In the saturation regime the relation of gate and drain voltage is given by $0 < |V_{GS} - V_{th}| < |V_{DS}|$.

A fundamental parameter to describe the modulation of the charge carrier density in a semiconducting material as a function of the gate voltage is the transconductance g:

$$g_{lin} = \frac{\partial I_D}{\partial V_{GS}} = \mu C_d \frac{W_{ch}}{L_{ch}} V_{DS} \tag{14}$$

$$g_{sat} = \frac{\partial I_D}{\partial V_{GS}} = \mu C_d \frac{W_{ch}}{L_{ch}} (V_{GS} - V_{th}) \tag{15}$$

μ is the charge carrier mobility in the semiconductor, C_d is the gate dielectric capacitance and W_{ch} and L_{ch} are the width and length of the transistor channel. The gate voltage-dependent current output I_D in the linear and saturation regime is given by the following :

$$I_{D,lin} = \mu C_d \frac{W_{ch}}{L_{ch}} \left[(V_{GS} - V_{th})V_{DS} - \frac{V_{DS}^2}{2} \right] \tag{16}$$

$$I_{D,sat} = \frac{1}{2} \mu C_s \frac{W_{ch}}{L_{ch}} (V_{GS} - V_{th})^2 \tag{17}$$

Solving for the mobility we can extract the charge carrier mobility in the respective regimes.

$$\mu_{lin} = \frac{\partial I_D}{\partial V_{GS}} \frac{L_{ch}}{C_d W_{ch} V_{DS}} \tag{18}$$

$$\mu_{sat} = \frac{L_{ch}}{C_d W_{ch} V_{DS}} \left(\frac{\delta \sqrt{I_D}}{\delta V_{GS}}\right)^2 \tag{19}$$

A further feature to analyze the quality of a TFT is the subthreshold slope S. Below the threshold voltage increases the drain current exponentially with increasing gate voltage, when considering a semi-logarithmic plot of the transfer characteristic. The steepness of the slope indicates how fast the device can exhibit a transition from an off-current I_{off} and an on-current I_{on}. The subthreshold slope is defined as follows:

$$S = \frac{\partial V_{GS}}{\partial (\log_{10} I_D)} = \frac{kT}{q} \ln 10 \left(1 + \frac{q N_t}{C_d}\right) \tag{20}$$

with k, T and q being the Boltzmann's constant, the temperature and the electronic charge and N_t being the density of trap states at the interface of semiconductor and dielectric. Conventional MOSFETs with large gate oxide capacitance and few trap states often approach the maximum subthreshold slope of 60 mV=decade. Usually the quality of the semiconductor/dielectric interface in organic TFTs is lower and the subthreshold slope is larger [123], [127].

5.2 Material and Methods

5.2.1 Device Fabrication

We used 90% semiconducting CNTs diluted in H_2O with CMC as dispersant to prepare our solution. We used spray coating for a uniform distribution of the CNT solution on the substrate. Two-inch Si wafers with SiO_2 as gate dielectric served as substrate and gate contact.

CNTs used were purchased from Merck. The structure of the nanotubes is specified as zig-zag with a chirality of (6,5), while the average length and diameter are denoted to $L_{nt} = 1$ µm and $d_{nt} = 0:78$ nm. They were synthesized with the CoMoCAT TM catalytic CVD method. For dispersion we used the standard CMC parameters described in. The solution was further

diluted with H_2O in a ratio of 1:14 solution:H_2O, to achieve the desired CNT density. To fabricate the contact structure of CNT based TFTs thermal evaporation of Au was performed. To fabricate CNT-TFTs with Au contacts we decided for the bottom-gated coplanar structure, so that the CNT thin-film remains unharmed during processing. As a substrate we used two inch Si p++ wafers from MicroChemicals GmbH, which additionally functioned as gate contact. The wafers had a thickness of 270 µm with dry oxidized SiO_2 of 50 nm, which served as gate dielectric. The contact layout is schematically depicted in Figure 5-2.
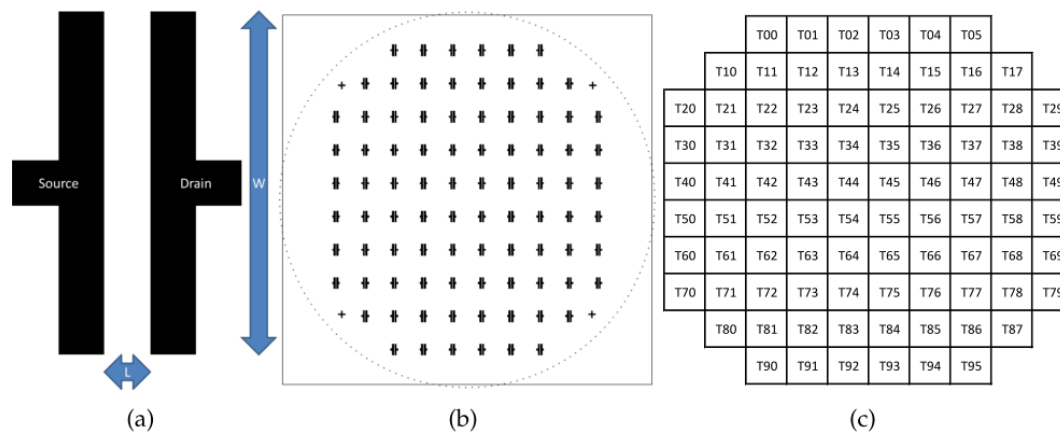

Figure 5-2 Schematic drawings of (a) source/drain electrode arrangements (b) wafer layout and (c) transistor nomination

Each wafer consists of 88 transistors with a channel length of 150 µm and a channel width of 1500 µm. The transistor nomination was spilt into columns and rows. The contact structure was patterned by negative photo-lithography with the ma N 1420 photoresist from micro resist technology GmbH. To achieve a uniform distribution, we deposited the photoresist on the wafer and spin-coated the sample at 50 rps for 30 s. To aid the evaporation of the residual solvent, we heated the wafer for 1 min at 100 °C.

Afterwards we masked the substrate with the TFT structure and exposed it for 15 s to UV-light. The exposed photoresist on the wafer polymerizes, while the masked part, with the TFT structure, remains un-polymerized and can be removed in the next step with the ma-D 533/S developer from micro resist technology GmbH. The contacts itself were thermally evaporated in a Univex 250 from Leybold GmbH. We deposited 5nm Cr as an adhesive layer followed by 50nm Au as contact material. In the next step we lifted the excess photoresist and gold residues off the substrate by means of an acetone bath followed by 2 min of sonication in acetone. To enable enhanced surface wetting of the wafer with the CNT solution, we modified the wafer surface at 0.3 bar O_2 plasma for 30 s at 150W. The plasma treatment increases the surface tension of the substrate by removing dangling bonds and

enables a decreased contact angle of solution droplets. Afterwards we soaked the wafer for 15 min in a solution of Isopropanol and 1 wt% APTES ((3-Aminopropyl)triethoxysilane) to promote the adhesion between the nanotubes and the SiO_2. For the deposition, we used the previously described spray deposition technique. For this purpose the CNT solution was atomized by a commercially available air atomizing spray valve from Nordson EFD. The valve is mounted on a four-axis automated motion platform above a hotplate and enabled a full cone spraying profile. We operated the nozzle in the wet spraying regime with an orifice opening of 0.7mm and a nozzle-substrate distance of 5 cm. The atomizing and material pressure were adjusted to 0.5 bar and 0.03 bar. In order to achieve a complete thin film the hotplate temperature was set to 62 °C, to enable the evaporation and merging of water droplets on the substrate. We covered the sensors with varying CNT film thickness (denoted as xL), to achieve different network densities. Note, that one layer comprise one spraying process in x-direction followed by one spraying process in y-direction. In order to remove the dispersant CMC from the nanotube network we placed the samples in an acid bath. We diluted one part of HNO_3 with four parts of DI water and soaked the wafers for at least 12 h. In the last step we removed our samples from the acid solution and dried them for 10 min at 100 °C on a hot plate, followed by a 10 min DI water bath and a subsequent drying step. Figure 5-3 schematically depicts the fabrication steps including the resulting wafer layout.
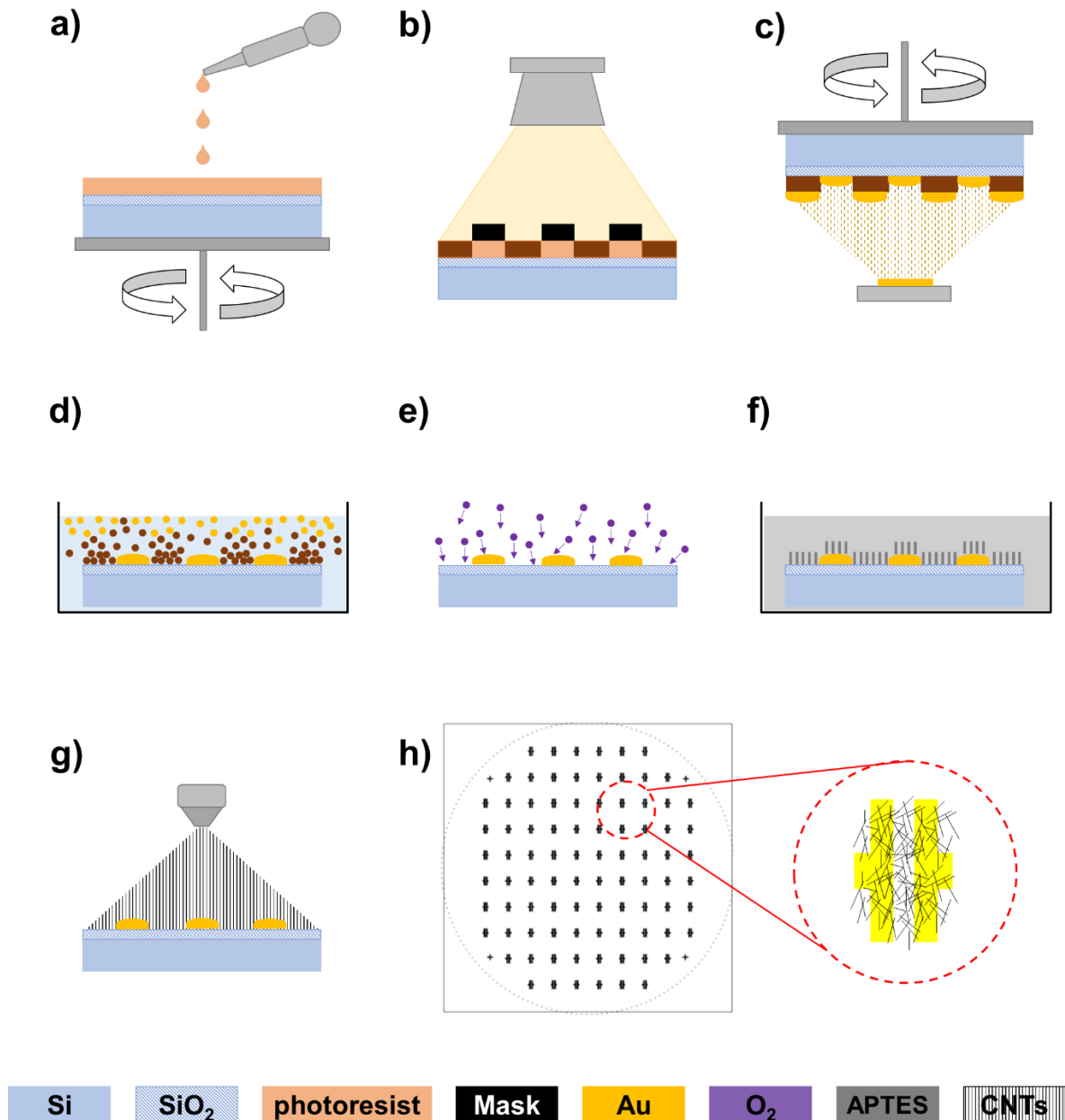
Figure 5-3 Schematic representation of the main fabrication steps we followed to fabricate gas sensors with thermally evaporated Au contacts. a) Spin-coating: application of negative photoresist on the wafer. b) Exposure process: exposed photoresist polymerizes and remains on wafer, while masked parts will be removed during development. c) Contact evaporation: deposition of evaporated Cr and Au particles on the substrate. Remaining photoresist will be removed during lift-off. d) Lift-Off: Remaining photoresist and gold particles, evaporated on top of the photoresist, are removed from the wafer in an acetone bath. e) Oxygen Plasma Treatment: surface cleaning with oxygen plasma to reduce surface tension. f) APTES treatment: soaking in APTES/Isopropanol solution to enhance CNT adhesion on the wafer. g) Spray-coating: application of a random CNT thin-film on the wafer. h) Final wafer layout consisting of 88 individual transistors. The magnification shows a schematic of a random CNT network on one of the sensors.

5.3 DC Characterization

For the electrical characterization of the transistors an automated measurement setup is used. The setup consists of a RK probe station, semiconductor analyzer (Keithley SCS 4200) and a LabView program. The interfacing between the various elements of the setup is done over the GPIB bus. The wafer is mounted onto a chuck which is connected to a pump that generates the vacuum for the chuck and controls the pneumatics for the z direction motion of the probe station. The chuck also serves as the gate contact and is connected to a pre amp leading into channel one of the SCS 4200. The source and drain contacts are identical and are contacted with the aid of micromanipulators with each channel respectively also being connected to their own pre amps. The LabView program controls both the data acquisition as well as the movement of the probe station. A typical measurement for a device consists of a transfer curve being measured from +10V to -10V V_{GS} in steps of 0.1V and -3V V_{DS} followed by five output curves in steps of 5V from 10V to -10V V_{GS} with a drain source sweep from 0V to -10V V_{DS} in steps of 0.1V. After a transistor is measured the stage is moved according to a given coordinate list and the measurements are repeated for the next transistor. The entire process is repeated until all transistors are measured.
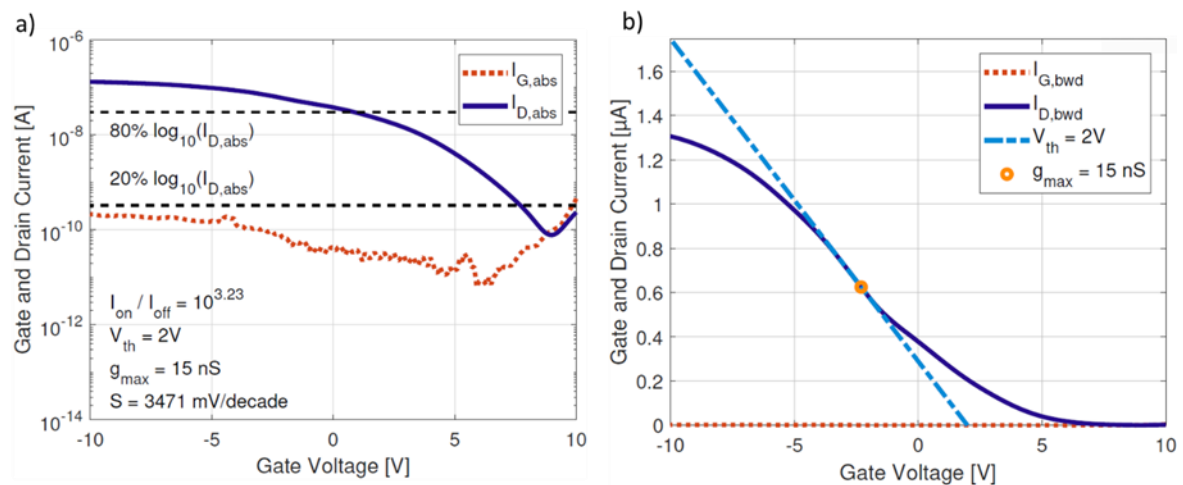

Figure 5-4 a) Half logarithmic representation of the transfer characteristic of a CNT-TFT in ambient conditions. The text box in the lower left corner displays different transistor characteristics, such as on-off ratio, threshold voltage, maximum transconductance and subthreshold slope. b) Linear representation of the transfer characteristic of a CNT-TFT in ambient conditions. The yellow circle indicates the point of maximum transconductance. The zero crossing of the tangent aligned at the point of maximum transconductance shows the threshold voltage.

Figure 5-4 exemplifies the transfer characteristic of a CNT-TFT recorded in ambient conditions. Drain gang gate currents are displayed in absolute values. From the recorded data, we determined different transistor characteristics, such as the on-off ratio I_{on}/I_{off}, the maximum transcsonductance g_{max}, the threshold voltage V_{th} and the subthreshold slope S,

which are displayed in lower left corner Figure 5-4. The on-off ratio was calculated by dividing the maximum drain current by the minimum drain current. We determined the maximum transconductance of the sensor by identifying the maximum gradient in the drain current data, which is depicted in Figure 5-4 as yellow circle. From the maximum transconductance we determined the threshold voltage graphically by aligning a tangent at the point of maximum transconductance. The zero crossing of the tangent indicates the threshold voltage. The tangent is depicted in Figure 5-4 as dashed, light blue line. Finally, we calculated the subthreshold slope between 20% and 80% of the maximum drain current in half-logarithmic representation.

5.3.1 Uniformity

A key characteristic for any process is the reproducibility and uniformity in device performance. As such we plotted all transfer characteristics of the 88 devices in Figure 5-5. As well as the transfer characteristics the I_{ON} was plotted in the form of a surface plot as to better visualize the individual transistors.
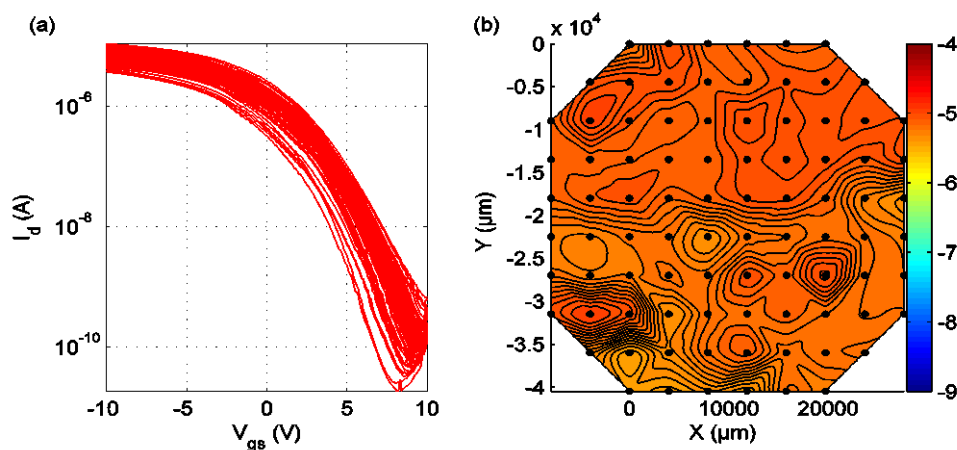

Figure 5-5 (a) Transfer characteristics of 88 4L CNT transistors on same wafer swept from +10 V to -10 V V_G at a V_{DS} of -3 V. (b) Contour plot displaying the spatial distribution of ON current of the 88 transistors on the 2"wafer. Each point represents an individual transistor. [Results published in [128]]

All transistors exhibit the normally-on characteristic with a threshold voltage mean of 4.43 V. The distribution of ON and OFF current has a width normalized mean of 4.77 μA/mm with and 0.12nA/mm, respectively. In the ON current regime, a clear homogeneity can be seen across all transistors indicative, as previously mentioned, of a homogeneous CNT distribution. In the OFF state, the variance in current derives from the non-negligible gate leakage which varies from transistor to transistor and, as such, affecting the distribution of OFF current. Distribution values for normalized transconductance and mobility are a mean

of 94 nS/mm and 2.12 cm2/Vs respectively. These value have been summarized in Figure 5-6 for better visualization. The histograms (blue) along with the overlapped fitted standard distribution fits (red) display a very narrow distribution in device performance, indicative of a reproducible process at the wafer level.
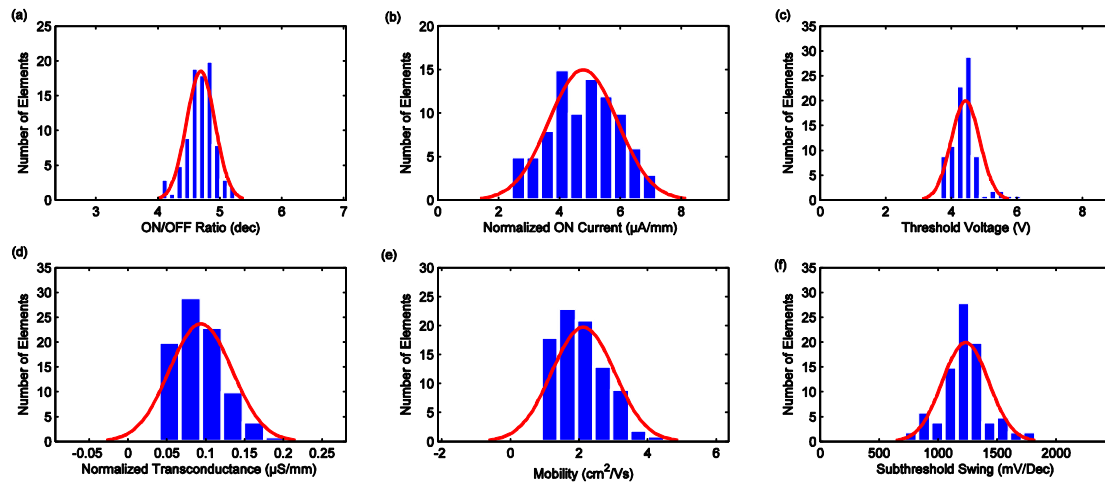

Figure 5-6 Histograms representing characteristic DC IV values for 88 4L CNT TFTs. (a-f) Width-normalized ON current (I_{ON}/W), ON/OFF ratio (I_{ON}/I_{OFF}), threshold voltage (V), width normalized transconductance (µS/mm), mobility (µFET) and subthreshold swing (S), respectively. [Results published in [128]]

5.3.2 CNT Density Dependency

As a starting point to a modular process, flexibility in the deposition of the CNT channel material is desired as the electrical performance of the transistor is closely related to film thickness, length and width of the channel. With increasing channel length the CNT film density needs to be adjusted correspondingly while a too steep increase in film can lead to the creation of too many metallic parasitic paths, not increasing film thickness can lead to a reduced ON current as not enough paths exist to bridge the gap. Depending on the purpose of the device certain characteristic are more decisive. An example being electrolyte gated bio sensors which have a gate operation from 0.6V to -0.6V [refxx]. In such a device, IDES structured electrodes are used to maximize current and while a good I_{on}/I_{off} ratio is desired, an I_{on} current with a magnitude of µA is more important. For such a device, the CNT layer would be deposited thicker than for a device for which the goal is to minimize I_{off} current and maximize I_{on}/I_{off} ratio.

In order to better understand the tuning possibilities it was important to investigate the CNT density deposited per layer. As such we performed AFM measurements of our CNT-TFTs. Figure 5-7 displays a 4 x 4 µm^2 area in the channel of a 4L transistor. The AFM image is then converted into a binary image and the surface coverage is extracted. Black pixels

represent the SiO₂ surface, while white pixels represent the CNTs and impurities. An analysis of the ratio of black and white pixels resulted in a surface coverage of 13.65%. Taking into account measurement artefacts from AFM and the impurities on the wafer, we expect an actual surface coverage below the extracted 13.65%.
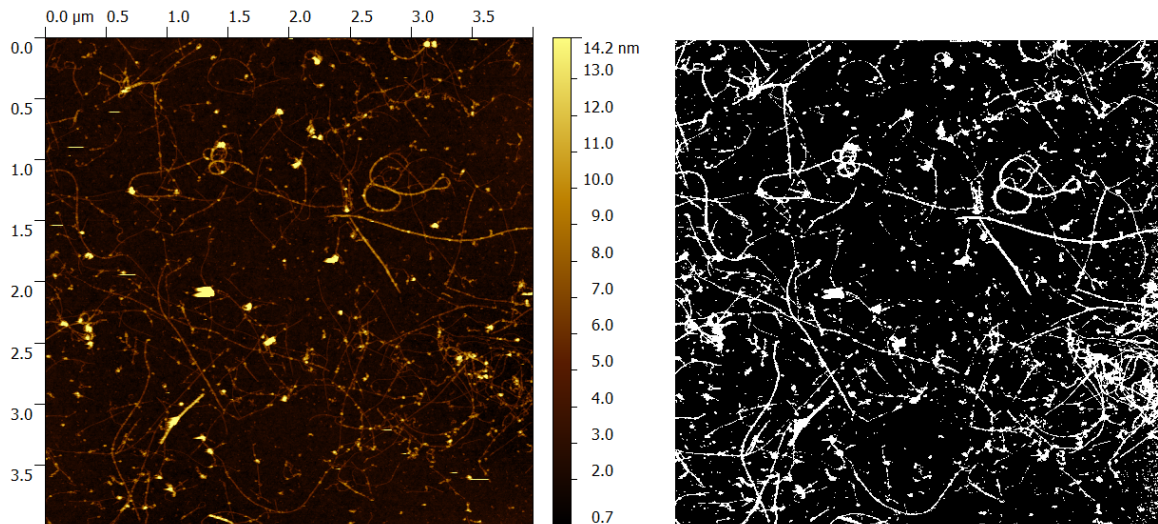

Figure 5-7 AFM image of a four layer CNT network deposited on SiO₂. Left: 4 μm x 4 μm image post software processing. Right: black and white conversion image to calculate surface coverage. [Results published in [128]]

The figure reveals a bundle-free distribution of CNTs on the substrate, as well as the lack of full surface coverage. Both are desired characteristics in semiconducting CNT thin-films. Due to the lack of a synthesis for pure semiconducting CNT, a random CNT network will also comprise a certain proportion of metallic tubes. If present in large bundles, metallic tubes dominate the charge carrier conduction, which results in the alteration of the device performance. In addition increased sensor coverage increases the probability of metallic CNT to form a conductive path between the electrodes. As a consequence, the sensor characteristic shifts from a gate voltage dependent switching to a resistive behavior. Therefore a network density below the percolation threshold of the metallic tubes is recommended [129].

From the extracted surface coverage of the 2L -6L transistors, a deposition of ca 5-6 CNT/ μm² was extracted with a linear relationship to the deposited number of layers. Please note that this is for very strongly diluted concentrations. From these results, we repeated the previous experiment as to investigate the transistor performance in relationship to layer number.
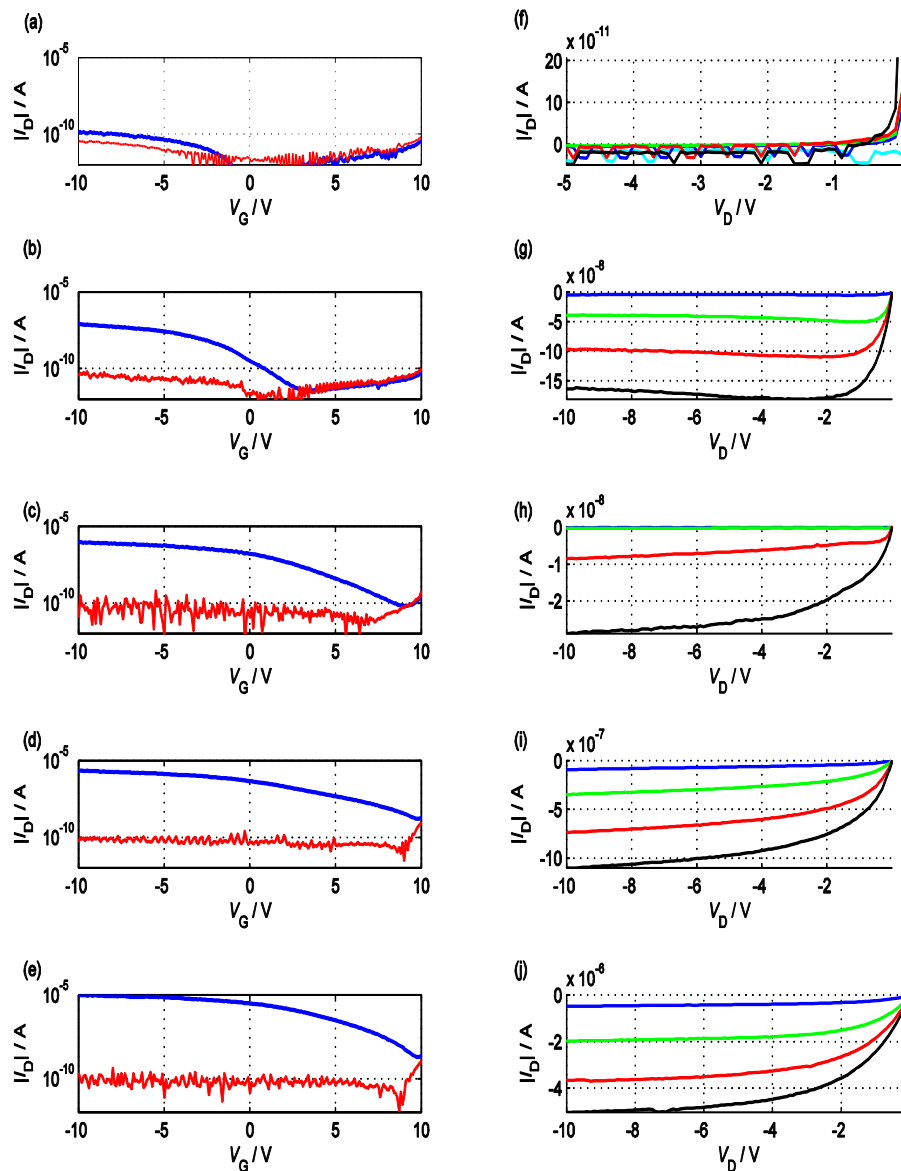
Figure 5-8 Plots (a-e) of transfer characteristic of a representative CNT transistor for each increasing layer (2L-6L) swept from +10V to -10V V_{GS} at a V_{DS} of -3V. Plots (f-j) displaying output characteristics of a representative device for each increasing layer (2-6) measured from 10V to -10V in 5V steps. The transistors were fabricated from CMC solution on Si wafers with full back gate.

Figure 5-8 shows typical transistor and output characteristics in ascending layer order. Transfer curves were measured from +10V to -10V V_{GS} in steps of 0.1V and -3V V_{DS} followed by five output curves in steps of 5V from 10V to -10V V_{GS} with a drain source sweep from 0V to -10V V_{DS} in steps of 0.1V. What is clearly visible at a thickness of two layers is that the CNT film is too thin and no real transistor is established. With increasing film thickness the transistor behavior is more visible. An increase of ON current is visible, with increasing film thickness, from 10^{-10} A to 10^{-7} A with the first increase in film thickness while OFF current remains constant. With a further increase in layer number the ON current

saturates and OFF current increases. This increase in performance can be explained by the previously mentioned analogy to the percolation theory. While at low layers the film thickness is close to percolation, too few paths bridge the electrodes with very low measured I_{DS}, an increase in film thickness results in a huge performance increase as we move beyond the percolation limit. As layer number further increases and as such film thickness, the benefit of increasing number of paths saturates as does increase in ON current. In addition to the saturation of benefit of increased path number, the numbers of metallic parasitic paths increase and as such an increase in OFF current is also visible. Detailed behavior of typical characteristics, for each layer, with increasing film thickness can be seen in Figure 5-9. Plotted in each of the graphs is the mean value for each layer with the error bars displaying the standard error from the mean. The potted data shows the safe aforementioned increase in ON current 10pA to 0.1μA with increasing layer number.
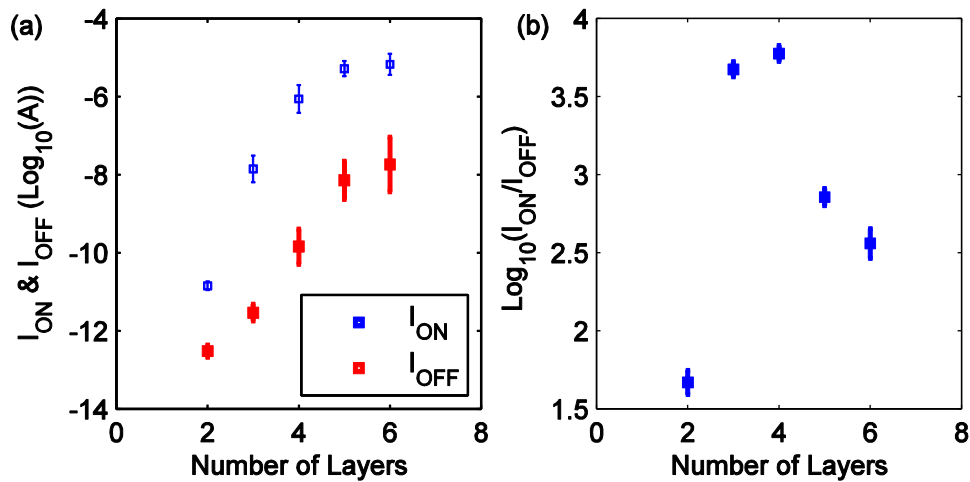

Figure 5-9 (a) Plot showing I_{ON}/I_{OFF} ratio with respect to deposited number of CNT layers. Error bars are displaying variance from the mean value. (b) Plot displaying I_{ON} with respect to deposited number of CNT layers. Error bars are displaying variance from the mean value. [Results published in [128]]

The effect of increasing layer number on ON current saturates and as such after four layers a decrease in ON/OFF ratio is observable. Similarly, what can be clearly seen is the increase in threshold voltage in the positive region from ca 0V at 3 layers to ca 5.5V at 5 layers. A possible explanation for this behavior is that with increasing film thickness the probability of metallic CNT is increased. At higher layer numbers, metallic paths are present so under floating gate bias a non-negligible current still flows and as such the concept of threshold voltage does not really apply in the strict sense of the word. What the voltage value indicates is how much voltage needs to be applied in order to fully shut off the transistor by limiting the charge carrier concentration in semiconducting paths. Such a reduction in charge carriers results in effectively higher barriers at metal/semiconductor interfaces essentially shut off such paths, which constitute the highest portion of the film. The analogy to silicon transistors

would be that the transistor behaves as an enhancement type transistor at low layer numbers while the behavior shifts to depletion mode at thicknesses above four layers. Transconductance increases with higher layer count as more paths are available and as such when semiconducting tubes shift from on to off a higher number of paths becomes available. Mobility is directly proportional to transconductance and behaves similarly with increasing layer thickness. Noteworthy however is that the capacitance model used for the capacitance calculation is a better fit at lower film densities as it assumes evenly spaced nanotubes while at higher film densities the capacitance model of a parallel plate becomes more appropriate. Subthreshold swing ranges from 1500 to 2300mv/dec at 2-5 layers while at 6 layer then a sharp increase to 3500mV/dec is measured. The transition from enhancement mode transistor to depletion mode allows for sensitivity towards gate bias. At even higher film thickness, even higher subthreshold swing values are to be expected as we move beyond the percolation threshold of purely metallic paths with charge transport dominated more and more by metallic paths. The reduction of film resistance by semiconducting tubes switching from OFF state to ON state becomes less prevalent.
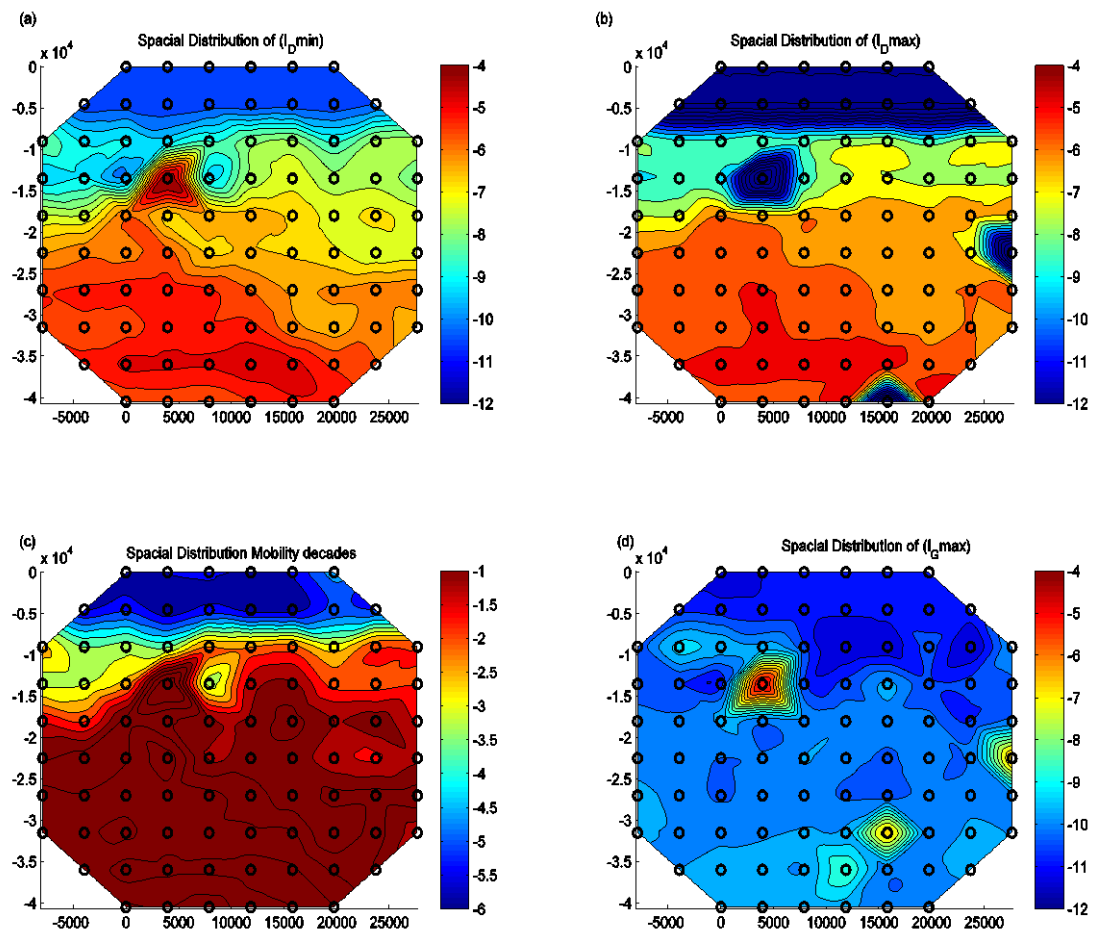

Figure 5-10 Surface plots visualizing a fabricated wafer of transistors from SDS solution with increasing layer number (2-6) and respective characteristics (a) Minimum current (I_{Dmin}), (b) maximum current (I_{Dmax}), (c) device mobility, (d) maximum gate current (I_{Gmax})

Regarding visualization Figure 5-10 provides spatial distribution surface plots of ON (I_{Dmax}) and OFF (I_{Dmin}) current as well as device mobility and maximum gate current (I_{Gmax}). A uniform device performance is visible across individual layers while a distinct change in characteristics is present with increasing layer thickness. The surface plot also show a very good device yield with only three defect transistors (T33, T59, and T94). The defective transistors are due to a local defective gate as can be clearly seen in the spatial distribution of maximum gate current.

5.3.3 Dispersant Dependency

In this section, a similar characterization is performed as in the anterior section. The alteration in fabrication is solely the dispersant used for the ink fabrication and the layer arrangement on the wafer (decreasing layer thickness rather than increasing thickness). The reason for the inverse layer order is for simplicity in production without an ulterior motive.

For the transfer and output curves displayed in Figure 5-11 representative devices were selected. The same as the CMC based transistors transfer curves were measured from +10V to -10V V_{GS} in steps of 0.1V and -3V V_{DS} followed by five output curves in steps of 5V from 10V to -10V V_{GS} with a drain source sweep from 0V to -10V V_{DS} in steps of 0.1V. Similarly to the previous results a clear increase of ON current is visible, with increasing film thickness, from 10^{-7} A to 10^{-5} A with the first increase in film thickness while OFF current remains constant. With a further increase in layer number the ON current saturates and while OFF current starts increasing. A more visible difference can be seen in the output characteristics where at low layer numbers at high gate voltage (-10V) rather than saturating a sharp decrease in current is visible. With increasing layers this effect is reduced in magnitude and at higher layer thicknesses (5-6) has completely disappeared.
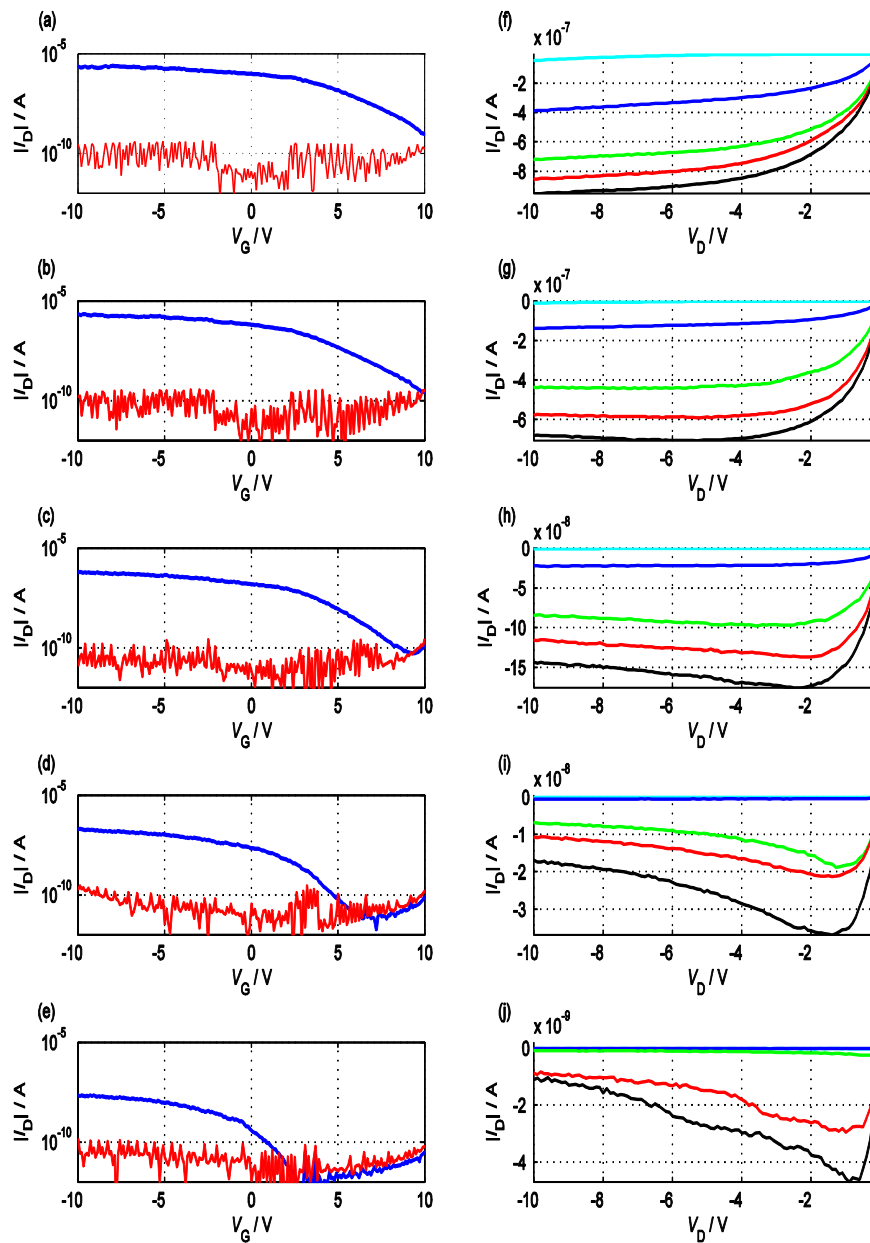
Figure 5-11 Plots (a-e) of transfer characteristic of a representative transistor for each decreasing layer (6-2) swept from +10V to -10V VGS at a VDS of -3V. Plots (f-j) displaying output characteristics of a representative device for each decreasing layer (6-2) measured from 10V to -10V in 5V steps. The transistors were fabricated from SDS solution on Si wafers with full back gate.

Regarding visualization Figure 5-11 provides spatial distribution surface plots of ON (I_{Dmax}) and OFF (I_{Dmin}) current as well as device mobility and maximum gate current (I_{Gmax}). A uniform device performance is visible across individual layers while a distinct change in characteristics is present with increasing layer thickness. The surface plot also shows a very good device yield. Overall, with the exception in output characteristic SDS and CMC based transistors show similar performances and as such SDS has become the dispersant of choice

as it is largely less process demanding as CMC and far less chemically invasive allowing for an easier integration into other systems
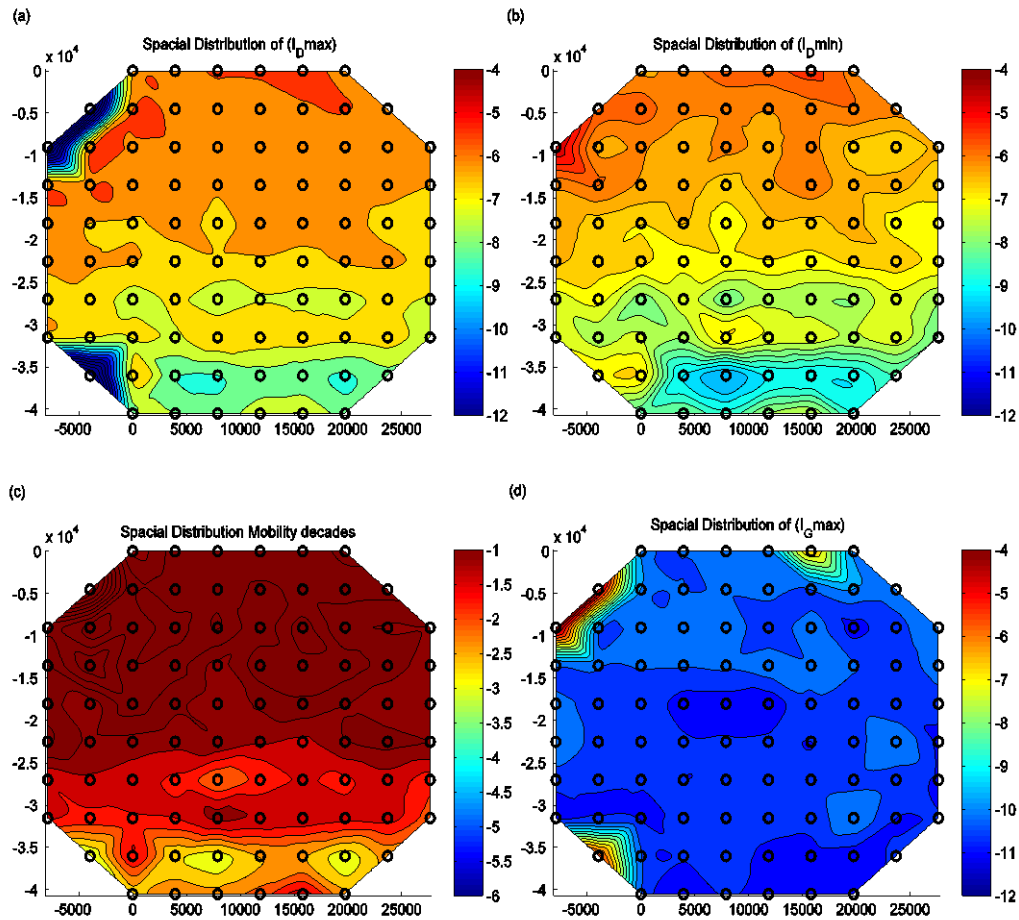

Figure 5-12 Surface plots visualizing a fabricated wafer of transistors from SDS solution with decreasing layer number (6-2) and respective characteristics (a) Minimum current (I_{Dmin}), (b) maximum current (I_{Dmax}), (c) device mobility, (d) maximum gate current ($I_{G}max$)

5.4 CMOS Integration with IGZO

In an attempt to fabricate devices able to perform basic logic operations, we choose the well-established complementary metal oxide semiconductor structure employed in silicon. Due to the p-type behavior displayed by the CNTs in ambient conditions, rather than attempting to modify the CNTs by means of functionalization [130]–[133], the pairing with already existing n-type TFTs is chosen. One such material system is the inorganic indium gallium zinc oxide. This material system has been thoroughly investigated and displays astonishing transistor behavior [134]–[137]. Due to the non invasive processes steps, the CNT deposition process is added to an existing process, developed at the ETH Zürich for the deposition of contacts, insulator and IGZO. [138]–[140]

The fabricated circuits are manufactured on a flexible foil as to also test the feasibility of the resulting system as a flexible device. The target structure is a coplanar back gated CMOS structure. The substrate used is a polyimide foil commonly known as Kapton. The first step is the deposition of a 50 nm SiN_x adhesion layer by use of a plasma-enhanced chemical vapor deposition. This is a uniform coating covering the entire substrate. For the gate contacts, 30 nm Cr electrodes are evaporated by e-beam evaporation and patterned by a subsequent UV photolithography masking and wet etching. As an insulating gate dielectric layer 50 nm Al_2O_3 (dielectric constant ca. 9.5) was grown by atomic layer deposition at 150°C. The n-type IGZO layer is deposited radio frequency magnetron sputtering and results in a 15 nm layer. This process is performed at room temperature and a ceramic IGZO target is used. At this time, IGZO and opening in the oxide for the gate contacts are patterned by means of UV lithography followed by a subsequent wet etch. Source and drain contacts, consisting of Ti/Au, 10 and 50nm respectively, as well as interconnect lines are e-beam evaporated and patterned by lithographic lift-off. As a passivation for the IGZO, a 1.8µm layer of AZ1518 photoresist is spin coated and photo lithographically patterned. For the p-type CNT a, as purchased, 99.9% of semiconducting CNT solution with a wt% of 0.001 dispersed in DI H_2O with the aid of a proprietary dispersant based on SDS, is used. The solution is sprayed through a shadow mask at 50 °C. The dispersant is removed using a subsequent DI H_2O bath. A schematic of the resulting sa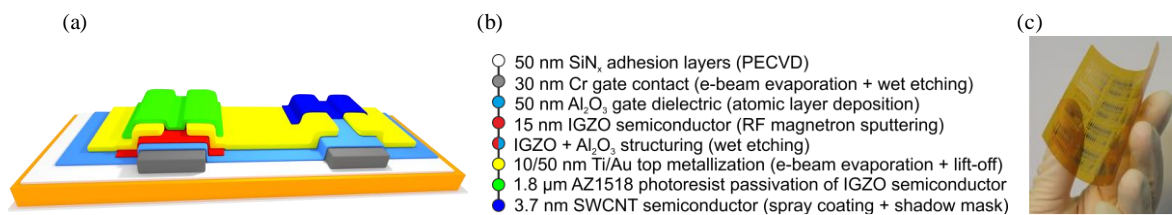mple with the accompanying processes can be observed in Figure 5-13 Schematic cross-section (a) and fabrication process flow (b) of flexible complementary circuits based on n-type IGZO and p-type SWCNT TFTs on a free-standing 50 µm-thick polyimide foil. The fabrication process was optimized concerning low temperature fabrication (<150 °C), thickness of brittle materials, and adhesion between the different device layers aiming at good electrical performance and mechanical bendability. A photograph of the entirely processed flexible substrate is shown in (c).Figure 5-13 as well as a photograph of the entire substrate.

(a)   (b)   (c)

○ 50 nm SiN_x adhesion layers (PECVD)
● 30 nm Cr gate contact (e-beam evaporation + wet etching)
● 50 nm Al_2O_3 gate dielectric (atomic layer deposition)
● 15 nm IGZO semiconductor (RF magnetron sputtering)
● IGZO + Al_2O_3 structuring (wet etching)
● 10/50 nm Ti/Au top metallization (e-beam evaporation + lift-off)
● 1.8 µm AZ1518 photoresist passivation of IGZO semiconductor
● 3.7 nm SWCNT semiconductor (spray coating + shadow mask)

Figure 5-13 Schematic cross-section (a) and fabrication process flow (b) of flexible complementary circuits based on n-type IGZO and p-type SWCNT TFTs on a free-standing 50 µm-thick polyimide foil. The fabrication process was optimized concerning low temperature fabrication (<150 °C), thickness of brittle materials, and adhesion between the different device layers aiming at good electrical performance and mechanical bendability. A photograph of the entirely processed flexible substrate is shown in (c). [Results published in [141]]

For an initial surface topological characterization of the active layers, AFM images were taken of the resulting layers post deposition. The results are depicted in Figure 5-14 with (a) being the IGZO film and (b) the CNT film. Visible for the IGZO film is a homogeneous distribution of material without stark grain boundaries. The CNT film exhibits a good distribution with well dispersed and separated tubes visible, however clear bundles can also be observed.
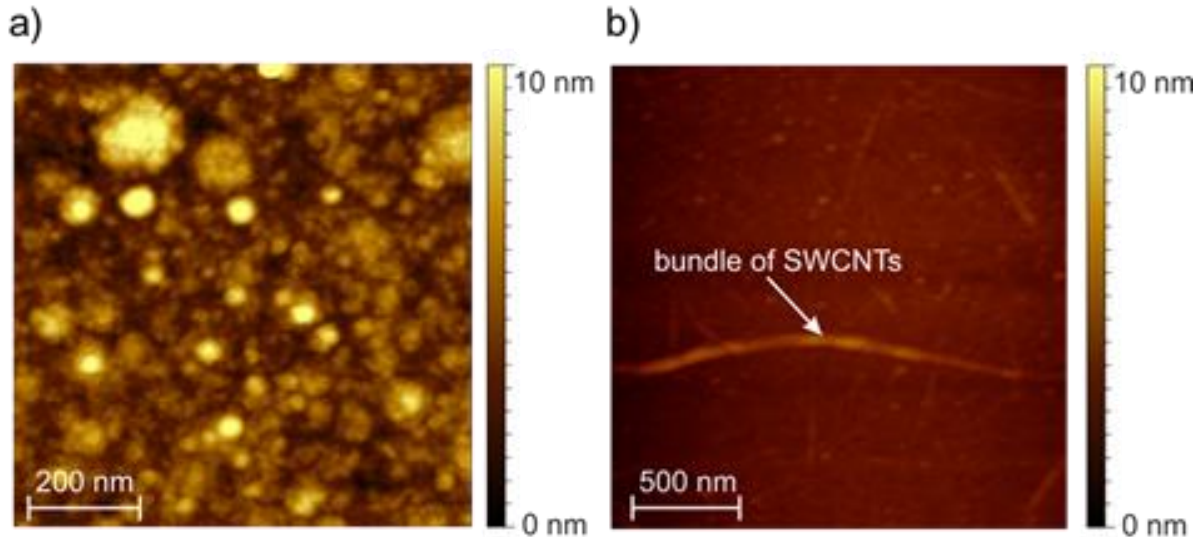

Figure 5-14 AFM images displaying topography of the semiconducting layers in the CMOS structure (a) IGZO and (b) CNT. The underlying material system consists of polyimide, SiN_x and Al_2O_3

The electrical characterization was performed using an Agilent technologies B1500A parameter analyzer. For the initial characterization both transistors were characterized in ambient air both in an output configuration as well as transfer. Selected were identical channel lengths at 25 µm while the current measurements were width normalized. The applied voltages in the transfer configuration were V_{GS} -2V to 10V and 2V to -10V for the IGZO and CNT film respectively. Both transistors were biased at $|V_{DS}| = 0.5V$ and 10V. For the output characteristics the transistors were measured past the threshold voltage. In the IGZO case from $V_{GS} = 5V$ to 10V in 1V steps while sweeping V_{DS} from 0V to 10V. For the CNT transistor, V_{GS} was stepped from 0V to -10V in 2V steps with the V_{DS} being swept from 0V to -10V. Figure 5-15 displays the measured transistor characteristics with (a-b) representing the IGZO transistor while (c-d) the CNT. From the measured data, a saturation field-effect mobility μ_{FEn} of 26.6 $cm^2V^{-1}s^{-1}$ and μ_{FEp} of 0.1 $cm^2V^{-1}s^{-1}$ were calculated for the IGZO and CNT transistor respectively. Threshold voltages were $V_{THn} = 5.4V$ and $V_{THp} = -1.4V$ for IGZO and CNT respectively. Both transistors showed negligible gate leakage around 10nA that can also be seen in Figure 5-15. In terms of I_{ON}/I_{OFF} ratios, 3x 10^8 and 70 were extracted for IGZO and CNT transistors respectively. The low I_{ON}/I_{OFF} ratio for the CNT transistor can be mainly attributed to the poor debundeling that is also visible in Figure

5-14. It has been shown in literature that electrical transport, in bundled CNTs, is dominated by metallic tubes, if present [82]. Furthermore the CNT layer thickness was engineered in such a way that the I_{DS} matches the IGZO transistor as the intention is to combine the two technologies in a CMOS architecture. In order to avoid a possible bottleneck in the CNT transistor a tradeoff was made with regard to the I_{ON}/I_{OFF} ratio. As such, this aspect needs to be further optimized. The final characteristic examined was the hysteresis behavior. The IGZO transistor exhibits a negligible clockwise hysteresis of <25 mV while the CNT transistor a clockwise hysteresis of <1.3V both measured at $|V_{DS}| = 0.5V$. The generated hysteresis stems from the air measurement environment as further enunciated in 5.1. At the time of the experiments, this behavior yielded a reduced hysteresis in comparison to previous works that employed CNTs in flexible CMOS circuits [140]. With an encapsulation targeted at specifically reducing humidity at the semiconductor oxide interface, without interfering with transistor performance, a further reduction is viable.
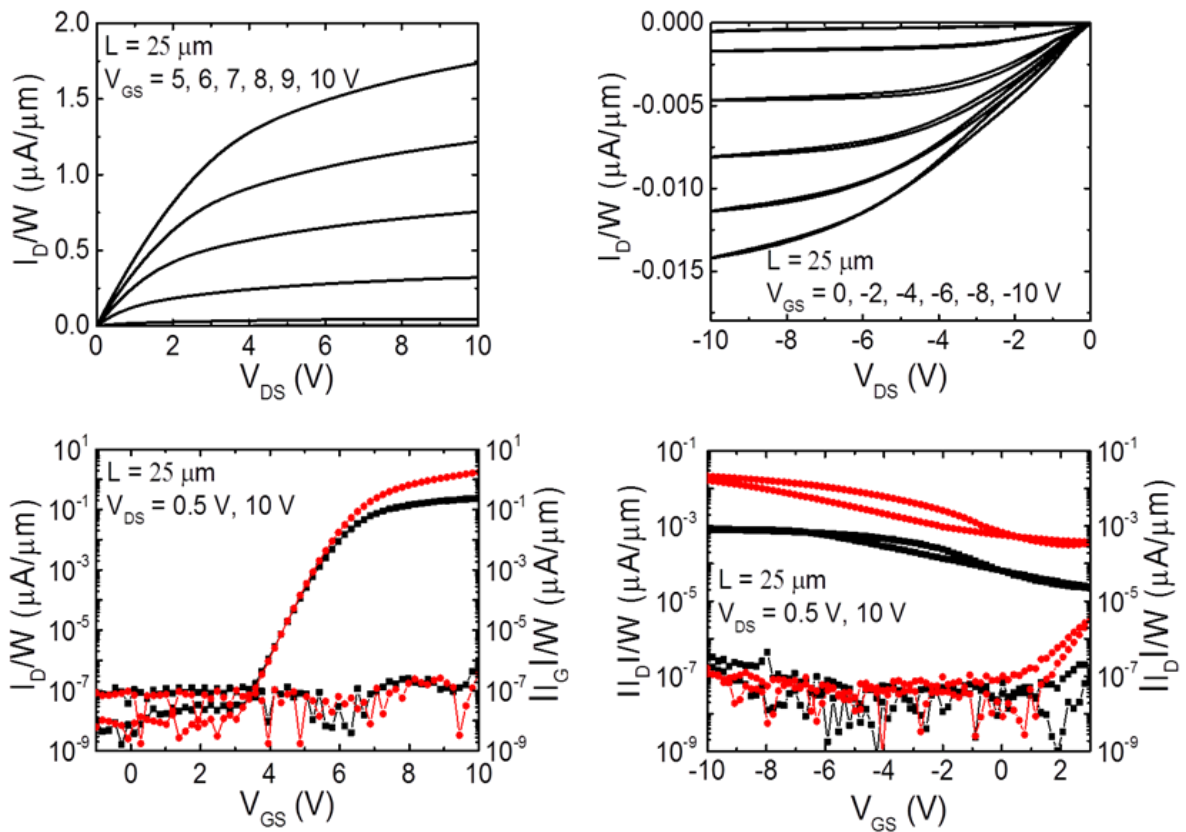

Figure 5-15 Width-normalized output (a) and transfer (b) characteristic of flexible n-type IGZO TFT measured in air. TFT performance parameters are: $\mu_{FEn} = 26.6$ cm^{2}V^{-1}s^{-1}, $V_{TH} = 5.4$ V, and $I_{ON}/I_{OFF} = 3 \times 10^8$. Width-normalized output (c) and transfer (d) characteristic of flexible p-type SWCNT TFT measured in air. TFT performance parameters are: $\mu_{FEp} = 0.1$ cm^{2}V^{-1}s^{-1}, $V_{TH} = -1.4$ V, and $I_{ON}/I_{OFF}=70$. [Results published in [141]]

5.4.1 Logic Gates

Fig. 5 shows the circuit diagram (a) and schematic (b) of the flexible complementary NOT gate fabricated on a free-standing polyimide foil. The complementary inverter was realized by complementing an n-type IGZO TFT (W/L = 500 µm/25 µm) with a p-type CNT TFT (W/L = 10000 µm/25 µm), as shown in Fig 5 (b). The flexible CNT/IGZO NOT gate was electrically characterized in ambient air using the following measurement conditions: a V_{DD} = 10 V, an input voltage swing V_{IN} from 0 to 10 V, and an input frequency f_{IN} = 500 Hz. All signals were monitored using a multichannel oscilloscope. The resulting digital input and output signal of the flexible NOT gate are displayed in Fig. 6. At 500 Hz input frequency, the NOT gate yields a rise time t_r of 140 µs, a fall time t_f of 11 ns, a propagation delay t_p of 9 ns, and an output swing V_L of 9.4 V. For input frequencies above 1 kHz, the output signal gets distorted, due to the large parasitic capacitances of the interdigitated p-type SWCNT TFT channels.
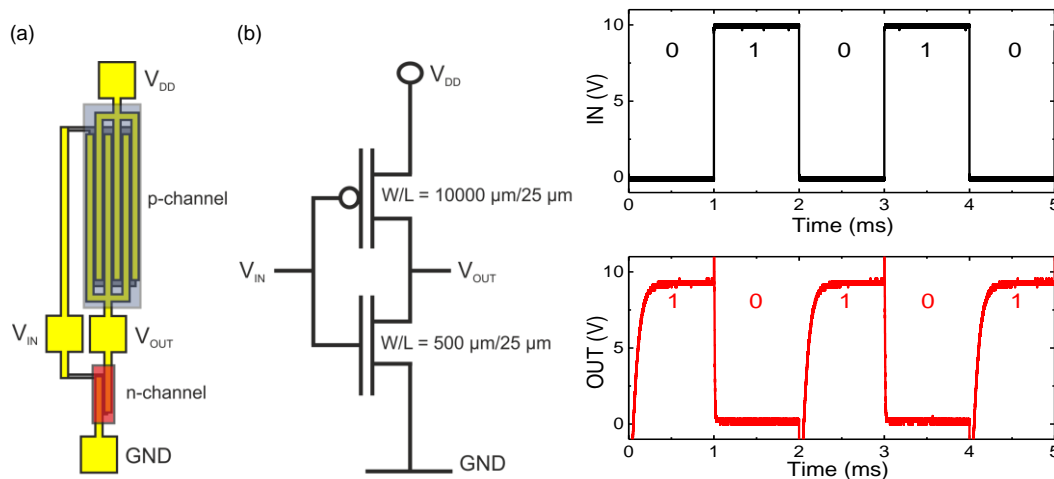

Figure 5-16 Circuit schematic (a) and diagram (b) of flexible complementary NOT gate. All TFTs have a channel length L = 25 µm. The p-type TFT presents an interdigitated channel. c) Input and output signals of flexible complementary NOT gate based on p-type SWCNT and n-type IGZO TFTs measured in air at V_{DD} = 10 V, V_{IN} = 0-10 V, and f_{IN} = 500 Hz. [Results published in [141]]

To demonstrate the feasibility of our complementary circuit technology for larger logic gates, also flexible complementary two-input NAND gates were realized. Fig. 7 displays the circuit diagram (a) and schematic (b) of the flexible NAND gate realized connecting two n-type IGZO TFTs (W/L = 500 µm/25 µm) and two p-type SWCNT TFTs (W/L = 10000 µm/25 µm). Also in this case, the flexible SWCNT/IGZO NAND gate was electrically characterized in ambient air using a V_{DD} of 10 V, a voltage swing of the two input signals $V_{IN,1}$ and $V_{IN,2}$ from 0 to 10 V, and an f_{IN} = 500 Hz. The resulting input and output signals monitored through an oscilloscope are given in Fig. 8. As shown in Fig. 8 (b), the

SWCNT/IGZO NAND gate is able to fully reproduce the desired two-input logic function with an output swing V_L of 8.5 V. Like the NOT gate, also the NAND gate yields similar rise, fall and propagation times, as well as a full operation up to an input frequency of 1 kHz.
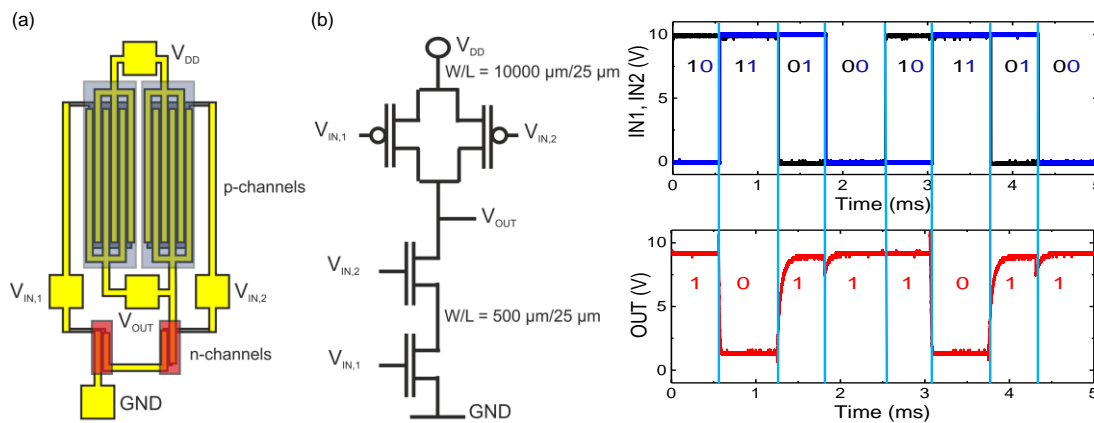

Figure 5-17 Circuit schematic (a) and diagram (b) of flexible complementary NAND gate. All TFTs have L = 25 µm. P-type TFTs present an interdigitated channel c) Input and output signals of flexible complementary NAND gate based on p-type SWCNT and n-type IGZO TFTs measured in air at V_{DD} = 10 V, $V_{IN},1 = V_{IN},2 = 0$-10 V, and f_{IN} = 500 Hz.

5.4.2 Flexibility Stability

A complete set of performance parameters of flexible circuits cannot be limited to the electrical characteristics, but needs to deal also with the mechanical properties. In an effort to test the mechanical characteristics of our complementary circuits, we attached a flexible CNT/IGZO NOT gate to double-side adhesive tape and wound it around a metallic rod of 1 cm radius. Figure 5-18 displays the input and output signals of the NOT gate measured while flat and bent to 1 cm tensile radius, which corresponds to a tensile strain ε of ≈ 0.3 %. As shown in Figure 5-18, the NOT gate stays fully operational when strained to 0.3 % and yields only small changes in the performance parameters (V_L decreases by 7.4%). Furthermore, the circuits are functional after re-flattening, while bending to radii below 4 mm induces cracks in the TFT films that permanently harm the device operation.
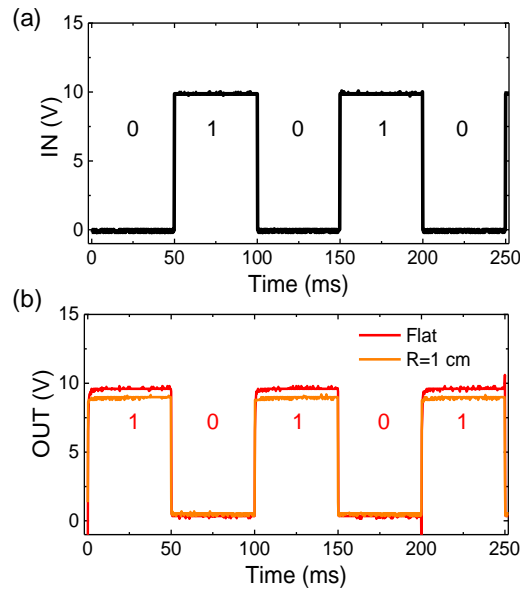
Figure 5-18 Width-normalized output (a) and transfer (b) characteristic of flexible n-type IGZO TFT measured in air. TFT performance parameters are: $\mu_{FE,n}$ = 26.6 cm^2/Vs, V_{TH} = 5.4 V, and I_{ON}/I_{OFF} = 3x10^8. Width-normalized output (c) and transfer (d) characteristic of flexible p-type SWCNT TFT measured in air. TFT performance parameters are: μFE,p = 0.1 cm^2/Vs, V_{TH} = -1.4 V, and I_{ON}/I_{OFF} = 70.

5.4.3 CS-Amplifier

The promising performance of our logic gates prompted us to explore the potential of this technology for flexible analog circuits, such as common-source amplifiers. Figure 5-19 shows the circuit schematic (a) and diagram (b) of the complementary amplifier constituted by an n-type IGZO TFT (W/L = 8400 µm/10 µm) and a p-type SWCNT TFT (W/L = 7200 µm/10 µm).
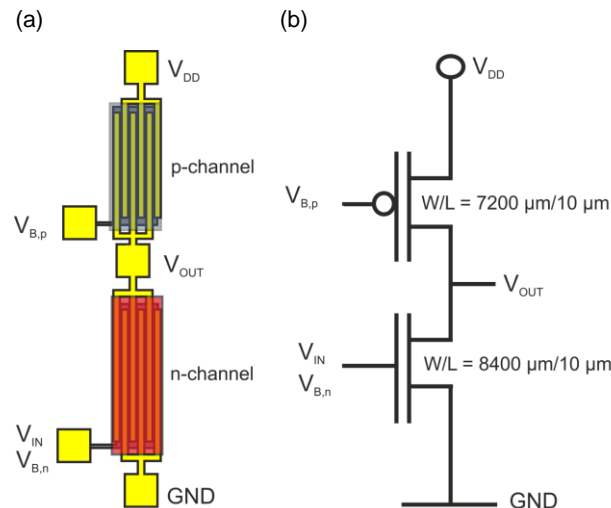
Figure 5-19 Circuit schematic (a) and diagram (b) of flexible CS amplifier (all TFTs have L = 10 µm and an interdigitated channel). The sinusoidal signal is applied at the gate of the n-type TFT, whereas n- and p-type devices are supplied with VB,n and VB,p, respectively. Circuit schematic (a) and diagram (b) of flexible complementary NAND gate. All TFTs have L = 25 µm. P-type TFTs present an interdigitated channel

The AC analysis of the amplifier was performed by applying a V_{DD} of 10 V and a sinusoidal signal with peak-to-peak amplitude V_{IN} of 100 mV and offset $V_{B,n}$ to the gate of the n-type IGZO TFT. At the same time, the p-type SWCNT TFT was supplied with a bias voltage $V_{B,p}$ in order to act as a current source load. The resulting output signal was monitored with the aid of an oscilloscope with a total resistive and capacitive load of 1 MΩ and 2 pF, connected to the amplifier output refxx. To find the optimal operating point of the CS amplifier, a sweeping of $V_{B,p}$ and $V_{B,p}$ was performed at an input frequency of 100 Hz and the corresponding voltage gain (G) was measured . The graph in Figure 5-20 shows how the amplifier gain can be modulated through $V_{B,n}$ and $V_{B,n}$ in order to reach a peak value G = 28.7 dB (at $V_{B,n}$ of 7 V and $V_{B,p}$ of 8 V). To the best of our knowledge, this is the highest gain ever reported for flexible complementary amplifiers [141], [142]. Thanks to the p-type SWCNT TFT acting as current source load, this gain exceeds also the best value shown for flexible unipolar single-stage CS amplifiers. The Bode plot of the circuit operated at different $V_{B,n}$ and $V_{B,p}$ measured in ambient air is shown Figure 5-20. At $V_{B,n}$ = 7 V and $V_{B,p}$ = 8 V, the CS amplifier yields a cutoff frequency f_c of 2.2 kHz and a gain bandwidth product GBWP of 60 kHz. Different values of $V_{B,p}$ result in lower gains but in the same GBWP of ≈ 60 kHz.
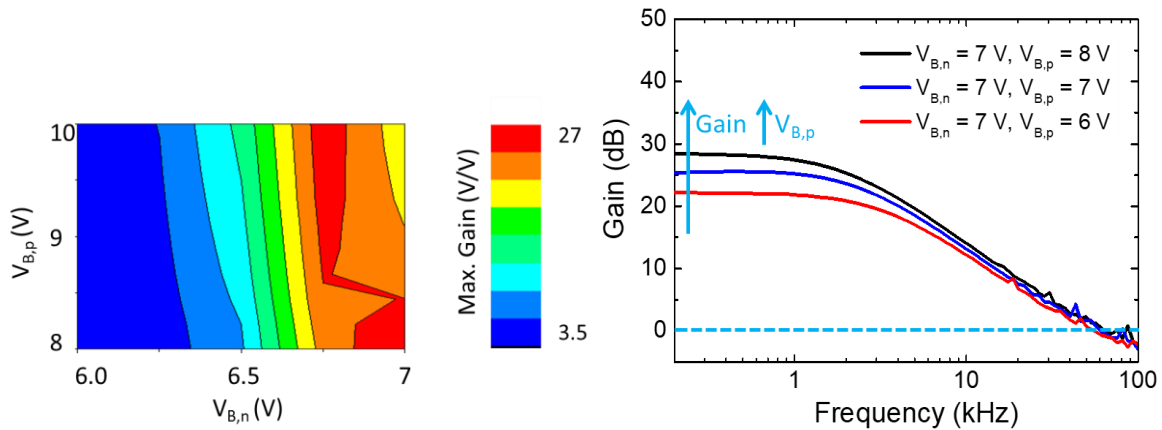
Figure 5-20 a) Maximum gain G of flexible complementary CS amplifier as a function of the bias voltages VB,n and VB,p. At VB,n = 7 V and VB,p = 8 V (fIN = 100 Hz), an optimal value G = 27.2 V/V (28.7 dB) was measured. b) Bode plot of flexible CS amplifier measured in air at different VB,p. At VB,n = 7 V and VB,p = 8 V, G = 28.7 dB, fc = 2.2 kHz, and GBWP = 60 kHz. [Results published in [141]]

5.5 Summary

In this chapter, we presented our concept for carbon nanotube thin-film transistors (TFTs) based on random networks. Initially a short overview of general organic TFTs was given as well as the basic charge transport mechanism. Following we showed the specifics pertaining to CNT TFTs. We introduced I-V characteristics for OTFTs and key characteristics defining figure of merits such as field effect mobility, transconductance and subthreshold swing. Following the theoretical aspects, we introduced our fabrication protocol for CNT TFTs. We investigated the homogeneity and reproducibility of our process. Showing both great yields as well as a thin deviation on the wafer scale. For a better understanding, we investigated the device performance dependency on CNT density with the corresponding figure of merits in the process gaining a better understanding of the device performance correlation to increasing CNT densities. In correspondence with the developed SDS ink in a previous chapter, we repeated the investigation to display its efficiency as an alternative to the CMC process that requires an acid treatment post deposition. Although not reaching the performance of CMC based process, the SDS process provides an alternative for more sensitive substrates. Due to the modularity of our process, it allowed us to integrate it into an existing process and realizes a flexible CMOS configuration with the CNT TFT as the p-type and indium gallium zinc oxide (IGZO) as the n-type. With this configuration we fabricated common logic gates such as not and nand. We investigated the system in a flexible configuration showing great mechanical stability and reliability. In contrast to previous works, we managed to reduce both the hysteresis behavior of CNT TFT as well as reliability.

Finally we fabricated a flexible common source amplifier with, at the time the highest gain for flexible complementary amplifiers.

Chapter 6

CNT Thin-Film: Gas Sensors

Due to the unique properties of CNTs, a wide applicability, as active and passive material in a wide range of applications, can be observed. One such application is their use in gas sensing applications. The following chapter will investigate the use of CNTs as an active layer in a gas sensor configuration. Initially the general working device principle will be presented, followed by the manufacturing and testing of the fabricated devices. In subsequent sub chapters resistive sensors, sensors based on TFTs and finally a sensor fabricated by means of a new quick prototyping based on robot assisted written electronics, will be presented.

6.1 CNT Gas Sensor Overview

Deriving from, the high aspect ratio of CNTs, is their high surface area to volume ratio. This key characteristic renders them geometrically as an ideal sensor material as due to maximization of analytes binding sites present. To better understand the suitability as a sensing material, a description of the interaction mechanism between analyte and CNT is needed. Due to the strong chemical bonds in the honeycomb structure of CNTs, the chemisorption of CNTs is minimal as such most molecules that adhere to the CNT are by physisorption. This is a weaker binding mechanism that relies on van der Waal forces. Bound molecules, based on their structure, act either as charge donor or acceptors. Looking at possible binding sites, there are four distinct options; surface (S), pore (P), groove (G) and interstitial (I). Figure 6-1 depicts the potential binding sites in relation to CNTs. Depending on the binding site, binding energy E_a and charge transfer Q_t vary greatly. As such adhesion on the surface is less favorable as binding energy is reduced in comparison to the other binding sites. Zhao et al. [51] performed a detailed analysis on the binding energies and

charge transfer for varying analytes with weak binding energies ($E_a \leq 0.2$ eV) for NH_3, CO_2 and H_2O with a positive charge transfer. While gasses such as NO_2 and O_2 exhibited a stronger binding energy (0.5 eV $\leq E_a \leq 0.8$ eV) with a negative charge transfer due to unpaired electrons.
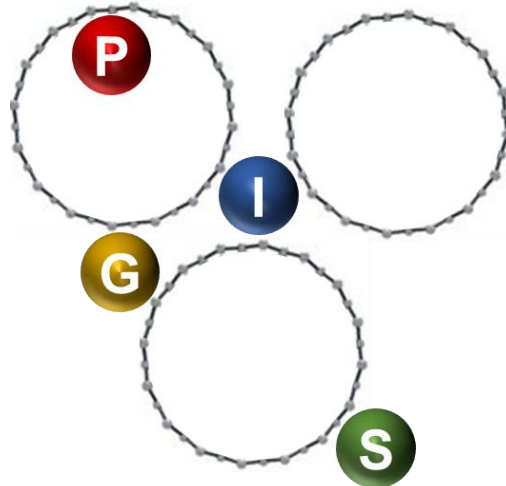

Figure 6-1 Schematic displaying the four possible binding site of a molecule in relation to CNTs. surface (S), pore (P), groove (G) and interstitial (I)

Kong et al. [143] have further expanded on this by separating the CNT-molecule interaction into two categories: intratube modulation and intertube modulation. Intratube modulation is the change in the properties of a single nanotube by direct charge transfer form a donor or acceptor molecule. The additional charge either depletes, or enhances the hole density in the nanotube, by shifting the Fermi level of the CNT further away from the HOMO, or closer to it. The direct transfer of charge manifests as significant increase of conductivity for acceptor adhesion and conductivity drop, if donor molecules adhere to the nanotube. In this case the molecule either interacts directly with the honeycomb carbon lattice or adheres to the nanotube due to defects or foreign particles, such as O_2 in the lattice [144]. Intertube modulation is the change in the conductive path between CNTs. One such proposed mechanism is the forming of hopping junctions between the molecule and the nanotube. This theory applies especially for nanotube networks, where the molecule is adsorbed at the CNT-CNT junction. The charge transport across the nanotube network is altered, as such the charge flow is impeded by an additional energy barrier induced by the molecule [145]. These suggested mechanism are summarized in Figure 6-2.
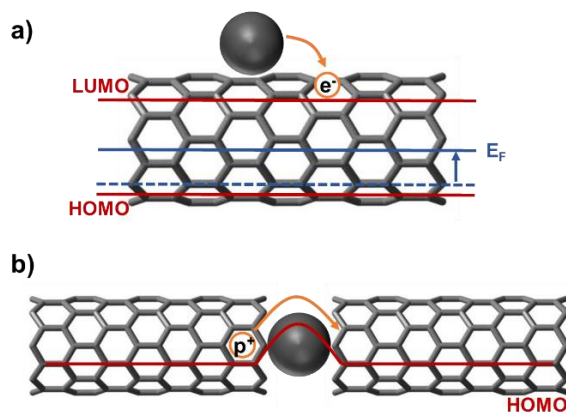
Figure 6-2 Schematic representation of the two types of CNT-molecule interaction: a) intra-tube modulation of a donor molecule which adheres to the nanotube. The donation of an electron results in a shift of the Fermi level of the nanotube towards the LUMO and b) inter-tube modulation, where a molecule is adsorbed between two adjacent CNTs. The charge carrier flow in the HOMO is altered due to an additional energy barrier caused by the molecule.

Consulting further literature, Cui et al. [52] and Yamada et al. [146] defend a hypothesis that molecule adsorption at the CNT-contact interface is the main factor responsible for the sensing mechanism in CNTs. The key aspect of this is that acceptor and donor molecules act as dipole at the contact CNT interface and generate an electrostatic potential. If the negative pole faces the CNT and the positive pole faces the contact, the work function and the HOMO are increased. As a result, the hole injection barrier S_p is diminished and the p-type conductance of the nanotubes is enhanced. Reversing the dipole orientation reduces the contact work function and thus the electron injection barrier, which consequently diminishes the p-type conductance of the nanotube. This hypothesis of gas effecting the contact work function is supported by the findings that CNT-TFTs alter their electrical behavior from p-type to n-type conduction in vacuum [56].

Figure 6-3 displays schematically the aforementioned effect. Visualized are the adsorption of both an electron donor, NH_3 (b), and an electron acceptor, O_2 (a). The figure shows the formation of an interface dipole between the metal electrode and the CNTs, which alters the work function magnitude Φ by a potential ΔU. Note that the electron affinity ϕ_{e^-} and the distance between the Fermi level E_F and LUMO ΔE remain the same independent of the type of molecule adhesion.
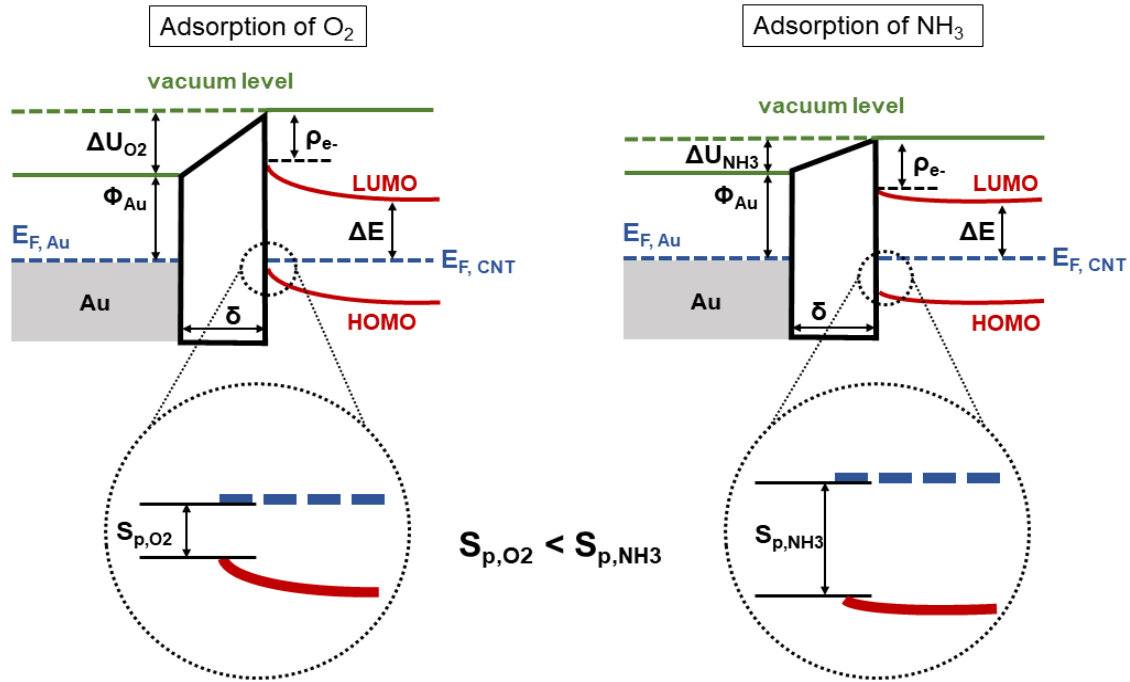
Figure 6-3 Schematic representation of contact-molecule interaction with a) O_2 as electron acceptor molecule adhering at the contact-nanotube interface and b) NH_3 as electron donor molecule adsorbed at the contact-nanotube interface.

In terms of gas sensors using CNTs as the sensing layers, two main categories can be outlined: chemresistors and chemFETs. Chemresistors are passive devices based on CNT thin-films that alter their resistance as a function of adsorbed molecules. ChemFETs are TFTs with a semiconducting CNT active layer, whose modulation effect is dependent on the adsorbed molecules. The advantage of chemFETs over chemresistors is that the TFT configuration generates a multitude of parameters from which the analyte presence can be extracted. This has further advantages when it comes to multi analyte analysis that proves to be one of the greatest challenges for chemresistors that provide a one-dimensional measurement parameter. Although the chemFETs provide an advantage in terms of data acquisition, they require a more complex fabrication and operation procedure. Regardless of the selected device type, the quality of a CNTs-based sensor is evaluated with respect to the response time t_{rsp}, which is the time period needed to alter the sensors conductance by one order of magnitude. The sensitivity E of such a sensor is given as the difference of a desired measured parameter, after and before molecule adhesion divided by the measured parameter before molecule adhesion:

$$E = \frac{x_g - x_0}{x_0} \times 100 \tag{21}$$

where x_0 is the desired sensor response in ambient conditions and x_g is the desired measured parameter after exposure to gas. Important in practice is the recovery time t_{rec} of the sensor, which is the time it takes to desorb all molecules from the CNT surface, indicated as return of the measured parameter to its initial value. Molecule desorption under ambient conditions ranges usually in the order of hours, it is therefore standard to heat the sensors with a Peltier element or by applying a bias. The heating accelerates the rate of molecule desorption, above the rate of molecule adsorption to the CNTs and therefore results in a net molecule desorption in the system [147].

In the following sections both chemresistors and chemFETs will be presented along with fabrication details and measurement approach.

6.2 Resistive Sensors

Chemresistors provide a low cost and reliable solution to gas sensing. Their simple architecture provides an ideal starting point for the investigation into gas sensing based on CNTs. As previously mentioned a significant amount of research was presented on this topic [50], [89], [148]. As such in this sub chapter we will build upon those works and investigate further concepts that go beyond the simple architecture previously presented.

6.2.1 Material and Methods

We used 2:1 semiconducting to metallic CNTs diluted in H_2O with CMC as dispersant to prepare our solution. We used spray coating for a uniform distribution of the CNT solution on the substrate. Two-inch Si wafers with SiO_2 as gate dielectric served as substrate and gate contact. We used two different fabrication techniques, thermal evaporation of Au and spray coating of CNT solution, to realize gas sensors with different contact materials. To enhance the gas adsorption area, we fabricated drain and source contacts as IDE with different channel lengths.

CNTs used were purchased from Carbon Solution Inc. They were synthesized with the CVD method and have a 1-3 wt% carboxylic acid functionalization attached. For dispersion we used the standard CMC parameters described in chapter 3.2. The solution was further diluted with H_2O in a ratio of 1:14 solution:H_2O, to achieve the desired CNT density for the active layer. For the electrodes the solution was used undiluted. To fabricate the contact structure of CNT based TFTs for gas sensing applications, we pursued two different approaches: thermal evaporation of Au contacts and spray deposition of CNT contacts.

For the sensor substrate we used two inch Si p++ wafers from MicroChemicals GmbH. The wafers had a thickness of 270 μm with dry oxidized SiO_2 of 50 nm, which served as gate dielectric. To maximize the sensor signal, we decided to fabricate the drain and source contacts as IDE structure. This approach expands the W/L ratio of the sensor channel and thus increases the current. A further benefit of the IDE structure is that the area for gas molecule adsorption is enhanced [82]. We prepared sensors with three different channel lengths of 100 μm, 200 μm and 500 μm, while maintaining a constant sensor area of 9.92 mm^2. The contact layout is schematically depicted in Figure 6-4.
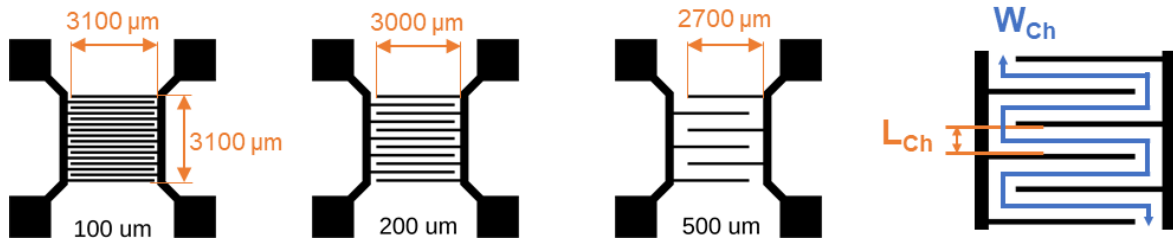

Figure 6-4 Schematic representation of the three different IDE layouts we used for the fabrication of gas sensors with thermally evaporated Au contacts. At a sensor length of 3200 μm and a sensor width of 3100 μm the finger spacing amounts for 100 μm, 200 μm and 500 μm.

The contact structure was patterned by negative photo-lithography with the ma N 1420 photoresist from micro resist technology GmbH. To achieve a uniform distribution, we deposited the photoresist on the wafer and spin-coated the sample at 50 rps for 30 s. To aid the evaporation of the residual solvent, we heated the wafer for 1 min at 100 °C.

Afterwards we masked the substrate with the IDE structure and exposed it for 15 s to UV-light. The exposed photoresist on the wafer polymerizes, while the masked part, with the IDE structure, remains un-polymerized and can be removed in the next step with the ma-D 533/S developer from micro resist technology GmbH. The contacts itself were thermally evaporated in a Univex 250 from Leybold GmbH. We deposited 5nm Cr as an adhesive layer followed by 50nm Au as contact material. In the next step we lifted the excess photoresist and gold residues off the substrate by means of an acetone bath followed by 2 min of sonication in acetone. To enable enhanced surface wetting of the wafer with the CNT solution, we modified the wafer surface at 0.3 bar O_2 plasma for 30 s at 150W. The plasma treatment increases the surface tension of the substrate by removing dangling bonds and enables a decreased contact angle of solution droplets. Afterwards we soaked the wafer for 15 min in a solution of Isopropanol and 1 wt% APTES ((3-Aminopropyl)triethoxysilane) to promote the adhesion between the nanotubes and the SiO_2.

For the deposition, we used the previously described spray deposition technique chapter 3.2 For this purpose the CNT solution was atomized by a commercially available air atomizing

spray valve from Nordson EFD. The valve is mounted on a four-axis automated motion platform above a hotplate and enabled a full cone spraying profile. We operated the nozzle in the wet spraying regime with an orifice opening of 0.7mm and a nozzle-substrate distance of 5 cm. The atomizing and material pressure were adjusted to 0.5 bar and 0.03 bar. In order to achieve a complete thin film the hotplate temperature was set to 62 °C, to enable the evaporation and merging of water droplets on the substrate. We covered the sensors with varying CNT film thickness, from three to four layers (3L & 4L), to achieve different network densities. Note, that one layer comprise one spraying process in x-direction followed by one spraying process in y-direction.

In order to remove the dispersant CMC from the nanotube network we placed the samples in an acid bath. We diluted one part of HNO_3 with four parts of DI water and soaked the wafers for at least 12 h. In the last step we removed our samples from the acid solution and dried them for 10 min at 100 °C on a hot plate, followed by a 10 min DI water bath and a subsequent drying step. Figure 6-5 schematically depicts the fabrication steps including the resulting wafer layout. For the following gas measurements we broke the wafers along the auxiliary lines in nine individual sensors.

6.2.2 DC Characterization

In preparation for the gas measurement, we fabricated a sample holder for 3-terminal characterization compatible with the gas chamber. A breadboard served as substrate and we mounted pin headers for external contacting. Two vertically adjustable probing arms were used to contact contacts on the gas sensor and simultaneously ensured a secure hold of the sensor on the sample holder. A Peltier element was mounted beneath the copper plate to enable active recovery by heating the sample and desorb gas molecules form the CNT network. We surveyed the actual temperature with a Pt100. Dimensions and assembly of the sample holder were adjusted to the dimensions of a measurement compartment of the gas setup. To confirm the sensor functionality we placed the sensor on the sample holder and connected it to a source meter. We operated the source meter via GPIB with a Simulink script executed on a personal computer. The Simulink script enabled recording the resistance of the sensor, by sourcing the current and sensing the voltage with the source meter.
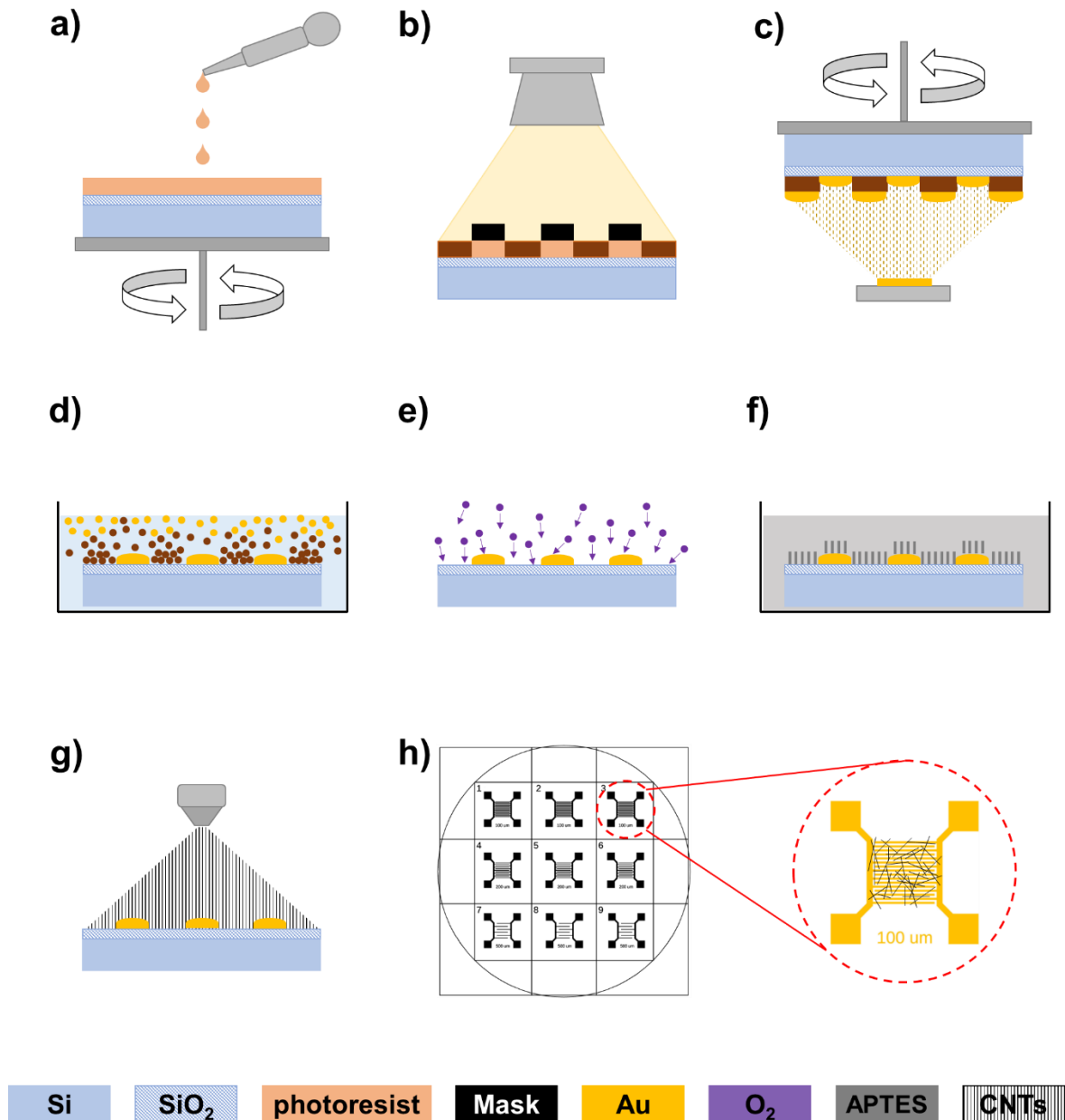
Figure 6-5 Schematic representation of the main fabrication steps we followed to fabricate gas sensors with thermally evaporated Au contacts. a) Spin-coating: application of negative photoresist on the wafer. b) Exposure process: exposed photoresist polymerizes and remains on wafer, while masked parts will be removed during development. c) Contact evaporation: deposition of evaporated Cr and Au particles on the substrate. Remaining photoresist will be removed during lift-off. d) Lift-Off: Remaining photoresist and gold particles, evaporated on top of the photoresist, are removed from the wafer in an acetone bath. e) Oxygen Plasma Treatment: surface cleaning with oxygen plasma to reduce surface tension. f) APTES treatment: soaking in APTES/Isopropanol solution to enhance CNT adhesion on the wafer. g) Spray-coating: application of a random SWCNT thin-film on the wafer. h) Final wafer layout: nine gas sensors per wafer with different channel length. The magnification shows a schematic of a random SWCNT network on one of the sensors.

To perform a gas measurement we placed one sensor on the sample holder and introduced it to the measurement compartment, which was then sealed hermetically. The measurement compartment was connected to a gas flow controller, which regulated the gas supply of carrier gas and test gas. We controlled the gas flow controller with a LabView script implemented on a personal computer. The LabView script enabled continuous measurements with successive cycles of gas supply and sensor recovery. The same software also controlled a Keithley 2602B system source meter, which triggered the Peltier element for a stable environmental temperature and surveyed the temperature recorded by the Pt 100. We adjusted the regular measurement temperature to 30 °C and increased it to 80 °C for active recovery of the CNT sensor. Figure 6-6 displays the experimental setup, schematically.
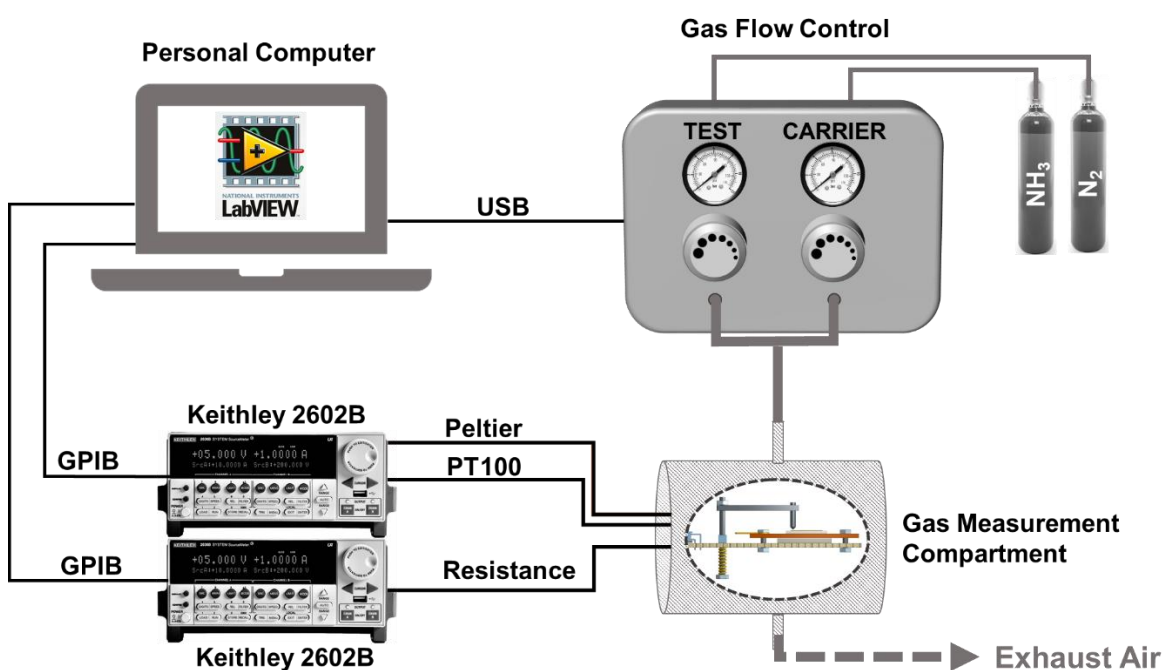

Figure 6-6 Schematic representation of the experimental setup we established for gas measurements consisting of: gas chamber, gas flow controller, source meters and a PC controlling the devices over a LabView interface.

In this work, we analyzed the response of the CNT sensor on different concentrations of NH_3. The test gas was mixed with a carrier gas, to achieve the desired concentration, while maintaining a constant gas flux of 200 mL/min. Here, N_2 served as carrier gas. One measurement routine comprised of four consecutive cycles of the following measurement steps: 600 s standard measurement at 30 °C, 300 s of gas flow and 300 s of active recovery at 80 °C. In each cycle we altered the test gas concentration. Note that the test gas concentrations correspond to 10, 25, 50 and 100 ppm, respectively.

6.2.3 Time Stability Measurements

The initial investigation was to determine the stability of the gas sensors over an extended period of time. This was done as a proof of concept as to the time stability of sensors in ambient conditions. The sensors were stored in a lab without any passivation as to emulate conditions in which such a sensor could be used. For the investigation the sensor was measured as fabricated, after one year and after four years. In Figure 6-7 the raw resistance of the film is plotted vs expired time. The shaded areas represent the various measuring regimes: red recovery, black: cooling down and green: measurement time. Visible is the increase in resistance with time (9.5 kΩ to 12.5 kΩ). This degradation in film conduction is a result of foreign molecules such as CO_2, O_2 and H_2O binding to the CNTs which are not fully desorbed during the active recovery cycles. This is also seen in the sensor response to the gas as with time the sensor response decreases. This can be seen further below
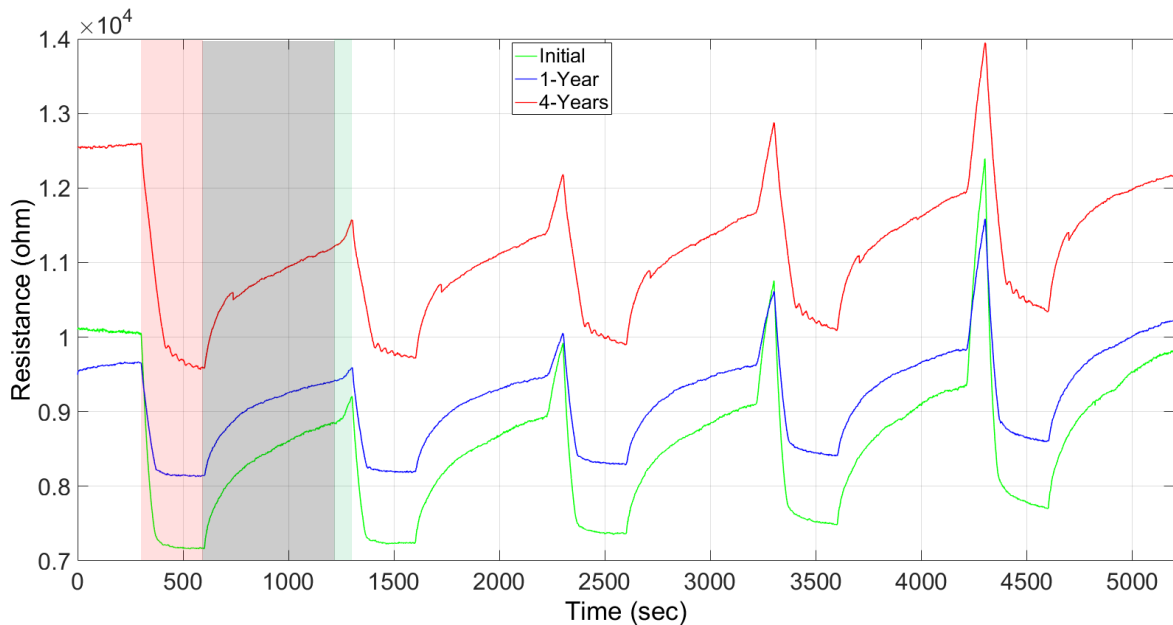

Figure 6-7 Figure representing resistance time response to NH_3 of a 4L CNT sensor with Au contacts with a finger spacing of 200 µm. The green line represents the initial measurement, the blue line one year after fabrication and the red line four years after fabrication. The shaded areas represent the various measurement conditions that repeat themselves: red active recovery: 200 mL/min N_2 at 30°C. black: 200 mL/min N_2 cooling to 30°C. green: mixture of N_2 and NH_3 increasing from 10ppm to 100ppm NH_3 (10, 25, 50 , 100 ppm). [Results published in [149]]

Figure 6-8 represents a typical measurement plot. Although sensor response can be seen, for a better visualization the normalized response was plotted for the 10, 25, 50 and 100 ppm NH_3 concentrations.
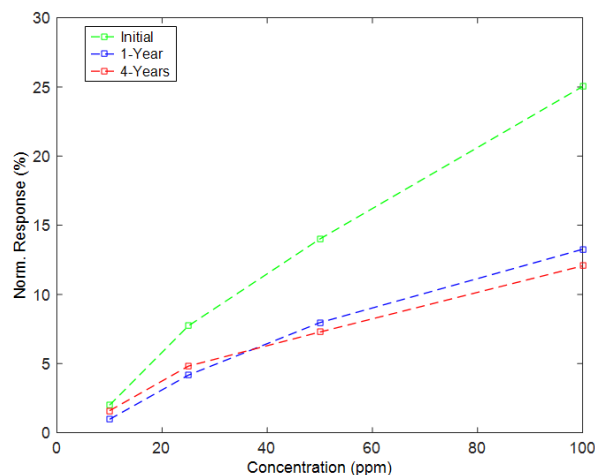
Figure 6-8 Figure representing normalized response to NH$_3$ of a 4L CNT sensor with Au contacts with a finger spacing of 200 µm. The green line represents the initial measurement, the blue line one year after fabrication and the red line four years after fabrication. [Results published in [149]]

In terms of sensor response after the first year there is a decrease of ca 40% at 10 ppm, 45% at 25 ppm, 50% at 50 ppm and 60% at 100 ppm. This ties in with the assumption that the CNT network adsorbs other molecules such as O$_2$ and H$_2$O which then block binding sites for the NH$_3$. This however would need to be further investigated however, it has been reported in literature [150]. The difference between one and four years is negligible in comparison. To summarize the results presented demonstrate the stability of CNT-film based gas sensors, answering to one of the main research questions related to solution-processed sensors.

6.2.4 Full CNT Devices

So far, we have shown the long-term stability of our sensors, although there is a decrease in response, sensor functionality is still given. From a technological point of view the current process has some high barriers with the use of Au electrodes. The evaporation process is a high temperature high vacuum process that has both cost and substrate limitations. In addition the gold electrodes are non-transparent reducing some of the functionality of the device. As such we propose to replace the Au electrodes with spray deposited CNT electrodes that were presented in [75], [151]. For the comparison we fabricated the previously mentioned Au based sensors with 50 µm, 100 µm and 200 µm spacing. The reduction in spacing was purposefully done as a consideration for the CNT electrodes as these raise the total sensor resistance. For the CNT sensors a full 20 layer was patterned by photolithography. We masked the substrate with the IDE structure and exposed it for 15 s to UV-light. We developed the resist ma-D 533/S developer from micro resist technology GmbH. Using a 3 min 100W O$_2$ plasma we etched away the unwanted CNTs and

subsequently removed the remainder of the photo resist with a 10 min isopropanol bath. 50 µm, 100 µm and 200 µm spacing, sensors were fabricated. The spray deposition was identical for both wafers with a 4L being deposited. The resulting device as well as the critical processing steps can be schematically see in Figure 6-9.
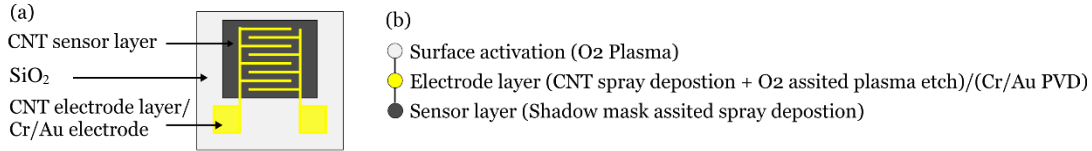

Figure 6-9 a) Schematic representation of resulting sensors with key layers marked. b) key processing steps for the resulting sensor.

The initial characterization was done for the 4L CNT sensor for the 50 µm, 100 µm and 200 µm with respect to NH_3 at 10 ppm, 25 ppm, 50 ppm and 100 ppm. The results are depicted in Figure 6-10. For better visual comparison, the normalized resistance was plotted.
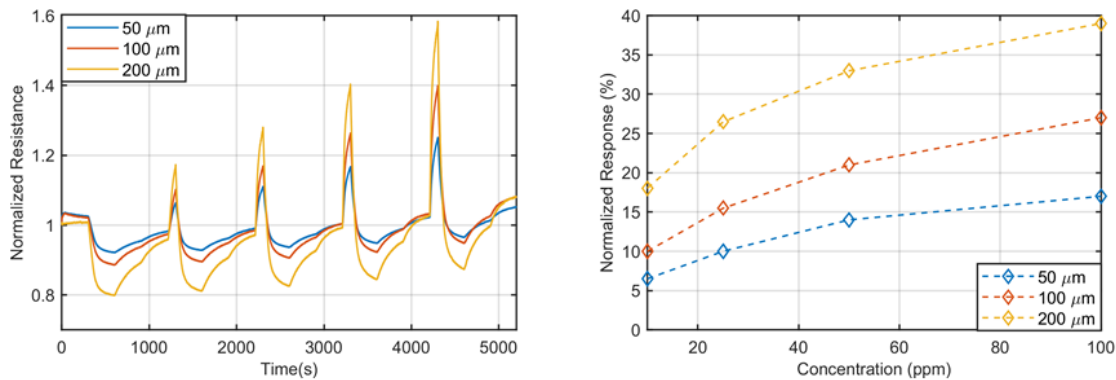

Figure 6-10 a) Figure representing normalized resistance time response to NH_3 of a 4L CNT sensor with CNT contacts with a finger spacing of 50 µm (blue), 100 µm (red) and 200 µm (yellow) when exposed to mixture of N_2 and NH_3 increasing from 10 ppm to 100 ppm NH_3 (10, 25, 50 , 100 ppm). b) figure representing normalized response to NH_3 of a 4L CNT sensor with CNT contacts with a finger spacing of 50 µm (blue), 100 µm (red) and 200 µm (yellow)

The normalized response for the 50 µm is approx. 6%, 10%, 14% and 17% for 10, 25, 50 and 100 ppm NH_3 concentrations. For the 100 µm, approx. 10%, 16%, 21% and 27% for 10, 25, 50 and 100 ppm NH_3 concentrations and for the 200 µm, approx. 17%, 27%, 33% and 39% for % for 10, 25, 50 and 100 ppm NH_3 concentrations. Clearly visible is that the 200 µm spacing sensors outperforms the other spacing although all sensor responses show a positive linear correlation with increasing NH_3 concentration. The decrease in response is directly proportional to reduction in channel length. This effect is not present in Au electrodes as will be seen further below. The causation for this decrease in sensor response can be correlated to the electrode structure that significantly increases the total sensor

resistance of the device. An effect, which is, not present for the Au electrodes where the series electrode resistance is 10^3 orders of magnitude lower that the channel resistance where as for the CNT electrodes is in the same order of magnitude. As such the change in total resistance caused by the exposure to NH_3 is proportionally smaller than for the Au system.

In addition to the NH_3 characterization and the current need for CO_2 sensors we decided to expand our comparison to this gas as well. As such we repeated the experiment while fluxing 500 ppm, 1000 ppm, 2500 ppm and 5000 ppm mixed with dry air. The range of measurement corresponds to the critical levels of CO_2 concentrations for health and air quality monitoring. The results are plotted in Figure 6-11. For better visual comparison, the normalized resistance was plotted.
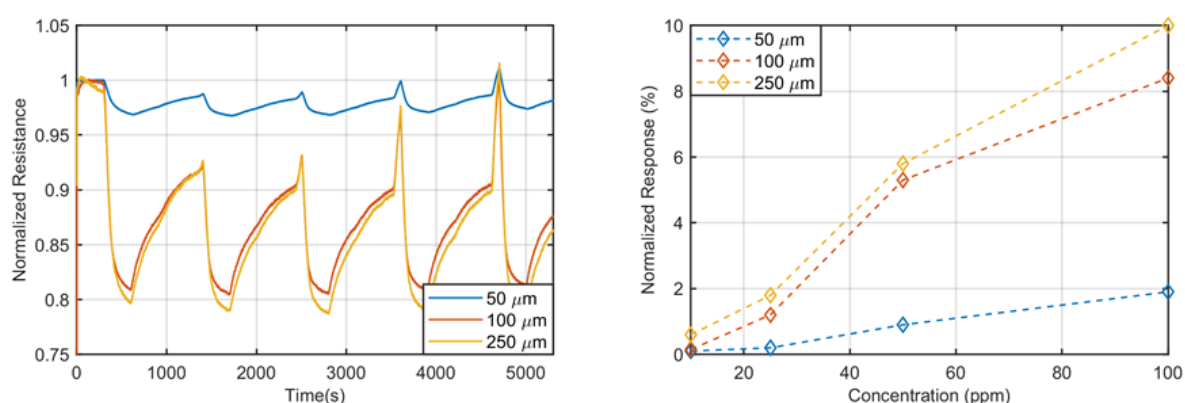

Figure 6-11 Figure representing normalized resistance time response to CO_2 of a 4L CNT sensor with CNT contacts with a finger spacing of 50 µm (blue), 100 µm (red) and 200 µm (yellow) when exposed to mixture of dry air and CO_2 increasing from 500 ppm to 5000 ppm CO_2 (500, 1000, 2500 , 5000 ppm). b) figure representing normalized response to CO_2 of a 4L CNT sensor with CNT contacts with a finger spacing of 50 µm (blue), 100 µm (red) and 200 µm (yellow)

The normalized response for the 50 µm is approx. 0.1%, 0.2%, 1% and 2% for 500, 1000, 2500 , 5000 ppm CO_2 concentrations. For the 100 µm, approx. 0.1%, 1%, 5% and 8% for 500, 1000, 2500 , 5000 ppm CO_2 concentrations and for the 200 µm, approx. 0.5%, 1.2%, 5.8% and 10% for 500, 1000, 2500 , 5000 ppm CO_2 concentrations. Similarly, to the NH_3 a positive correlation with increasing CO_2 concentration is present. The same decrease in response with decreasing channel length is present as with NH_3 however the difference between 100 µm and 200 µm is not as pronounced. For a comparison with the Au electrodes, both experiments were repeated and the normalized response is plotted in Figure 6-12.
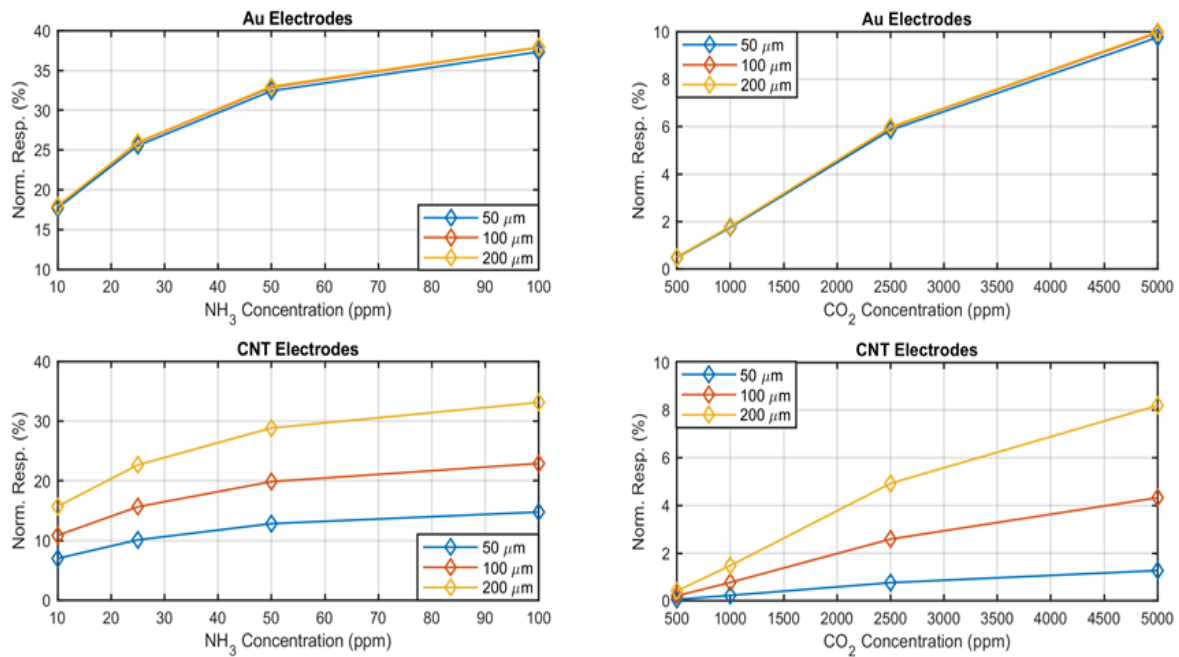
Figure 6-12 a) figure representing normalized response to NH_3 of a 4L CNT sensor with Au contacts with a finger spacing of 50 µm (blue), 100 µm (red) and 200 µm (yellow). b) figure representing normalized response to CO_2 of a 4L CNT sensor with Au contacts with a finger spacing of 50 µm (blue), 100 µm (red) and 200 µm (yellow). c) figure representing normalized response to NH_3 of a 4L CNT sensor with CNT contacts with a finger spacing of 50 µm (blue), 100 µm (red) and 200 µm (yellow). d) figure representing normalized response to CO_2 of a 4L CNT sensor with CNT contacts with a finger spacing of 50 µm (blue), 100 µm (red) and 200 µm (yellow)

In terms of response, the CNT electrode sensor slightly underperforms the Au electrode sensor however, this holds true only for the 200 µm channel. Also visible is the slight reduction in response when compared to the initial set of experiments. This raises a question of reproducibility. As presented in the previous section the CNT sensors experience reduced conductivity with exposure to ambient conditions. This effect would be amplified with a full CNT sensor. As such a more detailed experimental series would be need in order to investigate both the stability as well as the reproducibility issues. Nevertheless, the presented results show a promising proof of concept to an initial step to remove Au from the sensor system and as such greatly reduce cost while increasing sensor functionality although at a tradeoff for time stability. In the following subchapter, we will introduce another strategy to reduce both costs and fabrication complexity with regard to the fabrication of CNT based gas sensors.

6.3 Low-cost written sensors

Although the previously shown designs show great potential for large area mass production, we were interested in exploring a simpler processing technique that reduces the cost of acquiring machinery especially targeting the quick prototyping sector. With this in mind, a new trend known as handwritten electronics has begun to emerge [152]. One such technique is the use of a graphite pencil to define electrodes for paper-based fuel cells [153] or to define resistors [154]. In addition to this, efforts have been made in creating active compounds and compressing these into "pencil like" leads, which are subsequently used to generate functional devices on paper [155], [156]. In addition to this ball and fountain pens have been used to generate light emitting diodes (LEDs) [157], and bio catalytic sensors for in home low-cost diabetes diagnosis [158]. As such in the following subchapter we will attempt to combine the previously developed CNT ink with the handwritten technology to fabricate chemresistors. In order to show the feasibility of this technology we will expand the tested gasses to CO and ethanol in addition to the NH_3 and CO_2 previously measured.

6.3.1 Sensor fabrication

The devices we fabricated with the aid of a ballpoint pen (Schmidt Technology). The ball diameter is 0.7 mm. The pen was mounted in a 2D-stage plotter (AxiDraw) and controlled over an Inkscape addon. No additional weight was added to improve contact as to not damage soft substrates. The movement speed of the pen was fixed at 25 mm/s with 90° and 180° angle hatching as to improve contact conductance and reduce defects. As a substrate a polypropylene poster foil was used (EMBLEM). The process was performed in ambient lab conditions. For the active layer we used CNTs from Carbon Solution Inc. diluted in H_2O with SDS as dispersant to prepare our solution. For details please see chapter 3.2. Contacts were drawn from a silver nanoparticle ink (AgNP) (Sigma-Aldrich) with a content of 30-35 wt% with a particle size on < 50 nm in triethylene glycol monomethyl ether (TGME). The samples were subsequently photonically sintered (Xenon) at a pulse width of 500 µs at a period of 1s repeated 15 times [159]. Figure 6-13 represents the setup as well as a schematic of the sensor. The sensor layout differs slightly from the evaporated contacts in previous subchapters. This change was performed as to accommodate decrease the chance of creating unwanted short circuits. The finger spacing is set at 200µm.

In order to verify the resulting areas SEM images (NVision40 from Carl Zeiss) were taken of both contacts and active layer. Images were taken at extraction and acceleration voltages of 5 and 7 kV respectively with a working distance of 5-6 mm. The resulting images can be seen in Figure 6-14. Figure 6-14 a (5k x) and b (25k x) are of the Ag film.

(a)

(b)
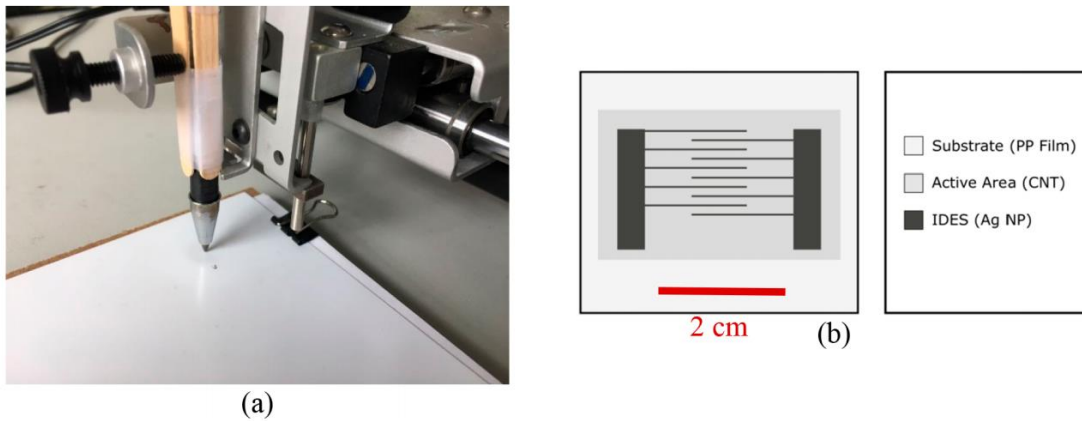
Figure 6-13 Photograph of ball pen in the robot arm employed to develop the printed sensor. (b) Schematic of the sensor depicting critical layers. [Results published in [160]]

In the lower magnification cracks are visible which are resulting of the flexible substrate that has been exposed to bending. At the higher magnification a good "necking" of the NPs can be observed. Necking is the melding of NPs together to reduce the contact resistance between individual particles. Figure 6-14 c (20k x) and d (200k x) display a homogenous film at lower magnification with a good debundling at higher magnification characteristic of our ink. A set of 20 sensors was written with a nominal value of resistance measure at ambient conditions of 1.6 ± 0.3 kΩ.

Figure 6-14 (a-b) Scanning electron microscope image of silver nanoparticle film at (a) 5k and (b) 25k magnification. (c-d) Scanning electron microscope image of CNT film at (a) 20k and (b) 200k magnification. The red circle depicts the higher magnification region. [Results published in [160]]

6.3.2 DC Characterization

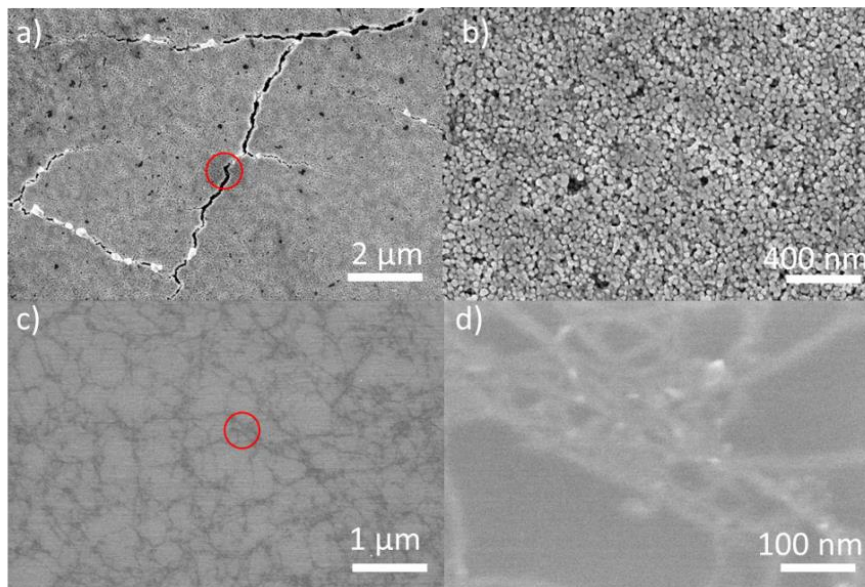For the DC characterization of the sensors, the sample was fixated on a sample holder with an additional Peltier element, for sensor thermal recovery, and a PT 100 sensor for temperature monitoring. Dimensions and assembly of the sample holder were adjusted to the dimensions of a measurement compartment of the gas setup. To confirm the sensor functionality we placed the sensor on the sample holder and connected it to a source meter. We operated the source meter via GPIB with a Simulink script executed on a personal computer. The Simulink script enabled recording the resistance of the sensor, by sourcing the current and sensing the voltage with the source meter. To perform a gas measurement we placed one sensor on the sample holder and introduced it to the measurement compartment, which was then sealed hermetically. The measurement compartment was connected to a gas flow controller, which regulated the gas supply of carrier gas and test gas. We controlled the gas flow controller with a LabView script implemented on a personal computer. The LabView script enabled continuous measurements with successive cycles of gas supply and sensor recovery. The same software also controlled a Keithley 2602B system source meter, which triggered the Peltier element for a stable environmental temperature and surveyed the temperature recorded by the Pt 100. We adjusted the regular measurement temperature to 30 °C and increased it to 60 °C for active recovery of the CNT sensor. In this section, we analyzed the response of the CNT sensor on different concentrations of NH_3, CO_2, CO and ethanol. The test gas was mixed with a carrier gas, to achieve the desired concentration, while maintaining a constant gas flux of 200 mL/min. Here, N_2 served as carrier gas for NH_3. CO, ethanol and dry air for CO_2. One measurement routine comprised of four consecutive cycles of the following measurement steps: 600 s standard measurement at 30 °C, 300 s of gas flow and 300 s of active recovery at 60 °C. In each cycle we altered the test gas concentration. Note that the test gas concentrations correspond to 10, 25, 50 and 100 ppm, for NH_3 respectively. For CO_2: 500, 1000, 2500 and 5000 ppm. For CO: 5, 10, 20 and 40 ppm and for ethanol: 5, 20, 45 and 90 ppm.

The initial gas characterization was performed for NH_3 with the results shown in Figure 6-15. The normalized response for the sensor is approx. 4%, 14%, 19% and 33% for 10, 25, 50 and 100 ppm NH_3 concentrations.

Figure 6-15 Figure representing normalized resistance time response to NH_3 of a written CNT sensor with AgNP contacts with a finger spacing of 200 µm when exposed to mixture of N_2 and NH_3 increasing from 10 ppm to 100 ppm NH_3 (10, 25, 50 and 100 ppm.). b) figure representing normalized response to NH_3 of a written CNT sensor with AgNP contacts with a finger spacing of 200 µm. [Results published in [160]]

Clearly visible from the measurement is the very pronounced baseline drift. This drift can be in part attributed to the insufficient active recovery cycle that was performed at 60 °C rather than at the previously established 80 °C. The desorption rate of molecules is strongly correlated to the active recovery temperature and as such the recovery time should be increased to compensate for the decreased recovery temperature. Due to the physical properties of the used substrate, we are limited to < 60 °C, as higher temperature would lead to substrate damage. Despite of the strong baseline drift, the measured response is comparable with the Au sensors presented in the previous subchapter. For the remainder of CO_2, CO and ethanol the measurement results and normalized response are presented in Figure 6-16, Figure 6-17 and Figure 6-18 respectively.
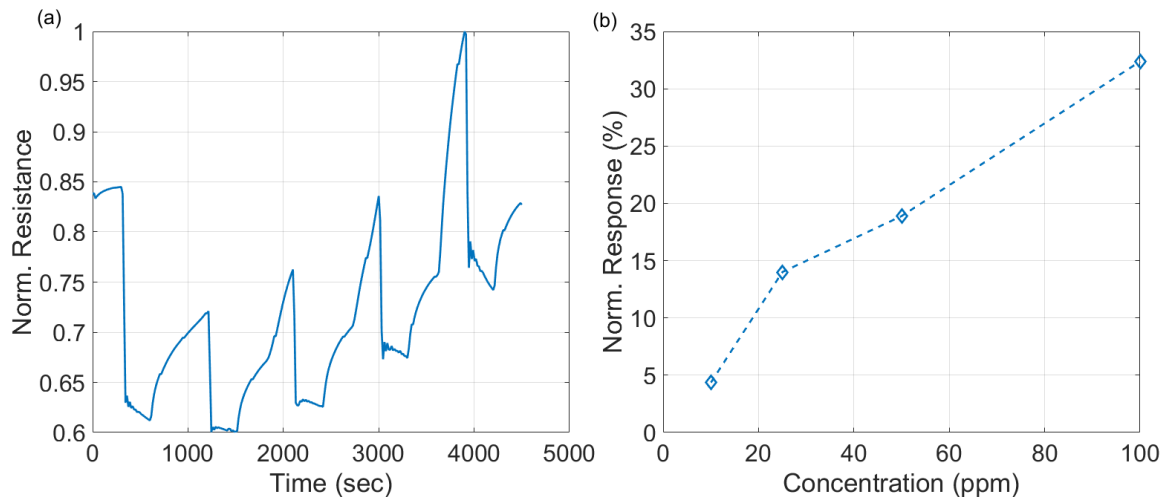
Figure 6-16 a) Figure representing normalized resistance time response to CO_2 of a written CNT sensor with AgNP contacts with a finger spacing of 200 µm when exposed to mixture of dry air and CO_2 increasing from 500 ppm to 5000 ppm CO_2 (500, 1000, 2500, 5000 ppm). b) figure representing normalized response to CO_2 of a written CNT sensor with AgNP contacts with a finger spacing of 200 µm. [Results published in [160]]

Figure 6-17 a) Figure representing normalized resistance time response to CO of a written CNT sensor with AgNP contacts with a finger spacing of 200 µm when exposed to mixture of N_2 and CO increasing from 5 ppm to 40 ppm CO (5, 10, 20 and 40 ppm). b) figure representing normalized response to CO of a written CNT sensor with AgNP contacts with a finger spacing of 200 µm. [Results published in [160]]
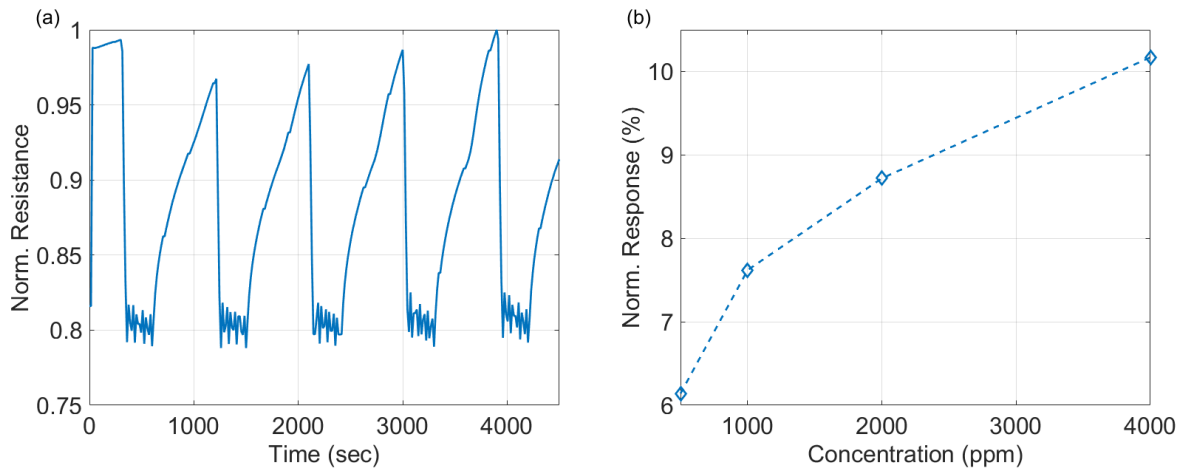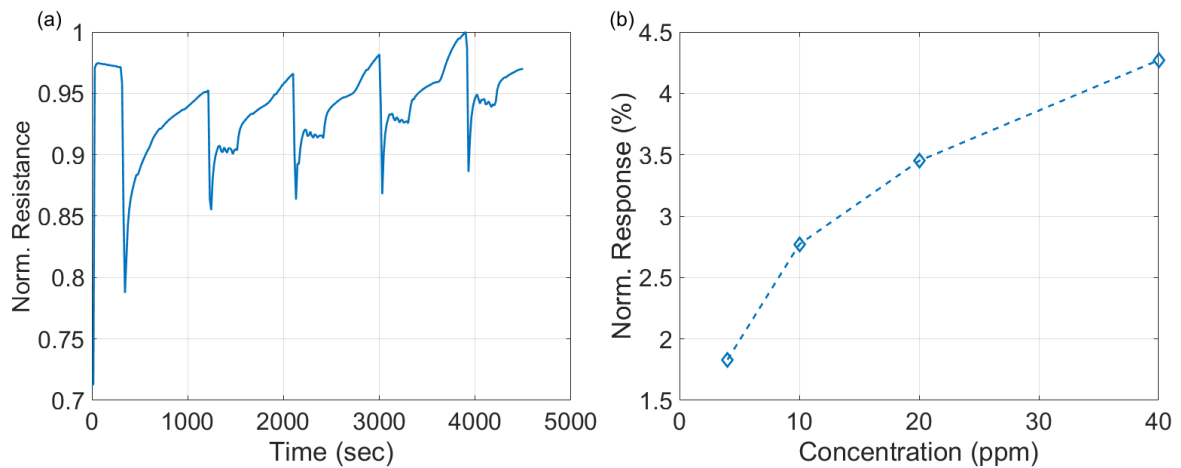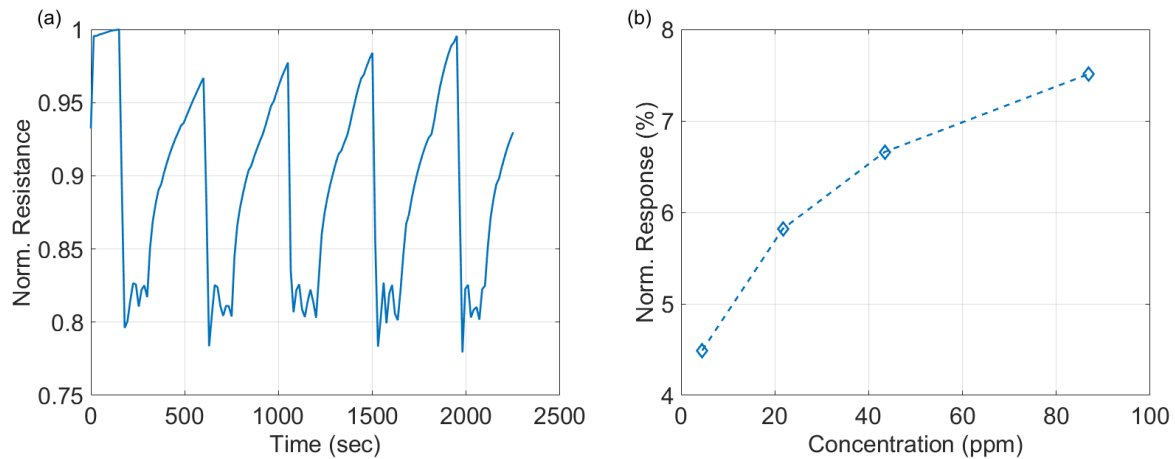
Figure 6-18 Figure representing normalized resistance time response to ethanol of a written CNT sensor with AgNP contacts with a finger spacing of 200 μm when exposed to mixture of N_2 and ethanol increasing from 5 ppm to 90 ppm CO (5, 20, 45 and 90 ppm.). b) figure representing normalized response to ethanol of a written CNT sensor with AgNP contacts with a finger spacing of 200 μm. [Results published in [160]]

The normalized response for the sensor when exposed to CO_2 is approx. 6%, 7.5%, 8.4% and 11% for 500, 1000, 2500 and 5000 ppm CO_2 concentrations. The normalized response for the sensor when exposed to CO is approx. 1.7%, 2.8%, 3.5% and 4.3% for 5, 10, 20 and 40 ppm CO concentrations. The normalized response for the sensor when exposed to ethanol is approx. 4.5%, 5.8%, 6.5% and 7.5% for 5, 20, 45 and 90 ppm ethanol concentrations. For all gasses, a positive correlation with increasing gas concentration is visible. Noticeable from the measurement curves however is that the sensor gives a similar response to different gasses at various ppm. In a controlled environment it is possible to correlate the sensor response to a given gas concentration, however where the sensor used for example in an office environment as an air quality sensor, it would give positives if the desired gas measured were CO_2 for example. This poses a challenge and limitation in regards to the usability of the presented sensors. Nevertheless, these problems are also applicable to the Au based sensors initially presented. The here presented method and results are to show a proof of concept with respect to the technology and its feasibility.

6.4 CNT TFT Sensor

Although chemresistors provide a low cost and reliable solution to gas sensing, multi analyte sensing provides a challenge that can then no longer be easily solve and greatly increases both fabrication complexity and costs, as well as the required measurement setup and data

analysis. As such in this sub chapter we will investigate the feasibility of chemFETs based on CNTs at the proof of concept level.

6.4.1 Sensor fabrication

We used 90% semiconducting CNTs diluted in H_2O with CMC as dispersant to prepare our solution. We used spray coating for a uniform distribution of the CNT solution on the substrate. Two-inch Si wafers with SiO_2 as gate dielectric served as substrate and gate contact. We used two different fabrication techniques, thermal evaporation of Au and screen printing of Ag, to realize gas sensors with different contact materials. Due to different work functions of Au and Ag we expect a variation in the gating behavior between both sensor types. To enhance the gas adsorption area, we fabricated drain and source contacts as IDE with different channel lengths.

CNTs used were purchased from Merck. The structure of the nanotubes is specified as zig-zag with a chirality of (6,5), while the average length and diameter are denoted to $L_{nt} = 1$ μm and $d_{nt} = 0:78$ nm. They were synthesised with the CoMoCAT TM catalytic CVD method. For dispersion we used the standard CMC parameters described in [sectionref]. The solution was further diluted with H_2O in a ratio of 1:14 solution:H_2O, to achieve the desired CNT density. To fabricate the contact structure of CNT based TFTs for gas sensing applications, we pursued two different approaches: thermal evaporation of Au contacts and screen printing of Ag contacts. Both approaches are briefly introduced in the following paragraphs.

To fabricate gas sensors with Au contacts we decided for the bottom-gated coplanar structure, so that the CNT thin-film remains unharmed during processing. As a substrate we used two inch Si p++ wafers from MicroChemicals GmbH, which additionally functioned as gate contact. The wafers had a thickness of 270 μm with dry oxidized SiO_2 of 50 nm, which served as gate dielectric. Since we expect low currents in the nA range, we decided to fabricate the drain and source contacts as IDE structure. This approach expands the W/L ratio of the transistor channel and thus increases the drain current. A further benefit of the IDE structure is that the area for gas molecule adsorption is enhanced. We prepared sensors with three different channel lengths of 100 μm, 200 μm and 500 μm, while maintaining a constant sensor area of 9.92 mm^2. The contact layout is schematically depicted in Figure 6-19.
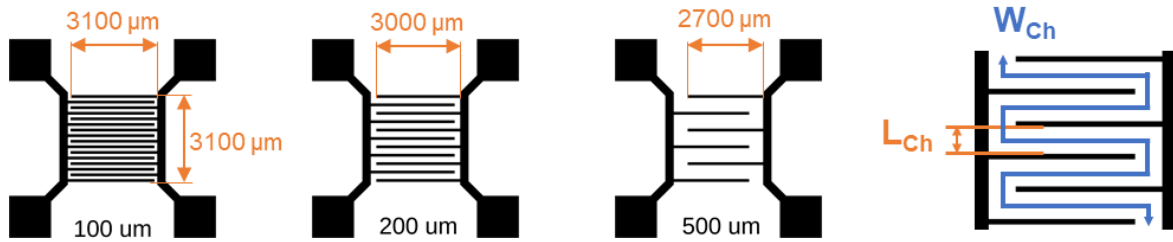
Figure 6-19 Schematic representation of the three different IDE layouts we used for the fabrication of gas sensors with thermally evaporated Au contacts. At a sensor length of 3200 μm and a sensor width of 3100 μm the finger spacing amounts for 100 μm, 200 μm and 500 μm.

The contact structure was patterned by negative photo-lithography with the ma N 1420 photoresist from micro resist technology GmbH. To achieve a uniform distribution, we deposited the photoresist on the wafer and spin-coated the sample at 50 rps for 30 s. To aid the evaporation of the residual solvent, we heated the wafer for 1 min at 100 °C.

Afterwards we masked the substrate with the IDE structure and exposed it for 15 s to UV-light. The exposed photoresist on the wafer polymerizes, while the masked part, with the IDE structure, remains un-polymerized and can be removed in the next step with the ma-D 533/S developer from micro resist technology GmbH. The contacts itself were thermally evaporated in a Univex 250 from Leybold GmbH. We deposited 5nm Cr as an adhesive layer followed by 50nm Au as contact material. In the next step we lifted the excess photoresist and gold residues off the substrate by means of an acetone bath followed by 2 min of sonication in acetone. To enable enhanced surface wetting of the wafer with the CNT solution, we modified the wafer surface at 0.3 bar O_2 plasma for 30 s at 150W. The plasma treatment increases the surface tension of the substrate by removing dangling bonds and enables a decreased contact angle of solution droplets. Afterwards we soaked the wafer for 15 min in a solution of Isopropanol and 1 wt% APTES ((3-Aminopropyl)triethoxysilane) to promote the adhesion between the nanotubes and the SiO_2.

For the deposition, we used the previously described spray deposition technique chapter 3.2. For this purpose the CNT solution was atomized by a commercially available air atomizing spray valve from Nordson EFD. The valve is mounted on a four-axis automated motion platform above a hotplate and enabled a full cone spraying profile. We operated the nozzle in the wet spraying regime with an orifice opening of 0.7mm and a nozzle-substrate distance of 5 cm. The atomizing and material pressure were adjusted to 0.5 bar and 0.03 bar. In order to achieve a complete thin film the hotplate temperature was set to 62 °C, to enable the evaporation and merging of water droplets on the substrate. We covered the sensors with varying CNT film thickness, from three to four layers (3L & 4L), to achieve different network densities. Note, that one layer comprise one spraying process in x-direction followed by one spraying process in y-direction.

In order to remove the dispersant CMC from the nanotube network we placed the samples in an acid bath. We diluted one part of HNO_3 with four parts of DI water and soaked the wafers for at least 12 h. In the last step we removed our samples from the acid solution and dried them for 10 min at 100 °C on a hot plate, followed by a 10 min DI water bath and a subsequent drying step. Figure 6-21 schematically depicts the fabrication steps including the resulting wafer layout. For the following gas measurements we broke the wafers along the auxiliary lines in nine individual sensors. Figure 6-20 depicts the final sensor with a 5 cent coin as size reference and an inlet AFM image displaying the resulting CNT layer.
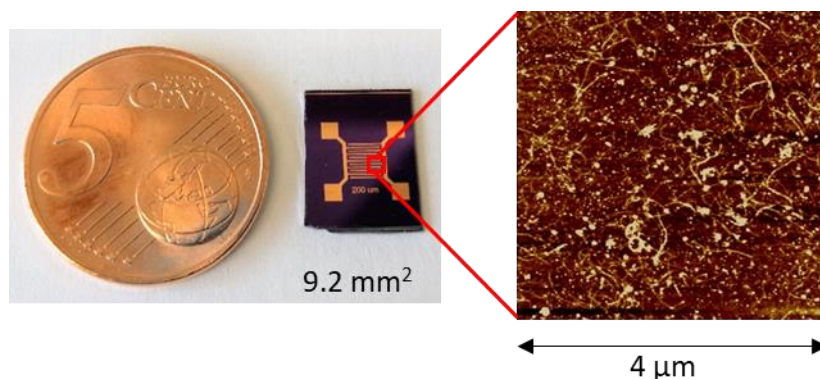
Figure 6-20 Resulting CNT based sensor with Au contacts diced from the wafer with a 5 cent coin as size reference. The inlet displays a 4 µm x 4µm AFM image of the sensor area.

For the Ag contacts a screen printing technique developed by Albrecht et. al was used [161]. Screen printing usually enables thick structures in the µm range. If applying a CNT thin-film on top of the printed contact structure, the structure thickness could disrupt the nanotube network, as the average nanotube length is only 1 µm. Additionally we decided to print the contacts with Ag ink, which oxidize to silver-nitrate in combination with HNO_3, the acid we used to remove the dispersant CMC from the CNT network. Therefore, we choose a bottom gated staggered structure and applied the CNT solution on the substrate before printing the contact structure.

Figure 6-21 Schematic representation of the main fabrication steps we followed to fabricate gas sensors with thermally evaporated Au contacts. a) Spin-coating: application of negative photoresist on the wafer. b) Exposure process: exposed photoresist polymerizes and remains on wafer, while masked parts will be removed during development. c) Contact evaporation: deposition of evaporated Cr and Au particles on the substrate. Remaining photoresist will be removed during lift-off. d) Lift-Off: Remaining photoresist and gold particles, evaporated on top of the photoresist, are removed from the wafer in an acetone bath. e) Oxygen Plasma Treatment: surface cleaning with oxygen plasma to reduce surface tension. f) APTES treatment: soaking in APTES/Isopropanol solution to enhance CNT adhesion on the wafer. g) Spray-coating: application of a random SWCNT thin-film on the wafer. h) Final wafer layout: nine gas sensors per wafer with different channel length. The magnification shows a schematic of a random SWCNT network on one of the sensors.

As mentioned we expect low currents in the nA range and decided to print the drain and source contacts as IDE structure. We prepared sensors with four different finger widths and the channel lengths of 100/100 µm, 100/150 µm, 150/150 µm and 150/225 µm, while maintaining a constant sensor area of 26.775 mm². The contact layout is schematically depicted in Figure 6-22.
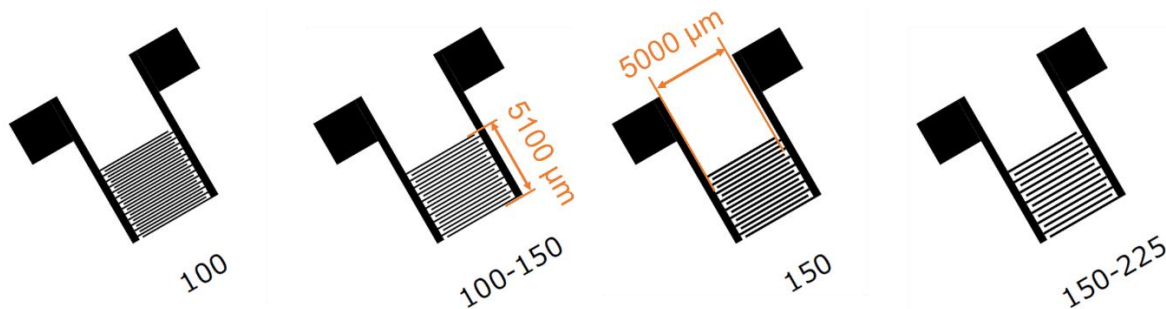
Figure 6-22 Schematic representation of the four different IDE layouts we used for the fabrication of gas sensors with screen printed Ag contacts. At a sensor length of 5100 µm and a sensor width of 5000 µm, finger width and the channel length of each sensor amounts for 100/100µm, 100/150µm, 150/150µm and 150/225µm, respectively.

As substrate the same two inch Si p++ wafers were used as for the Au samples. The wafer treatment before printing of the contacts was also similar to the wafer treatment used for the Au contacts. To enable enhanced surface wetting of the wafer with the CNT solution, we modified the wafer surface with 0:3 bar O_2 plasma for 30 s at 150W. Afterwards we soaked the wafer for 15 min in a solution of Isopropanol and 1 wt% APTES to promote the adhesion between the nanotubes and the SiO_2.

For the deposition, we used the previously described spray deposition technique We operated the nozzle in the wet spraying regime with an orifice opening of 0.7mm and a nozzle-substrate distance of 5 cm. The atomizing and material pressure were adjusted to 0.5 bar and 0.03 bar. In order to achieve a complete thin film the hotplate temperature was set to 62 °C, to enable the evaporation and merging of water droplets on the substrate. We covered the sensors with varying CNT film thickness, from 2L to 5L, to achieve different network densities. For the CMC removal the same protocol of diluted HNO_3 for 12h followed by drying 10 min at 100 °C on a hot plate, followed by a 10 min DI water bath and a subsequent drying step.

For printing Ag contacts we adapted a screen printing technique, which was successfully used by members of our team to print conductive patterns. We used the Nino screen printer from Coruna GmbH, which is a manual printing machine that can be operated with one hand. The Nino was designed for small and fast prints and comes with a vacuum table to fixate the substrate. The screen was bought from Siebdruckversand and has mesh count of 165, which

is the number of threads per cm^2. Each opening in the mesh has a dimension of 33 μm x 28 μm. For the contact structure we used the LOCTITE ECI 1011 E&C Ag ink from Henkel Electronic Materials, which features a particle size < 2 μm. We printed with a 3-layer squeegee from RK Siebdrucktechnik GmbH, with a layer hardness of 75, 95 and 75 Shore to achieve optimum printing results. After printing the samples were dried for at least 10 min at 100 °C, to cure the Ag ink. For the following gas measurements, we broke the wafers in four individual sensors. Figure 6-23 depicts the final sensor with a 5 cent coin as size reference and an inlet AFM image displaying the resulting CNT layer.
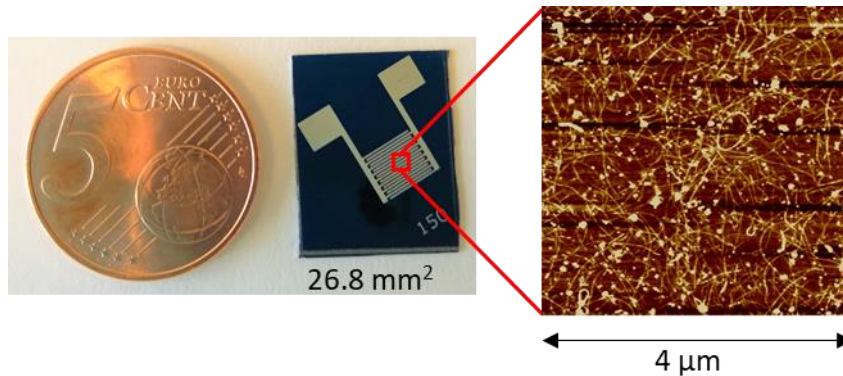
Figure 6-23 Resulting CNT based sensor with screen printed Ag contacts diced from the wafer with a 5 cent coin as size reference. The inlet displays a 4 μm x 4μm AFM image of the sensor area.

Figure 6-24 schematically depicts the fabrication steps including the resulting wafer layout. Before characterizing the gas sensors, we heated the wafers for 30 min at 100 C to desorb H_2O and O_2 molecules, which are absorbed on the Si surface in ambient conditions. Afterwards we removed the layer of oxidized Si from the rear side of the wafer, in order to establish a gate contact. Note, that these steps had been repeated in advance of every measurement.
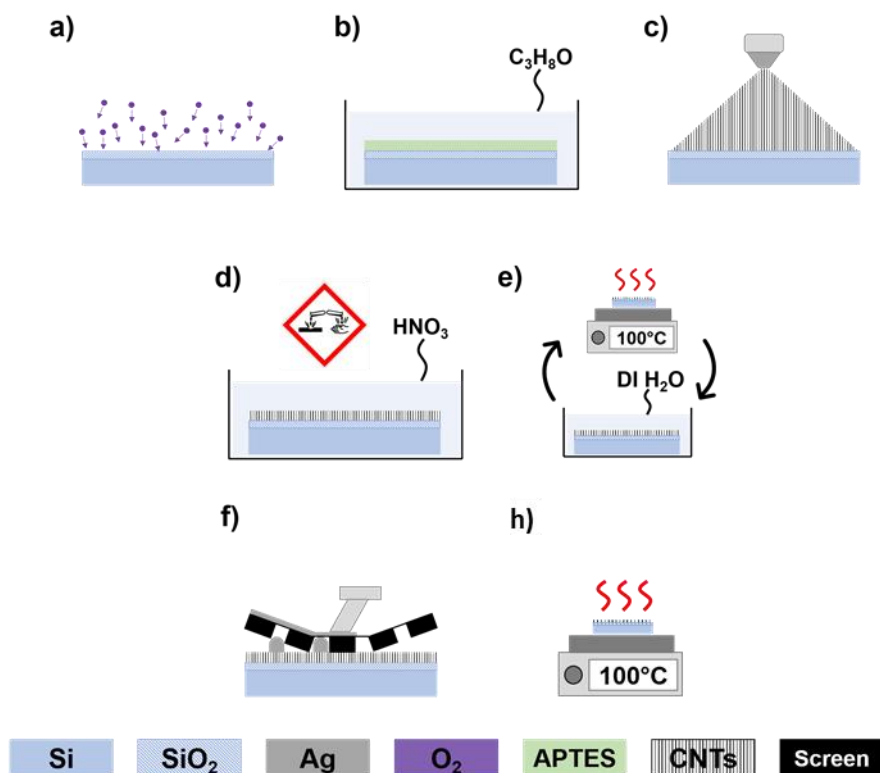
Figure 6-24 Schematic representation of the main fabrication steps we followed to fabricate gas sensors with screen printed Ag contacts. a) Oxygen Plasma Treatment: surface cleaning with oxygen plasma to reduce surface tension. b) APTES treatment: soaking in APTES/Isopropanol solution to enhance CNT adhesion on the wafer. c) Spray-coating: application of a random CNT thin-film on the wafer. d) Dispersant removal: soaking of the wafer in an acid bath for at least 12 h to remove the dispersant CMC. e) Drying step: successive cycle of drying the wafer at 100 °C for 15 min, soaking in DI water and drying again. f) Screen printing: Screen printing of Ag contact structure.

6.4.2 DC Characterization

To evaluate the quality of the CNT-TFTs patterned on one wafer we recorded transfer and output characteristics of each sensor with a Keithley 2636 sourcemeter. The 2636 allows measurement down to the 1 pA range. In preparation for the gas measurement, we fabricated a sample holder for 3-terminal characterization compatible with the gas chamber. A breadboard served as substrate and we mounted pin headers for external contacting. Two vertically adjustable probing arms were used to contact source and drain contacts on the gas sensor and simultaneously ensured a secure hold of the sensor on the sample holder. We installed a copper plate as seating and gate contact. A Peltier element was mounted beneath the copper plate to enable active recovery by heating the sample and desorb gas molecules form the CNT network. We surveyed the actual temperature with a Pt100. Dimensions and assembly of the sample holder were adjusted to the dimensions of a measurement

compartment of the gas setup. The resulting sample holder is schematically depicted in Figure 6-25.
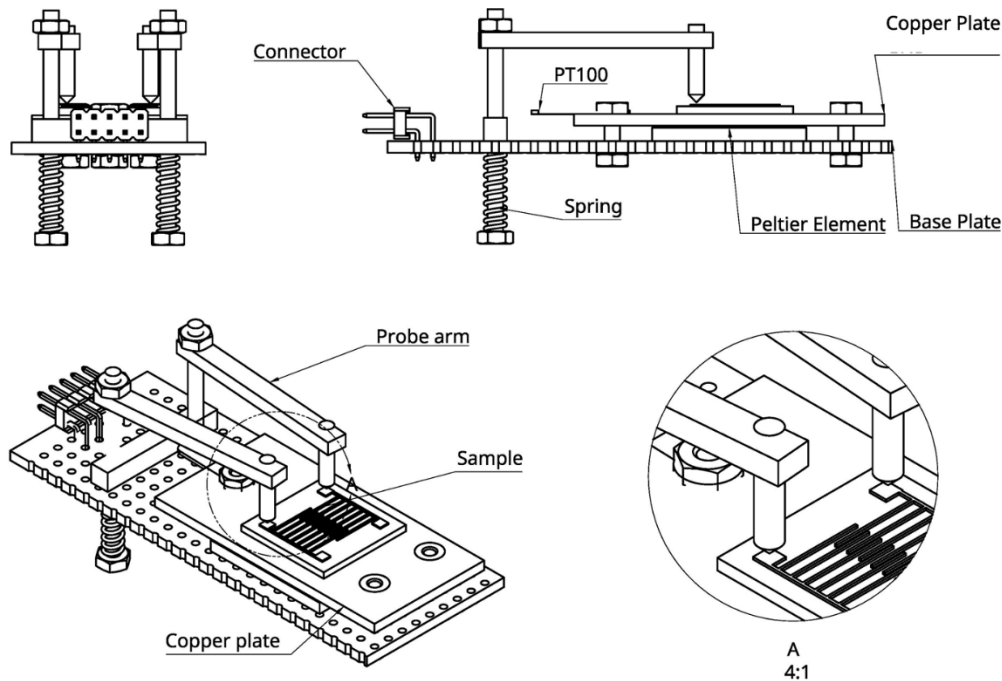
Figure 6-25 Technical drawing of the sample holder from different perspectives, designed for the gas measurement setup. Key elements are annotated in addition to a magnification at the contact point to the gas sensor.

To confirm the sensor functionality we placed the sensor on the sample holder and connected it to the Keithley 2636. We operated the Keithley 2636 via GPIB with a MATLAB script executed on a personal computer. The MATLAB script enabled recording the transfer and output characteristics of the sensor, by sourcing the voltage and sensing the current with the Keithley 2636. Independent of the measurement device, we collected the transfer data by sweeping the gate voltage from positive to negative voltages, with a step size of 0.1 V. The drain voltage was fixed to VDS = - 0.5 V and we recorded the resulting drain and gate current. Figure 6-26 exemplifies the transfer characteristic of a gas sensor recorded in ambient conditions in half logarithmic and linear scale. Drain and gate currents are displayed as absolute values. We smoothed the recorded drain and gate current with the 'smoothdata' command in MATLAB and a smoothing factor of 0.1. As smoothing method we decided for 'rloess', which is a robust quadratic regression, ideally suited for noisy data with outliers. With respect to Figure 6-26, the sensor clearly shows a gating effect: at positive gate voltages, the drain current is negligibly small and ranges around several pA and towards negative gate voltages the CNT thin-film starts conducting, resulting in an increasing drain currents
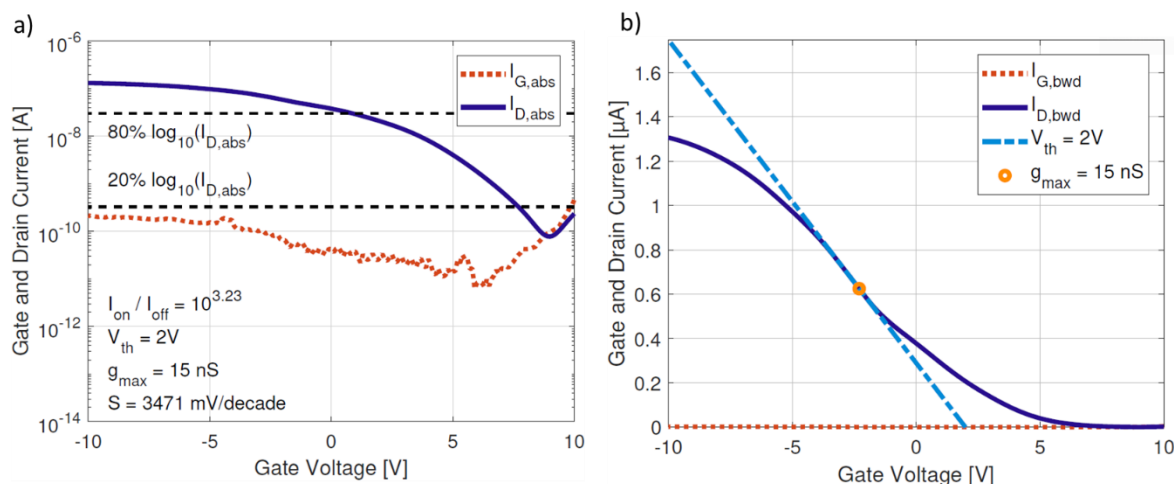
Figure 6-26 a) Half logarithmic representation of the transfer characteristic of a CNT-TFT in ambient conditions. The text box in the lower left corner displays different transistor characteristics, such as on-off ratio, threshold voltage, maximum transconductance and subthreshold slope. b) Linear representation of the transfer characteristic of a CNT-TFT in ambient conditions. The yellow circle indicates the point of maximum transconductance. The zero crossing of the tangent aligned at the point of maximum transconductance shows the threshold voltage.

From the recorded data, we determined different transistor characteristics, such as the on-off ratio I_{on}/I_{off}, the maximum transcsonductance g_{max}, the threshold voltage V_{th} and the subthreshold slope S, which are displayed in lower left corner of Figure 6-26. The on-off ratio was calculated by dividing the maximum drain current by the minimum drain current. We determined the maximum transconductance of the sensor by identifying the maximum gradient in the drain current data, which is depicted in Figure 6-26 as yellow circle. From the maximum transconductance we determined the threshold voltage graphically by aligning a tangent at the point of maximum transconductance. The zero crossing of the tangent indicates the threshold voltage. The tangent is depicted in Figure 6-26 as dashed, light blue line. Finally, we calculated the subthreshold slope between 20% and 80% of the maximum drain current in half-logarithmic representation.

To perform a gas measurement we placed one sensor on the sample holder and introduced it to the measurement compartment, which was then sealed hermetically. The measurement compartment was connected to a gas flow controller, which regulated the gas supply of carrier gas and test gas. We controlled the gas flow controller with a LabView script implemented on a personal computer. The LabView script enabled continuous measurements with successive cycles of gas supply and sensor recovery. The same software also controlled a Keithley 2602B system source meter, which triggered the Peltier element for a stable environmental temperature and surveyed the temperature recorded by the Pt 100. We adjusted the regular measurement temperature to 30 °C and increased it to 80 °C for

active recovery of the CNT-TFT. Figure 6-27 displays the experimental setup, schematically.
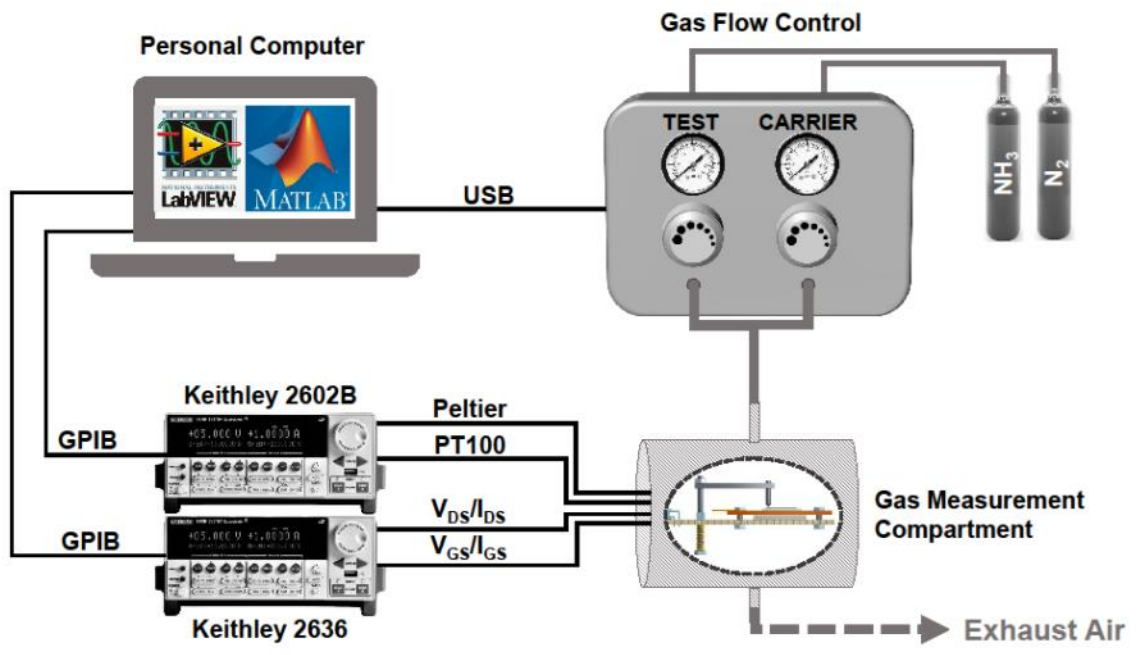
Figure 6-27 Schematic representation of the experimental setup we established for gas measurements consisting of: gas chamber, gas flow controller, source meters and a PC controlling the devices over a MATLab/ LabView interface.

In this work, we analyzed the response of the CNT-TFT on different concentrations of NH_3. The test gas was mixed with a carrier gas, to achieve the desired concentration, while maintaining a constant gas flux of 200 mL/min. Here, N_2 served as carrier gas. One measurement routine comprised of four consecutive cycles of the following measurement steps: 600 s standard measurement at 30 °C, 300 s of gas flow and 300 s of active recovery at 80 °C. In each cycle we altered the test gas concentration. Note that the test gas concentrations correspond to 10, 25, 50 and 100 ppm, respectively.

For the initial characterization, the samples were not exposed to NH_3 and were measured at 30 °C in N_2 atmosphere. Starting with the Au based contacts we performed experiments to select the optimal configuration of channel width, length and CNT layer number. Figure 6-28 displays transfer characteristic of three representative Au sensors with channel lengths of 100 μm, 200 μm and 500 μm at 3L. The table in Figure 6-28 summarizes key transistor characteristics. A first observation is the decreasing the on-off ratio with increasing channel length. While the transistors with 100 μm and 200 μm channel length exhibit a clear transition between the off and the on state, the gating effect of the 500 μm sensor is barely apparent. An explanation for this behavior is that the number CNTs forming a conductive paths between the electrodes diminishes for low network densities and increasing channel

length. As a result the maximum drain current across the channel is restricted and no longer modulated by the gate voltage.

A further observation is the shift of the threshold voltage towards larger gate voltages when comparing the 100 μm and 200 μm sensors, which results from the decreased on-current and thus a less steep slope of the drain current of the 200 μm transistor.

L_{ch} [μm]	100	200	500
I_{on} / W_{ch} [pA/mm]	262	130	1.22
I_{off} / W_{ch} [fA/mm]	156	822	131
I_{on} / I_{off}	$10^{2.23}$	$10^{2.2}$	$10^{0.97}$
V_{th} [V]	2	3.5	3.5
g_{max} / W_{ch} [pS/mm]	30	23	0.6
S [mV/dec]	3436	2992	6127
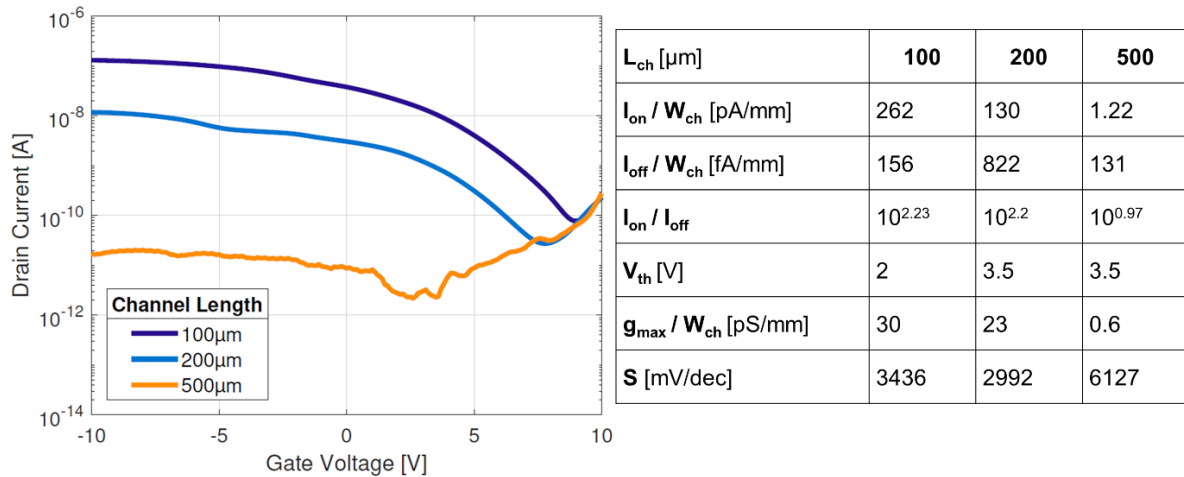
Figure 6-28 Plot of transfer characteristic of 3L Au sensors with channel lengths of 100 μm, 200 μm and 500 μm swept from 10 V to -10 V V_{GS} at a V_{DS} of - 0.5 V. Table displays transistor characteristics of 3L Au sensors with channel lengths of 100 μm, 200 μm and 500 μm.

Considering the subthreshold slope we would expect it to increase with increasing channel length, when comparing the transistors with 100 μm and 500 μm channel length. However, the subthreshold slope of the 200 μm sensor drops to 3003 mV/dec with regard to the 100 μm sensor. We assume this effect to occur due to the varied gate voltage range of -5 V to 10V to determine the 200μm transistor characteristics. From the maximum transconductance normalized with the channel width and a gate capacitance of 9.3 nF/cm^2, we extract a respective field effect mobility of 0.65 mm^2 V^{-1} s^{-1}, 0.1 mm^2 V^{-1} s^{-1} and 0.0065mm2 V^{-1} s^{-1} for the 100 μm, 200 μm and 500 μm transistors.

An identical experiment was performed for 4L and the results are presented in Figure 6-29. Clearly indicated is a decreasing gate voltage dependent switching with increasing channel length. While the transistors with 100 μm and 200 μm channel length exhibit a clear transition between the off and the on state, the gating effect of the 500 μm sensor is barely apparent. This effect is reflected in the on-off ratio, which calculates to $10^{3.8}$ and $10^{3.06}$ for the 100 μm and 200 μm transistors and declines to $10^{1.05}$ for the 500 μm. As previously explained we assume that the number CNTs forming conductive paths between the electrodes diminishes for low network densities and increasing channel length. As a result

the maximum drain current across the channel is restricted and is no longer modulated by the gate voltage.

L_{ch} [µm]	100	200	500
I_{on} / W_{ch} [pA/mm]	1690	592	11.7
I_{off} / W_{ch} [fA/mm]	266	511	1050
I_{on} / I_{off}	$10^{3.8}$	$10^{3.06}$	$10^{1.05}$
V_{th} [V]	-1.5	-1	2.5
g_{max} / W_{ch} [pS/mm]	$108 \cdot 10^3$	2621	1.4
S [mV/dec]	3391	3079	8714
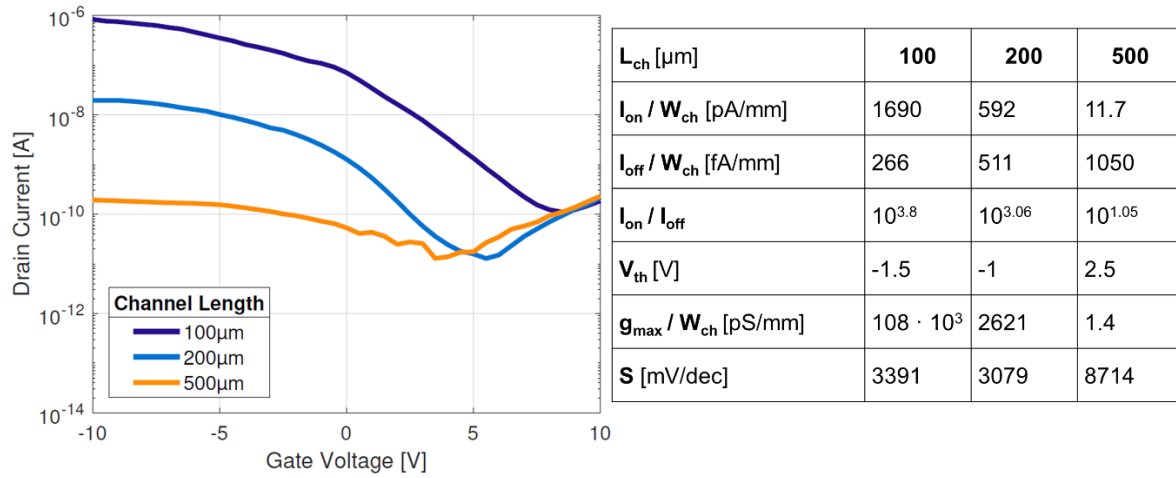
Figure 6-29 Plot of transfer characteristic of 4L Au sensors with channel lengths of 100 µm, 200 µm and 500 µm swept from 10V to -10V V_{GS} at a V_{DS} of -0.5V. Table displays transistor characteristics of 4L Au sensors with channel lengths of 100 µm, 200 µm and 500 µm.

A further observation is the faster transition of the transfer characteristic from the off- to the on-state with regard to the 200 µm sensor. Two consequences in the transistor characteristic reveal: the threshold voltage is shifted to the negative gate voltage regime and the subthreshold slope is reduced compared to transistors with 100 µm and 500 µm channel length. From the maximum transconductance normalized with the channel width and a gate capacitance of 11.2 nF/cm^2, we extract a respective field effect mobility of 3.9 mm^2 V^{-1} s^{-1}, 0.03 mm^2 V^{-1} s^{-1} and 0.01 mm^2 V^{-1} s^{-1} for the 100 µm, 200 µm and 500 µm transistors.

In the previous experiments, we discussed the performance of our fabricated 3L and 4L CNT-TFTs with Au electrodes. Here, we summarize the findings and compare results to find the optimum Au sensor layout for gas sensing. For both CNT densities, the transistor performance declined with increasing channel length. Especially the devices with 500 µm channel length barely exhibited a gating effect. We assume that both, 3L and 4L network densities lie far below the percolation threshold of the semiconducting nanotubes with regard to an increased contact distance of 500 µm. Overall, we observed an enhanced performance of the 4L devices compared to the 3L devices. For comparison, the most promising devices of both densities are depicted in Figure 6-30. The figure displays the transfer characteristic of a 3L and a four layer transistor with 100 µm channel length, as well as the transistor characteristics of both.
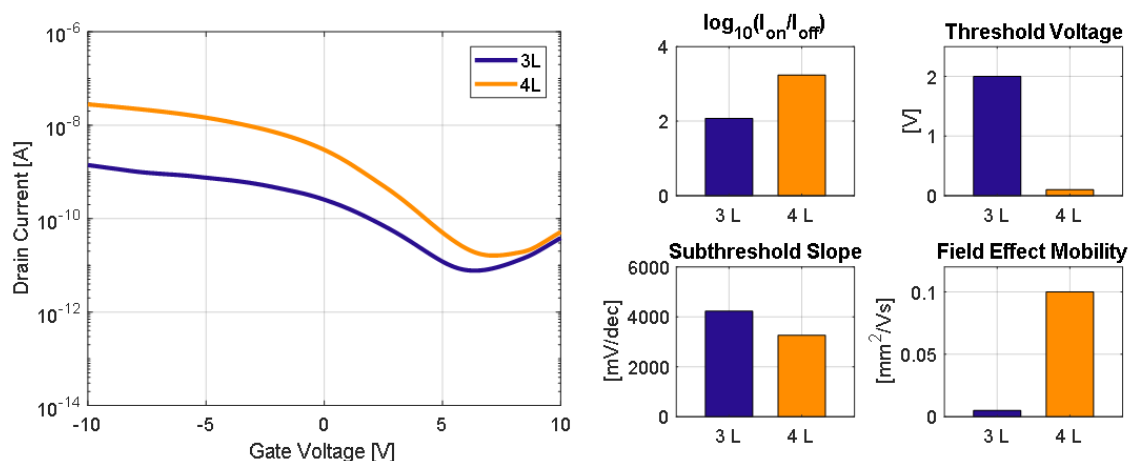
Figure 6-30 Plot of transfer characteristic of a 3L and 4L Au sensors with channel lengths of 100 μm swept from 10V to -10V V_{GS} at a V_{DS} of -0.5V. Sub-figures display transistor characteristics of a 3L and 4L Au sensors with channel lengths of 100 μm.

The I_{on} of the 4L transistor is significantly increased by one order of magnitude compared to the I_{on} of the 3L sensor, while the I_{off} stay in the same range. Normalized to the channel width the 3L and 4L devices exhibit a respective I_{on} of 1.85 pA/mm and 56.5 pA/mm and an I_{off} of 15.5 fA/mm and 32.7 fA/mm. The increased Ion also reflects in the on-off-ratio, which calculates to $10^{2.08}$ and $10^{3.24}$ for the 3L and 4L transistor. Another observation in the extracted Vth is that both transistors exhibit a normally-on characteristic. However, V_{th} is shifted towards lower V_{GS} for the 4L device, caused by a steeper slope and the increased I_{on}. Due to the steeper slope, the subthreshold slope of the 4L transistor reduces from 4224 mV/dec to 3263 mV/dec and enables a faster transition between the off- and the on-state. From maximum transconductance of 228 pS/mm and 5605 pS/mm and a gate capacitance of 9.3 nF/cm^2 and 11.2 nF/cm^2, the field effect mobility calculates to 0.005 mm2 V^{-1} s^{-1} and 0.1 mm2 V^{-1} s^{-1}, for the 3L and 4L transistor respectively. The main mechanism responsible for the enhanced performance of the 4L transistors is the optimum balance between the number of paths bridging the electrodes and a network density low enough to reduce the development of parasitic metallic paths. Therefore, the I_{on} increases which can be interpreted as decreasing network resistivity. Considering an equivalent circuit the Ion increase can be seen as additional resistance in parallel so that the total resistance is reduced.

For the Ag electrodes, a wider range of layers was tested as no previous experience was had with respect to possible device behavior. As previously mentioned we fabricated Ag sensors with 2L - 6L of CNT on below the IDE with channel lengths of 100 μm, 150 μm and 225 μm and finger widths of 100 μm and 150 μm. Note that from this point we abbreviate the different IDE layouts as 100-100, 100-150, 150-150 and 150-225, whereat the first number indicates the finger width and the second the channel length. Similarly to Au an array of experiments was performed to reduce the parameter space as to find the optimal starting

sensor for the gas measurement. Figure 6-31 summarizes the most promising results and compares them at differing xL.
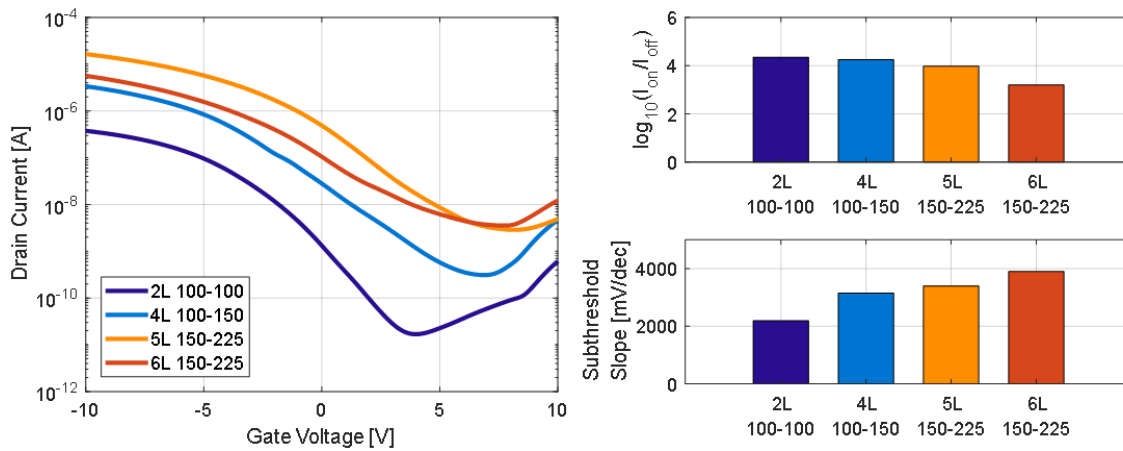
Figure 6-31 Plot of transfer characteristic of a 2L (100–100 µm), 4L (100-150 µm), 5L (150-225 µm) and 6L (150-225 µm) Ag sensors with corresponding channel lengths swept from 10V to -10V V_{GS} at a V_{DS} of -0.5V. Sub-figures display on-off ratios and subthreshold sweep values

Clearly visible is an increase of the I_{on} and the I_{off} with the ascending number of deposited CNT layers up to 5L with an outlier in the I_{on} of the 6L device. At lower densities the interval between I_{on} and I_{off} is more predominate, which also reflects in the on-off-ratio. Besides increasing I_{on}, adding extra CNT layers also has the undesired effect of increasing I_{off}. Since we fabricated the TFTs with 90% semiconducting CNTs the probability to introduce metallic tubes in the network increases with the ascending number of deposited layers. Metallic tubes in the thin-film reduce the resistivity and I_{off} increases. We achieved an optimal ratio of I_{on} and I_{off} with 2L deposited on the sensor. In order to evaluate the transition between off and on-state of the transistors, Figure 6-31 also displays the subthreshold slope. We find the optimum subthreshold slope with 2L deposited on the sensor. With increasing network density we observe the undesired effect of an increasing subthreshold slope, as a direct result from the increased I_{off}. Due to a high I_{off} and a saturating I_{on} the gradient flattens and the extracted subthreshold increases resulting in a poorer switching behavior.

Summarizing the optimal devices for Au was selected as 100 µm and 4L while for the Ag 100-100 µm and 2L was selected. Although somewhat surprising that the Ag sensors show higher current at 2L than 4L Au this has multiple explanations. One simple explanation is the slightly larger surface area (Ca 2.5x) however this would not result in an 10^1 increase in current. Another explanation is that Ag could in fact have a better band matching to CNTs than gold due to band bending [162].

6.4.3 Transistor Characteristic Gas Dependency

In the previous section, we found an optimum Au sensor layout at 100 μm channel length and 4L of CNTs deposited on the electrodes. To analyze the sensors response in a gas atmosphere we expose it to different concentrations of NH_3. As previously mentioned we performed four consecutive cycles of 600 s standard measurement at 30 °C and a N_2 carrier gas flow, followed by 300 s test gas flow of a certain concentration and finally 300 s active recovery at 80 °C. In each cycle, we increased the test gas concentration from ranging from 10ppm to 100ppm. To analyze the variation in the gating we recorded the transfer characteristic of the transistor every 300 s to analyze the performance. To better visualize the data the I_{on} and I_{off} for each measurement are plotted in Figure 6-32. The first observation is a significant decrease of I_{on} with increasing measurement duration of more than one order of magnitude.
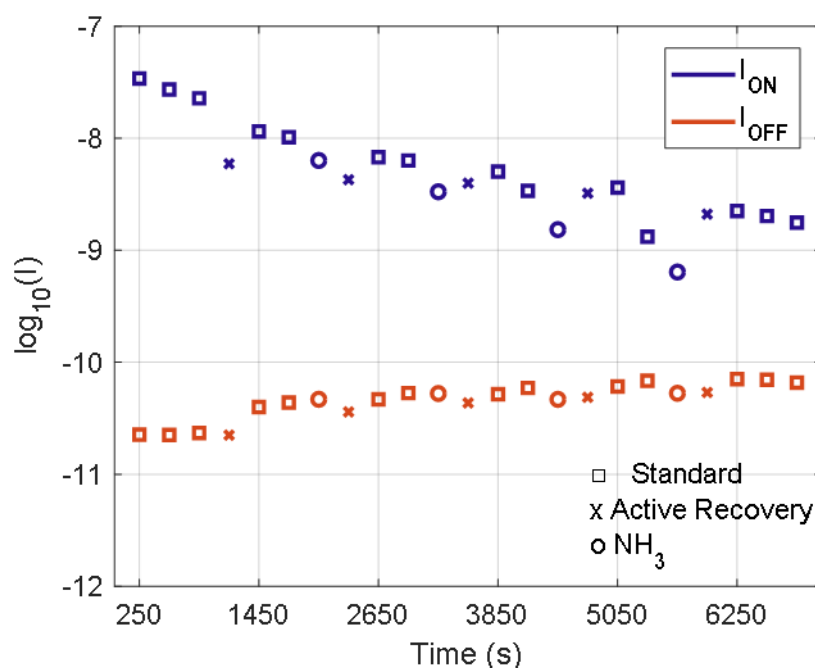
Figure 6-32 Half logarithmic plot representation of I_{on} (blue) and I_{off} (red) currents of the 4L Au transistor with 100 μm channel length with respect to the time of measurement. The various marked points represent different measuring conditions: square: 200 mL/min N_2 at 30°C. cross: 200 mL/min N_2 at 30°C. circle: mixture of N_2 and NH_3 increasing from 10ppm to 100ppm NH_3 (10, 25, 50 , 100 ppm)

The shift of the transfer curve with time indicates a reduction of the thin-film conductivity, caused by two effects: the desorption of O_2 and subsequent exchange with N_2, as well as the adsorption of NH_3. The first effect can be clarified considering the first three measuring points. I_{on} declines linearly with time, while the sensor is only exposed to a constant flux of

N_2 of 200 ml/min. As summarized the desorption of O_2 results in a decrease of the work function of the metal contacts, which causes a diminishing hole injection in the CNT network. Expanding on this theory, we assume that the due to the lack of O_2 in the gas compartment, O_2 molecules are slowly desorbed from the sensor caused by the imbalance of the adsorption-desorption rate in favor of desorption. N_2 molecules adhere to the O_2-free spaces on the sensor, which results in a decrease of the work function of the metal contacts and therefore a reduced thin-film conductivity. In addition to a carrier gas adsorption in the network, exposure to test gas might also affect the network conductivity, especially if the active recovery cannot entirely desorb the NH_3 molecules. Since NH_3 is an electron donor, physisorption to the sensor decreases the thin-film conductivity and induces a noticeable shift in the transfer curve towards lower V_{GS}. Figure 6-32 also reveals a significant drop of I_{on} with increasing test gas concentration, as well as an alteration of I_{on} as reaction to active recovery. In addition heating the sensor seems to restore Ion after gas exposure, although we cannot observe a full recovery to the initial magnitude. As mentioned above this behavior most likely occurs due the exchange of O_2 molecules present in ambient air and the carrier gas molecules N_2. In addition, NH_3 residues on the sensor may also be responsible for these results.

To discuss the effect of gas exposure and active recovery on the sensor performance, we investigate the transfer characteristics of the transistor recorded at these phases of measurement. As shown above we see a decrease of Ion, when exposing the sensor to NH_3 at all four concentrations, while I_{off} levels. In addition, the transfer curve shifts towards negative V_{GS}, which is more dominant at low concentrations. We observe the opposite effect at active recovery, where the curve shifts back towards positive V_{GS}. This is directly reflected in the threshold voltage, which shifts analogous with the shift of the transfer curve. Both, the shift of the curve, as well as the threshold voltage reveal an increased conductivity of the CNT network caused by heating. This is a typical observation in semiconducting materials, caused by the blurring of the Fermi-Dirac-distribution with increasing temperature and the resulting effect of an increased density of states in the HOMO for organic p-type semiconductors.

In order to determine the rate of change in the transfer characteristics, caused by the adsorption of NH_3, we analyzed the sensitivity of the device. Figure 6-33 shows the resulting sensitivities with respect to the NH_3 concentration. Noted are the absolute change and thus sensitivity regardless of the change being positive or negative.

Figure 6-33 Plot of sensitivity of the 4L Au transistor with 100 μm channel length regarding different transistor characteristics and with respect to different NH₃ concentrations.

Considering the on-off ratio, we observe a maximum sensitivity of 47.1% at 25 ppm NH_3 concentration. The sensitivity reduces to ca 42% for 10 and 50 ppm and reaches its minimum 100 ppm with 36.8%. Due to similar sensitivities at 10 and 50 ppm, a distinction of the test gas concentration is challenging, only considering the change in the on-off-ratio. It should be noted that due to the baseline drift of both I_{on} and I_{off} with increasing measurement time it is difficult to precisely isolate the change based solely on the exposure to NH With regard to the subthreshold slope the sensitivity ranges below 3% up to NH_3 concentrations of 50 ppm. Such low alterations probably occur due to measurement artefacts and are barely retractable to alterations in the ambient gas concentration. However, we record a peak of 11.9% at 100 ppm, which would enable the identification of increased NH_3 concentrations. Extracting the sensitivity based on the field effect mobility allows a good differentiation between low concentrations. While the sensitivity at 10 ppm calculates to 32.6%, ranges the sensitivity at 25 ppm around 47.4%. With further increasing NH_3 concentration the sensitivity appears to saturate at ca 60%. The sensitivity calculated from the threshold voltage allows no clear distinction between different test gases, since we observe similar values around 4.2% at 25 ppm and 50 ppm and around 5.5% at 10 ppm and 100 ppm.

In this section, we presented the results from exposing the optimum Au sensor with 4L and a channel of 100 μm to different concentrations of NH3. Besides a diminishing I_{on}, we also observed a shift of the transfer characteristic toward negative V_{GS} as a result from molecule

adsorption. We also determined the sensitivity of the sensor with respect to the concentration and different transistor characteristics. Although a distinction of the test gas concentrations considering the sensitivity of one characteristic is challenging, the combined information of all extracted sensitivities potentially allows distinguishing between different NH_3 concentrations.

Concerning the Ag sensor, we found an optimum Ag sensor layout at 100 μm channel length and finger width and 2L of CNTs deposited on the electrodes. The measuring protocol was identical to the Au sensor. I_{on} and I_{off} are plotted in Figure 6-34.
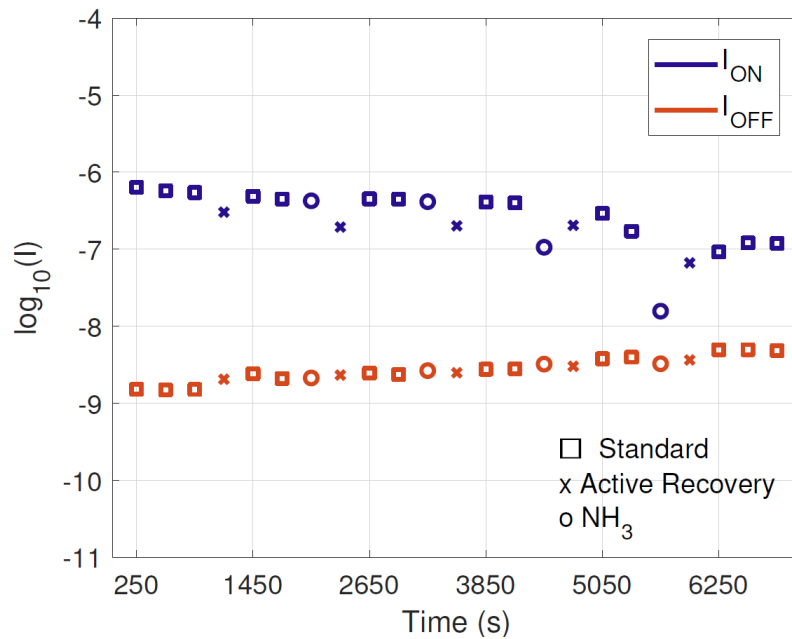
Figure 6-34 Half logarithmic plot representation of I_{on} (blue) and I_{off} (red) currents of the 2L Ag transistor with 100 μm channel length and finger width with respect to the time of measurement. The various marked points represent different measuring conditions: square: 200 mL/min N_2 at 30°C. cross: 200 mL/min N_2 at 30°C. circle: mixture of N_2 and NH_3 increasing from 10ppm to 100ppm NH_3 (10, 25, 50 , 100 ppm)

Similar to the Au sample a decrease of I_{on} can be observed with increasing measurement time as well as an increase in I_{off}, This effect is significantly smaller than for the Au sample as such the resulting sensitivity should give a better representation of the change due to gas exposure. Visible is decrease of Ion during active recovery, while I_{off} levels. In addition, the curve is shifted towards positive V_{GS} at 10 ppm and 25 ppm and towards decreasing V_{GS} at 50 ppm and 100 ppm. To discuss the effect of gas exposure and active recovery on the sensor performance, we investigate the transfer characteristics of the transistor recorded at these phases of measurement with the results plotted in Figure 6-35.
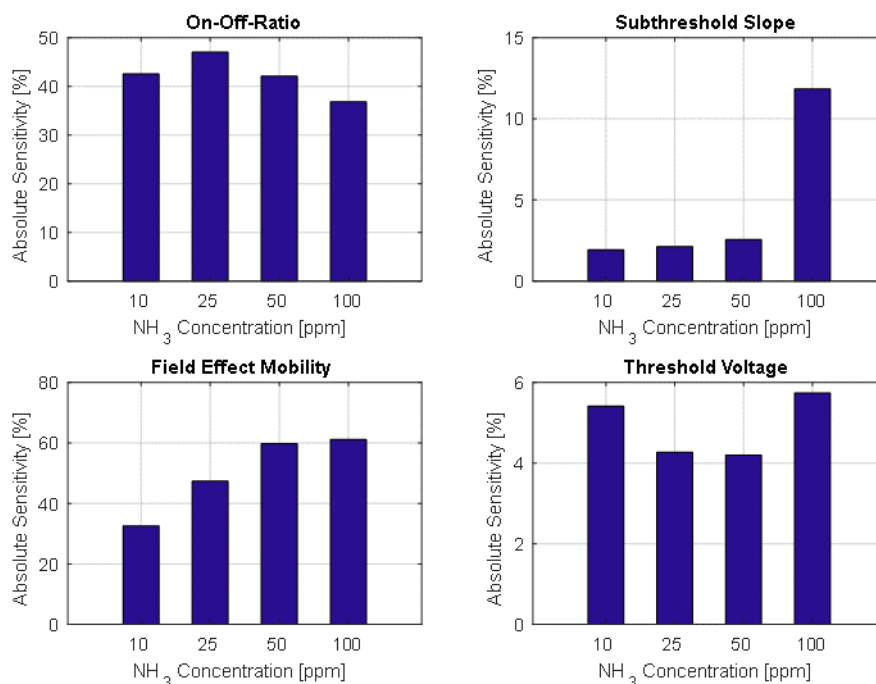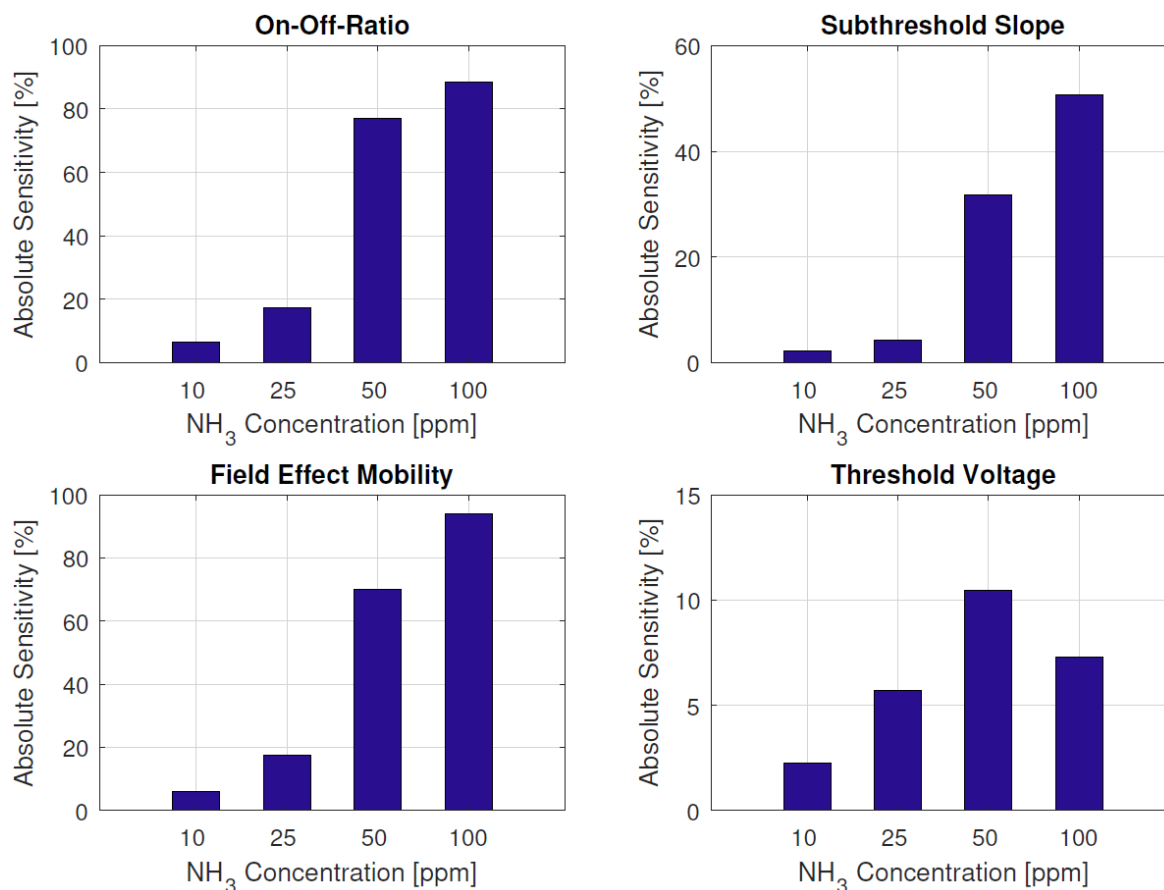
Figure 6-35 Plot of sensitivity of the 2L Ag transistor with 100 μm channel length and finger width regarding different transistor characteristics and with respect to different NH₃ concentrations.

Considering the on-off ratio we observe a maximum sensitivity of 88.4% at 100 ppm NH₃ concentration. The sensitivity reduces to 76.9% for 50 ppm and drops to 17.5% and 6.5% at 25 ppm and 10 ppm, respectively. With regard to the subthreshold slope the sensitivity ranges below 5% up to NH₃ concentrations of 50 ppm. Such low alterations probably occur due to measurement artefacts and are barely retractable to alterations in the ambient gas concentration. However, we record an exponential increase to 31.7% at 50 ppm an 50.7% at 100 ppm, which would enable the identification of increased NH3 concentrations. Extracting the sensitivity based on the field effect mobility allows a well differentiation of all concentrations. While the sensitivity at 10 ppm calculates to 5.9%, increases the sensitivity at 25 ppm to 17.6%. At 50 ppm notice an abrupt increase to 70.2%, which accelerates up to 94.1% for 100 ppm NH₃ concentration. The sensitivity calculated from the threshold voltage shows a linear increase from 2.2% to 10.45% between 10 ppm and 50 ppm with a significant drop to 7.3% at 100 ppm. As a result the sensitivity based on the threshold voltage is unsuited to discriminate between different gas concentrations. While at low concentrations a distinction of the transfer curves before and at the time of gas exposure is challenging, with increasing concentration the curves shift further apart. These findings suggest a good

distinction of the test gas concentration, even with one transistor characteristic, which could be further enhanced when considering all extracted characteristics.

6.4.4 Electrode Material Dependence

In order to compare the performance of the fabricated Au and Ag sensors we analyze two sensors with a similar layout. The Au sensor has a channel length of 100 µm and the Ag sensor a channel length and finger width of 100 µm and 150 µm, respectively. On both sensors we deposited 4L layers of CNTs. Figure 6-36 shows the resulting transfer and transistor characteristics of the Au and Ag sensor.
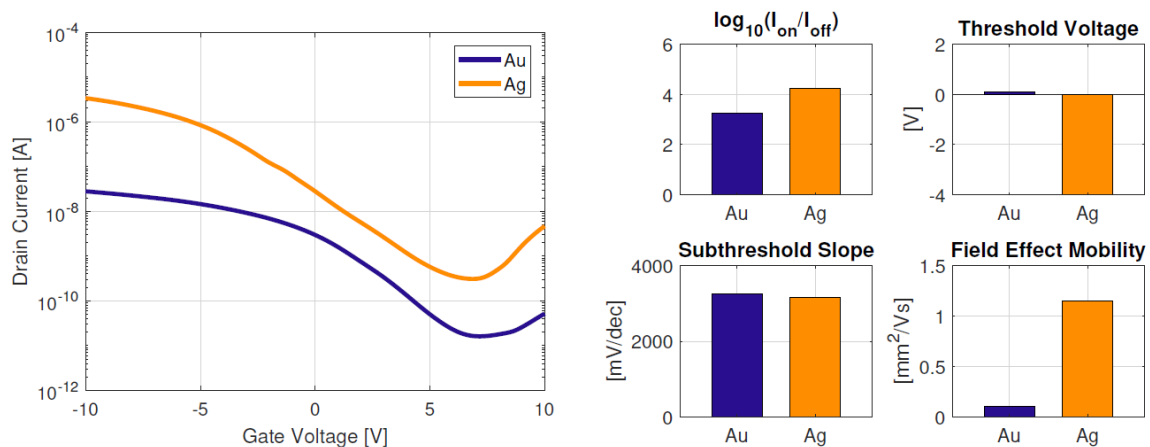
Figure 6-36 Plot of transfer characteristic comparing a 4L Au sensor with 100 µm channel length and a 4L Ag sensor with 100-150 IDE layout swept from 10V to -10V V_{GS} at -0.5V V_{DS}. The bar charts represent the extracted transistor characteristic of a 4L Au sensor (blue) with 100 µm channel length and a 4L Ag sensor (orange) with 100-150 IDE layout.

A first observation from Figure 6-36 is a shift of the transfer characteristic recorded with the Ag sensor toward increasing I_D. Moreover, the Ag transistor exhibits a ten times increased on-off-ratio of $10^{4.25}$ compared to the Au sensor with $10^{3.23}$. As previously discussed the recorded drain current in the linear and saturation regime is linearly dependent on the W/L -ratio as well as on the gate capacitance. Comparing the extracted gate capacitance of 8 nF/cm^2 and 11.2 nF/cm^2, and the calculated W/L -ratio of 1301 and 496 for the Ag and Au sensor, we notice an increase of the Ag sensor characteristics. Therefore, the increased I_D and on-off-ratio of the Ag sensors results probably from the increased sensor area of the device. This however was a limitation of the, at the time available printable structures.

In addition to the shift along the I_D-axis, we also observe a slight shift towards more negative V_{GS} of the Ag transfer characteristic. Most probably, the shift results from a decreased network conductivity. Adapting to [reffxx] a potential source is the influence of the decreased Ag work function, which ranges typically around 4.5 eV compared to the Au work

function, which ranges typically around 5.1 eV. The decreased work function of Ag supports the formation of Schottky barrier, due to the difference in the Fermi level of the CNTs and the metal work function. Moreover, we fabricated the devices in ambient conditions, which enables the adhesion of O_2 and H_2O molecules on the surface of the metals. This leads to the formation of surface dipole, which could further influence the hole injection barrier [163]. Both effects result in an increase of the hole injection barrier for the Ag contacts causing an overall reduced conductivity of the thin-film.

For a direct comparison, we compared the two sensors at 50 ppm NH_3. Figure 6-37 shows the transfer characteristics of both sensor layouts and compares the sensitivity with regard to the on-off ratio, the subthreshold slope, the maximum transconductance and the field effect mobility at 50 ppm NH_3 concentration.
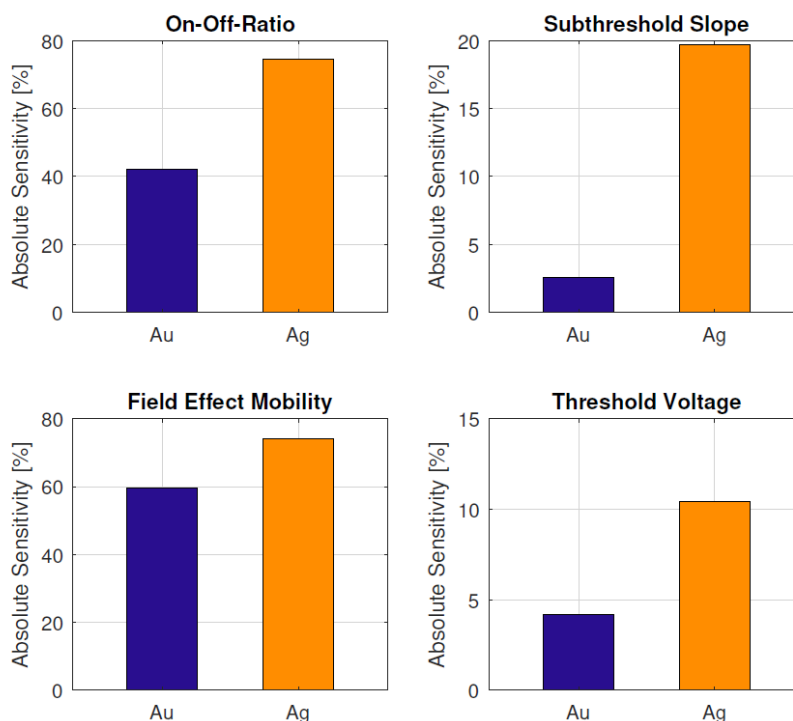
Figure 6-37 Comparison of sensitivity of 4L Au and 4L Ag sensor exposed to NH_3 regarding the on-off ratio, the subthreshold slope, the maximum transconductance and the field effect mobility at 50 ppm NH_3 concentration.

As displayed in Figure 6-37 the Au sensor exhibits a sensitivity with regard to the on-off ratio of 42.1%, with regard to the subthreshold slope of 2.6%, with regard to the field effect mobility of 59.7% and with regard to the threshold voltage of 4.2%. In contrast, the Ag sensor shows overall increases sensitivities of 74.5% with regard to the on-off ratio, 19.7% with regard to the subthreshold slope, 74.1% with regard to the field effect mobility and 10.45% with regard to the threshold voltage.

To sum up, in this section we compared the performance of two sensors fabricated with different electrode materials in ambient conditions as well as in gas atmosphere. Independent of the environmental conditions we found an overall enhanced performance of the Ag transistor. To investigate the actual distribution of the electrode material on the performance would require the fabrication of sensors with an identical layout and the same deposition technique to reduce unwanted factors.

6.5 Summary

In this chapter, we present the design and fabrication of CNT based gas sensors in both a resistive configuration as well as chemFET. Initially we describe the interaction between CNTs and gas molecules pertaining specifically to the electrical properties. We present what has currently been presented in literature as the possible mechanisms for interaction. The initial fabrication focuses on the resistive devices. We present a fabrication process for the realization of IDES structures with a CNT active layer. Due to the significant research present, we choose to investigate the longevity of our sensors as to prove their feasibility. Here we showed that after an initial decrease in performance the sensor stabilizes. The initial decrease in performance in attributed to the absorption of non-test molecules as such blocking binding sites. Regardless of this, the sensor maintains functionality even after the extended period of four years. As a further improvement to the already presented process we attempted to fabricate a full CNT sensor. This has advantages in both reduced cost as well as functionality providing the possibility of semitransparent sensors. We investigated various architectures with a focus on finger spacing. Intermitting the transition to chemFETs, we tested a newly introduced writing technique by fabricating flexible CNT based sensors with the aid of a roller ball. The sensors displayed comparable sensitives to the previously fabricated devices. This is a testament to the ease of integrabillity of our developed processes and CNT solutions. The second part of the chapter has been devoted to the fabrication of chemFETs. For this step, we merged the previous experience with TFTs and the knowledge of CNT gas sensors. We investigated various architectures to identify an optimum. Developing both a measurement protocol as well as a data analysis, we investigated the transistor performance in a controlled atmosphere while exposed to various concentrations of ammonia. Extracting the response from transistor characteristics such as on-off ratio, threshold voltage, transconductance and sub threshold swing. In terms of magnitude the field effect mobility had the largest response surpassing the previously recorded values for the resistive sensors. The final experiment performed was to reproduce the fabrication with silver instead of gold electrodes as it has been shown in literature that this could provide a better interface between active layer and electrodes. With these devices we achieved even higher responses and a significantly better distinction between the varying concentrations.

This part of the work was done as a proof of concept and needs to be significantly expanded, however it does provide a potential solution to the selectivity problem that CNT sensors are known to have.

Chapter 7

Conclusion and Outlook

The main goal of this thesis was to develop processing techniques for the development and fabrication of spray deposited CNT based devices, in particular TFTs and gas sensors. This task was segmented into various steps: the development of a spray deposition process that delivers a stable framework that is also easy to integrate into other existing processes, the definition and functionalization of our deposited films, specifically by means of laser ablation and modification, the development of CNT TFTs and CNT based gas sensors.

In order to better understand the framework into which this thesis fits, we gave a brief introduction into CNTs, their discovery, synthesis and purification. We continue by highlighting the key phenomena pertaining to CNTs and the source of their uniqueness as well as their electrical and physical properties. Additionally we present a short overview of state of the art devices presented in literature with a focus on CNT TFTs and gas sensors. We described the main printing techniques used in this thesis as well as where these have been successfully applied in the printed electronics world.

The first experimental chapter of the thesis laid out the framework for the spray deposition of CNT films. The initial challenge was dispersing the CNTs into a stable solution. For safety and environmental considerations, we chose water as our solvent. In order to aid dispersion we made use of dispersants CMC and SDS as to create both stable solutions as well as homogeneous dispersions. Although CMC solution offer a better dispersion, CMC is significantly more difficult to remove and requires the use of nitric acid while SDS can be removed with the aid of water. The tradeoff between the two dispersant was shown in terms of bundles and as such efforts were made to improve the SDS based solution to reach comparable dispersions for both. In order to guarantee a pristine film post deposition free of

unwanted dispersant, we investigated our processes with the aid of field enhanced scanning electron microscopy, X-ray photoelectron spectroscopy and Raman spectroscopy. Doing so allowed us to make measurement-backed statements as to the complete removal of dispersants. In addition we also showed that annealing treatments allow for the desorption of unwanted gas molecules adsorbed during the post deposition treatment are desorbed.

In the subsequent chapter, we addressed the drawbacks of the coated random network with the aid of femtosecond laser ablation and modification. We started the investigation by explaining the interaction between laser and CNT film while understanding the two operation modes of single and multi-pulse operation. Doing so revealed a differing behavior to for example SiO_2 namely an increase in energy required with subsequent pulses rather than a decrease. In addition we were able to define operating regimes: a) Visible modification of the CNT network without ablation. (b) ablation of the CNT network. (c) substrate damage. Following this we showed that it is possible to galvanically separate films as such allowing for the use of this technique as a paterning tool. In addition to simple separation we investigated the effects of polarized laser light. Here we displayed the capability to ablate CNT based on orientation with a 90° corelation to the polarization of the laser light. This is due to the reduced absorption of the light when mis alligned to the incident laser. We characterized the efficency of this method both electrically with regard to the resistance of the remaining film as well as optically with the aid of SEM images. Here we perfored an angle analysis on the remaining films showing the peak values of the distributions at 0° and 90° for the perpendicular polarization and perpendicular polarization respectively. The standard deviation from peak are 23° for the perpendicular and 24° for the parallel polarization. This is a proof of concept for a post deposition alignment technique previously reserved to directed chemical vapor deposition growth, an expensive and complex process. Finally, we also introduced the possibility that CNTs could be ablated based on their electrical properties as these are correlated to the absorption spectra as such metallic CNTs would have a lower ablation threshold (40%) at 550 nm for example in contrast to semiconducting CNTs. This method requires further investigation but gives promise of a technique that could be used as an alternative for very expensive separation technique that lead to exponentially higher material prices.

In the first device chapter (5), we introduced our process for the fabrication of randomly aligned CNT TFTs. Initially a short overview of general organic TFTs was given as well as the basic charge transport mechanism. Following we showed the specifics pertaining to CNT TFTs. We introduced I-V characteristics for OTFTs and key characteristics defining figure of merits such as field effect mobility, transconductance and subthreshold swing. Following the theoretical aspects, we introduced our fabrication protocol for CNT TFTs. We investigated the homogeneity and reproducibility of our process. Showing both great yields as well as a thin deviation on the wafer scale. For a better understanding, we investigated the

device performance dependency on CNT density with the corresponding figure of merits, in the process gaining a better understanding of the device performance correlation to increasing CNT densities. In correspondence with the developed SDS ink in chapter 3, we repeated the investigation to display its efficiency as an alternative to the CMC process that requires an acid treatment post deposition. Although not reaching the performance of CMC based process, the SDS process provides an alternative for more sensitive substrates. Due to the modularity of our process it allowed us to integrate it into an existing process and realize a flexible CMOS configuration with the CNT TFT as the p-type and IGZO as the n-type. With this configuration we fabricated common logic gates such as NOT and NAND. We investigated the system in a flexible configuration showing great mechanical stability and reliability. In contrast to previous works, we managed to reduce both the hysteresis behavior of CNT TFT as well as reliability. Finally, we fabricated a flexible common source amplifier with, at the time the highest gain (a peak value G = 28.7 dB) for flexible complementary amplifiers.

In the final device chapter we presented the design and fabrication of CNT based gas sensors in both a resistive configuration as well as chemFET configuration. Initially we described the interaction between CNTs and gas molecules pertaining specifically to the electrical properties. We showed what had previously been presented in literature as the possible mechanisms for interaction. The initial fabrication focused on the resistive devices. We presented a fabrication process for the realization of IDES structures with a CNT active layer. Due to the significant research present, we choose to investigate the longevity of our sensors as to prove their feasibility. Here we showed that after an initial decrease in performance the sensor stabilized. The initial decrease in performance is attributed to the absorption of non-test molecules, as such blocking binding sites. Regardless of this, the sensor maintained functionality even after the extended period of four years. As a further improvement to the already presented process, we attempted to fabricate a full CNT sensor. This has advantages in both reduced cost as well as functionality providing the possibility of semitransparent sensors. We investigated various architectures with a focus on finger spacing. Intermitting the transition to chemFETs, we tested a newly introduced writing technique by fabricating flexible CNT based sensors with the aid of a roller ball. The sensors displayed comparable sensitives to the previously fabricated devices. This is a testament to the ease of integrabillity of our developed processes and CNT solutions. The second part of the chapter was devoted to the fabrication of chemFETs. For this step, we merged the previous experience with TFTs and the knowledge of CNT gas sensors. We investigated various architectures to identify an optimum. Developing both a measurement protocol as well as data analysis, we investigated the transistor performance in a controlled atmosphere while exposed to various concentrations of ammonia. Extracting the response from transistor characteristics such as on-off ratio, threshold voltage, transconductance and sub threshold swing. In terms of magnitude the field effect mobility had the largest response (62% at 100

ppm) matching the previously recorded values for the resistive sensors. The final experiment performed was to reproduce the fabrication with silver instead of gold electrodes as it has been shown in literature that this could provide a better interface between active layer and electrodes. With these devices, we achieved even higher responses (75% at 100ppm) and a significantly better distinction between the varying concentrations. This part of the work was done as a proof of concept and needs to be significantly expanded, however it does provide a potential solution to the selectivity problem that CNT sensors are known to have.

Concluding, stable processes have been presented for the fabrication of both CNT TFTs and well as for the gas sensors, both resistive and TFTs, based on spray deposited random CNT networks. As is the case, each investigation has given rise to further questions and possible investigations, however this thesis should hopefully display the wide possibilities that spray coated CNT devices can offer especially with regards to possible integration into other existing processes.

Bibliography

[1]   M. Berggren, D. Nilsson, and N. D. Robinson, "Organic materials for printed electronics," *Nat. Mater.*, vol. 6, p. 3, Jan. 2007.

[2]   S. D. Ogier *et al.*, "Uniform, high performance, solution processed organic thin-film transistors integrated in 1 MHz frequency ring oscillators," *Org. Electron.*, vol. 54, pp. 40–47, 2018.

[3]   D. Choi, J.-S. Yeo, H.-I. Joh, and S. Lee, "Carbon Nanosheet from Polyethylene Thin Film as a Transparent Conducting Film: 'Upcycling' of Waste to Organic Photovoltaics Application," *ACS Sustain. Chem. Eng.*, vol. 6, no. 9, pp. 12463–12470, Sep. 2018.

[4]   N. Wang, A. Yang, Y. Fu, Y. Li, and F. Yan, "Functionalized Organic Thin Film Transistors for Biosensing," *Acc. Chem. Res.*, vol. 52, no. 2, pp. 277–287, Feb. 2019.

[5]   F. Schedin *et al.*, "Detection of individual gas molecules adsorbed on graphene," *Nat. Mater.*, vol. 6, no. 9, pp. 652–655, 2007.

[6]   I. Ierides, A. Zampetti, and F. Cacialli, "The resurgence of organic photovoltaics," *Curr. Opin. Green Sustain. Chem.*, vol. 17, pp. 15–20, 2019.

[7]   M. Biele, C. Montenegro Benavides, J. Hürdler, S. F. Tedde, C. J. Brabec, and O. Schmidt, "Spray-Coated Organic Photodetectors and Image Sensors with Silicon-Like Performance," *Adv. Mater. Technol.*, vol. 4, no. 1, p. 1800158, Jan. 2019.

[8]   C. Girotto, B. P. Rand, J. Genoe, and P. Heremans, "Exploring spray coating as a deposition technique for the fabrication of solution-processed solar cells," *Sol. energy Mater. Sol. cells*, vol. 93, no. 4, pp. 454–458, 2009.

[9]   G. Susanna, L. Salamandra, T. M. Brown, A. Di Carlo, F. Brunetti, and A. Reale, "Airbrush spray-coating of polymer bulk-heterojunction solar cells," *Sol. Energy Mater. Sol. Cells*, vol. 95, no. 7, pp. 1775–1778, 2011.

[10]   A. Reale *et al.*, "Spray Coating for Polymer Solar Cells: An Up-to-Date Overview," *Energy Technol.*, vol. 3, no. 4, pp. 385–406, 2015.

[11]   F. Aziz and A. F. Ismail, "Spray coating methods for polymer solar cells fabrication: A review," *Mater. Sci. Semicond. Process.*, vol. 39, pp. 416–425, 2015.

[12]   S. F. Tedde, J. Kern, T. Sterzl, J. Fürst, P. Lugli, and O. Hayden, "Fully Spray Coated Organic Photodiodes," *Nano Lett.*, vol. 9, no. 3, pp. 980–983, Mar. 2009.

[13]   M. Eslamian, "Spray-on thin film PV solar cells: advances, potentials and challenges," *Coatings*, vol. 4, no. 1, pp. 60–84, 2014.

[14]   Y.-J. Noh, S.-S. Kim, T.-W. Kim, and S.-I. Na, "Cost-effective ITO-free organic solar cells with silver nanowire–PEDOT: PSS composite electrodes via a one-step spray deposition method," *Sol. Energy Mater. Sol. Cells*, vol. 120, pp. 226–230, 2014.

[15]   S. Iijima, "Helical microtubules of graphitic carbon," *Nature*, vol. 354, no. 6348, pp. 56–58, 1991.

[16]   R. Saito, M. Fujita, G. Dresselhaus, and M. S. Dresselhaus, "Electronic structure of chiral graphene tubules," *Appl. Phys. Lett.*, vol. 60, no. 18, 1992.

[17]   P. M. Ajayan, "Nanotubes from Carbon," *Chem. Rev.*, vol. 99, no. 7, pp. 1787–1800, 1999.

[18]   B. Bhushan, *Handbook Springer of Nanotechnology*. 2010.

[19]   C. Schouml;nenberger and L. Forró, "Multiwall carbon nanotubes," *Phys. World*, vol. 13, no. 6, pp. 37–42, 2015.

[20]   S. Iijima and T. Ichihashi, "Single-shell carbon nanotubes of 1-nm diameter," *Nature*, 1993.

[21]   T. W. Odom, J. L. Huang, P. Kim, and C. M. Lieber, "Atomic structure and electronic properties of single-walled carbon nanotubes," *Nature*, vol. 391, no. 6662, pp. 62–64, 1998.

[22]   M. S. Dresselhaus, G. Dresselhaus, and R. Saito, "Physics of carbon nanotubes," *Carbon N. Y.*, vol. 33, no. 7, pp. 883–891, 1995.

[23]   C. Journet and P. Bernier, "Production of carbon nanotubes," *Appl. Phys. A Mater. Sci. Process.*, vol. 67, no. 1, pp. 1–9, 1998.

[24]   M. Kumar and Y. Ando, "Chemical vapor deposition of carbon nanotubes: a review on growth mechanism and mass production," *J. Nanosci. Nanotechnol.*, vol. 10, no. 6, pp. 3739–3758, 2010.

[25]   P. J. F. Harris and P. J. F. Harris, *Carbon nanotube science: synthesis, properties and applications*. Cambridge university press, 2009.

[26]   G. Zhong, T. Iwasaki, J. Robertson, and H. Kawarada, "Growth kinetics of 0.5 cm vertically aligned single-walled carbon nanotubes," *J. Phys. Chem. B*, vol. 111, no. 8, pp. 1907–1910, 2007.

[27]   K. Hasegawa and S. Noda, "Millimeter-tall single-walled carbon nanotubes rapidly grown with and without water," *ACS Nano*, vol. 5, no. 2, pp. 975–984, 2011.

[28]   A. Aqel, K. M. M. A. El-Nour, R. A. A. Ammar, and A. Al-Warthan, "Carbon nanotubes, science and technology part (I) structure, synthesis and characterisation," *Arab. J. Chem.*, vol. 5, no. 1, pp. 1–23, 2012.

[29]   J. Tersoff and R. S. Ruoff, "Structural properties of a carbon-nanotube crystal," *Phys. Rev. Lett.*, vol. 73, no. 5, p. 676, 1994.

[30]   J. M. Benoit, J. P. Buisson, O. Chauvet, C. Godon, and S. Lefrant, "Low-frequency Raman studies of multiwalled carbon nanotubes: experiments and theory," *Phys. Rev. B*, vol. 66, no. 7, p. 73417, 2002.

[31] B. K. Kaushik and M. K. Majumder, "Carbon nanotube based VLSI interconnects: Analysis and design," *SpringerBriefs Appl. Sci. Technol.*, no. 9788132220466, pp. i–iv, 2015.

[32] J. H. Lehman, M. Terrones, E. Mansfield, K. E. Hurst, and V. Meunier, "Evaluating the characteristics of multiwall carbon nanotubes," *Carbon N. Y.*, vol. 49, no. 8, pp. 2581–2602, 2011.

[33] M. Meyyappan, *Carbon nanotubes: science and applications*. CRC press, 2004.

[34] M. S. Dresselhaus, G. Dresselhaus, and P. C. Eklund, *Science of fullerenes and carbon nanotubes: their properties and applications*. Elsevier, 1996.

[35] A. Lekawa-Raus, J. Patmore, L. Kurzepa, J. Bulmer, and K. Koziol, "Electrical properties of carbon nanotube based fibers and their future use in electrical wiring," *Adv. Funct. Mater.*, vol. 24, no. 24, pp. 3661–3682, 2014.

[36] Y. Zhou, S. Sreekala, P. M. Ajayan, and S. K. Nayak, "Resistance of copper nanowires and comparison with carbon nanotube bundles for interconnect applications using first principles calculations," *J. Phys. Condens. Matter*, vol. 20, no. 9, 2008.

[37] R. Martel, T. Schmidt, H. R. Shea, T. Hertel, and P. Avouris, "Single- and multi-wall carbon nanotube field-effect transistors," *Appl. Phys. Lett.*, vol. 73, no. 17, pp. 2447–2449, 1998.

[38] T. Dürkop, S. a. Getty, E. Cobas, and M. S. Fuhrer, "Extraordinary Mobility in Semiconducting Carbon Nanotubes," *Nano Lett.*, vol. 4, no. 1, pp. 35–39, Jan. 2004.

[39] A. Javey *et al.*, "High-Field Quasiballistic Transport in Short Carbon Nanotubes," *Phys. Rev. Lett.*, vol. 92, no. 10, pp. 10–13, 2004.

[40] P. Avouris, "Carbon nanotube electronics," *Chem. Phys.*, vol. 281, no. 2–3, pp. 429–445, Aug. 2002.

[41] A. Nomura, K. Ito, and Y. Kubo, "CNT Sheet Air Electrode for the Development of Ultra-High Cell Capacity in Lithium-Air Batteries," *Sci. Rep.*, vol. 7, p. 45596, 2017.

[42] S. G. Mahajan *et al.*, "Sustainable power sources based on high efficiency thermopower wave devices," *Energy Environ. Sci.*, vol. 9, no. 4, pp. 1290–1298, 2016.

[43] H. Pan, J. Li, and Y. Feng, "Carbon nanotubes for supercapacitor," *Nanoscale Res. Lett.*, vol. 5, no. 3, p. 654, 2010.

[44] S. J. Tans, A. R. M. Verschueren, and C. Dekker, "Room-temperature transistor based on a single carbon nanotube," *Nature*, vol. 393, no. 6680, pp. 49–52, May 1998.

[45] P. L. McEuen, M. Bockrath, D. H. Cobden, Y.-G. Yoon, and S. G. Louie, "Disorder, pseudospins, and backscattering in carbon nanotubes," *Phys. Rev. Lett.*, vol. 83, no. 24, p. 5098, 1999.

[46] P. L. McEuen and J.-Y. Park, "Electron Transport in Single-Walled Carbon Nanotubes," *MRS Bull.*, vol. 29, no. 04, pp. 272–275, 2004.

[47] E. S. Snow, P. M. Campbell, M. G. Ancona, and J. P. Novak, "High-mobility carbon-nanotube thin-film transistors on a polymeric substrate," *Appl. Phys. Lett.*, vol. 86, no. 3, pp. 1–3, 2005.

[48]   A. Mousavi, P. Lamberti, V. Tucci, and V. Wagner, "Feasible industrial fabrication of thin film transistor based on randomized network of single walled carbon nanotubes," *ASMC (Advanced Semicond. Manuf. Conf. Proc.*, pp. 18–23, 2013.

[49]   J. Kong *et al.*, "Nanotube Molecular Wires as Chemical Sensors Nanotube Molecular Chemical Sensors Wires as," *Adv. Sci.*, vol. 287, no. 5453, pp. 622–625, 2010.

[50]   A. Abdelhalim, F. Loghin, M. Winkler, C. Zeiser, A. Abdellah, and P. Lugli, "Carbon nanotube based gas sensor arrays on rigid and flexible substrates," *2015 Ieee Sensors*, pp. 1–4, 2015.

[51]   J. Zhao, A. Buldum, J. Han, and J. P. Lu, "Gas molecule adsorption in carbon nanotubes and nanotube bundles," *Nanotechnology*, vol. 13, no. 2, pp. 195–200, 2002.

[52]   X. Cui, M. Freitag, R. Martel, L. Brus, and P. Avouris, "Controlling energy-level alignments at carbon nanotube/Au contacts," *Nano Lett.*, vol. 3, no. 6, pp. 783–787, 2003.

[53]   J. P. Novak, E. S. Snow, E. J. Houser, D. Park, J. L. Stepnowski, and R. A. McGill, "Nerve agent detection using networks of single-walled carbon nanotubes," *Appl. Phys. Lett.*, vol. 83, no. 19, pp. 4026–4028, 2003.

[54]   P. R. Mudimela *et al.*, "Single-Walled Carbon Nanotube Network Field Effect Transistor as a Humidity Sensor," *J. Sensors*, vol. 2012, pp. 1–7, 2012.

[55]   E. S. Snow, J. P. Novak, P. M. Campbell, and D. Park, "Random networks of carbon nanotubes as an electronic material," *Appl. Phys. Lett.*, vol. 82, no. 13, pp. 2145–2147, 2003.

[56]   A. Star, V. Joshi, S. Skarupo, D. Thomas, and J. C. P. Gabriel, "Gas sensor array based on metal-decorated carbon nanotubes," *J. Phys. Chem. B*, vol. 110, no. 42, pp. 21014–21020, 2006.

[57]   M. W. Rowell *et al.*, "Organic solar cells with carbon nanotube network electrodes," *Appl. Phys. Lett.*, vol. 88, no. 23, pp. 2–5, 2006.

[58]   C. M. Aguirre, S. Auvray, S. Pigeon, R. Izquierdo, P. Desjardins, and R. Martel, "Carbon nanotube sheets as electrodes in organic light-emitting diodes," *Appl. Phys. Lett.*, vol. 88, no. 18, pp. 18–21, 2006.

[59]   D. B. Hall, P. Underhill, and J. M. Torkelson, "Spin coating of thin and ultrathin polymer films," *Polym. Eng. Sci.*, vol. 38, no. 12, pp. 2039–2045, 1998.

[60]   C. J. Lawrence, "The mechanics of spin coating of polymer films," *Phys. Fluids*, vol. 31, no. 10, pp. 2786–2795, 1988.

[61]   R. K. Yonkoski and D. S. Soane, "Model for spin coating in microelectronic applications," *J. Appl. Phys.*, vol. 72, no. 2, pp. 725–740, 1992.

[62]   B. J. Norris, J. Anderson, J. F. Wager, and D. A. Keszler, "Spin-coated zinc oxide transparent transistors," *J. Phys. D. Appl. Phys.*, vol. 36, no. 20, 2003.

[63]   C. C. Chang, C. L. Pai, W. C. Chen, and S. A. Jenekhe, "Spin coating of conjugated polymers for electronic and optoelectronic applications," *Thin Solid Films*, vol. 479, no. 1–2, pp. 254–260, 2005.

[64]   D. E. Bornside, C. W. Macosko, and L. E. Scriven, "Spin coating: One-dimensional model,"

J. Appl. Phys., vol. 66, no. 11, pp. 5185–5193, 1989.

[65]   W. W. Flack, D. S. Soong, A. T. Bell, and D. W. Hess, "A mathematical model for spin coating of polymer resists," *J. Appl. Phys.*, vol. 56, no. 4, pp. 1199–1206, 1984.

[66]   A. K. K. Kyaw, X. W. Sun, C. Y. Jiang, G. Q. Lo, D. W. Zhao, and D. L. Kwong, "An inverted organic solar cell employing a sol-gel derived ZnO electron selective layer and thermal evaporated MoO 3 hole selective layer," *Appl. Phys. Lett.*, vol. 93, no. 22, p. 221107, 2008.

[67]   N. Miyata, T. Suzuki, and R. Ohyama, "Physical properties of evaporated molybdenum oxide films," *Thin Solid Films*, vol. 281, pp. 218–222, 1996.

[68]   Y. Yu *et al.*, "Thermally evaporated methylammonium tin triiodide thin films for lead-free perovskite solar cell fabrication," *RSC Adv.*, vol. 6, no. 93, pp. 90248–90254, 2016.

[69]   J. Puigdollers, C. Voz, A. Orpella, I. Martin, M. Vetter, and R. Alcubilla, "Pentacene thin-films obtained by thermal evaporation in high vacuum," *Thin Solid Films*, vol. 427, no. 1–2, pp. 367–370, 2003.

[70]   J. B. Johnson, H. Jones, B. S. Latham, J. D. Parker, R. D. Engelken, and C. Barber, "Optimization of photoconductivity in vacuum-evaporated tin sulfide thin films," *Semicond. Sci. Technol.*, vol. 14, no. 6, p. 501, 1999.

[71]   D. M. Mattox, *Handbook of physical vapor deposition (PVD) processing*. William Andrew, 2010.

[72]   A. H. (Arthur H. Lefebvre, *Atomization and sprays*. Hemisphere Pub. Corp, 1989.

[73]   F. Loghin *et al.*, "Scalable spray deposition process for highly uniform and reproducible CNT-TFTs," *Flex. Print. Electron.*, vol. 1, no. 4, p. 45002, 2016.

[74]   M. Bobinger, D. Angeli, S. Colasanti, P. La Torraca, L. Larcher, and P. Lugli, "Infrared, transient thermal, and electrical properties of silver nanowire thin films for transparent heaters and energy-efficient coatings," *Phys. status solidi*, vol. 214, no. 1, p. 1600466, Jan. 2017.

[75]   A. Abdelhalim, M. Winkler, F. Loghin, C. Zeiser, P. Lugli, and A. Abdellah, "Highly sensitive and selective carbon nanotube-based gas sensor arrays functionalized with different metallic nanoparticles," *Sensors Actuators, B Chem.*, vol. 220, 2015.

[76]   A. M. Munzer *et al.*, "Back-gated spray-deposited carbon nanotube thin film transistors operated in electrolytic solutions: an assessment towards future biosensing applications," *J. Mater. Chem. B*, vol. 1, no. 31, pp. 3797–3802, 2013.

[77]   K. X. Steirer *et al.*, "Ultrasonic spray deposition for production of organic solar cells," *Sol. Energy Mater. Sol. Cells*, vol. 93, no. 4, pp. 447–453, Apr. 2009.

[78]   A. Abdellah, B. Fabel, P. Lugli, and G. Scarpa, "Spray deposition of organic semiconducting thin-films: Towards the fabrication of arbitrary shaped organic electronic devices," *Org. Electron.*, vol. 11, no. 6, pp. 1031–1038, Jun. 2010.

[79]   A. Falco, L. Cinà, G. Scarpa, P. Lugli, and A. Abdellah, "Fully-Sprayed and Flexible Organic Photodiodes with Transparent Carbon Nanotube Electrodes," *ACS Appl. Mater. Interfaces*, vol. 6, no. 13, pp. 10593–10601, Jul. 2014.

[80]   T. Hertel, R. E. Walkup, and P. Avouris, "Deformation of carbon nanotubes by surface van

der Waals forces," *Phys. Rev. B*, vol. 58, no. 20, p. 13870, 1998.

[81]   G. Buh, J. Hwang, and E. Jeon, "On-chip electrical breakdown of metallic nanotubes for mass fabrication of carbon-nanotube-based electronic devices," *Nanotechnology, IEEE*, vol. 7, no. 5, pp. 624–627, 2008.

[82]   P. G. Collins, M. S. Arnold, and P. Avouris, "Engineering Carbon Nanotubes and Nanotube Circuits Using Electrical Breakdown," *Science (80-.).*, vol. 292, no. 5517, pp. 706–709, 2001.

[83]   M. S. Strano *et al.*, "The Role of Surfactant Adsorption during Ultrasonication in the Dispersion of Single-Walled Carbon Nanotubes," *J. Nanosci. Nanotechnol.*, vol. 3, no. 1–1, pp. 81–86.

[84]   L. Hu, D. S. Hecht, and G. Grüner, "Carbon nanotube thin films: fabrication, properties, and applications.," *Chem. Rev.*, vol. 110, no. 10, pp. 5790–844, Oct. 2010.

[85]   E. J. Weydemeyer, A. J. Sawdon, and C.-A. Peng, "Controlled cutting and hydroxyl functionalization of carbon nanotubes through autoclaving and sonication in hydrogen peroxide," *Chem. Commun.*, vol. 51, no. 27, pp. 5939–5942, 2015.

[86]   T. Premkumar, R. Mezzenga, and K. E. Geckeler, "Carbon nanotubes in the liquid phase: addressing the issue of dispersion," *Small*, vol. 8, no. 9, pp. 1299–1313, 2012.

[87]   A. Abdellah, "Scalable Thin-Film Manufacturing Technologies for Organic Electronics Alaa Abdellah Doktor-Ingenieurs," 2012.

[88]   W. H. Duan, Q. Wang, and F. Collins, "Dispersion of carbon nanotubes with SDS surfactants: a study from a binding energy perspective," *Chem. Sci.*, vol. 2, no. 7, pp. 1407–1413, 2011.

[89]   A. Abdellah, A. Yaqub, and C. Ferrari, "Spray deposition of highly uniform CNT films and their application in gas sensing," *... (IEEE-NANO), 2011 ...*, pp. 1118–1123, 2011.

[90]   A. Abdellah *et al.*, "Flexible carbon nanotube based gas sensors fabricated by large-scale spray deposition," *IEEE Sens. J.*, vol. 13, no. 10, pp. 4014–4021, 2013.

[91]   F. Loghin, A. Rivadeneyra, M. Becerer, P. Lugli, and M. Bobinger, "A Facile and Efficient Protocol for Preparing Residual-Free Single-Walled Carbon Nanotube Films for Stable Sensing Applications," *Nanomaterials*, vol. 9, no. 3, p. 471, 2019.

[92]   T. Heinze and A. Koschella, "Carboxymethyl ethers of cellulose and starch–a review," in *Macromolecular Symposia*, 2005, vol. 223, no. 1, pp. 13–40.

[93]   S. Kundu, Y. Wang, W. Xia, and M. Muhler, "Thermal stability and reducibility of oxygen-containing functional groups on multiwalled carbon nanotube surfaces: a quantitative high-resolution XPS and TPD/TPR study," *J. Phys. Chem. C*, vol. 112, no. 43, pp. 16869–16878, 2008.

[94]   V. Datsyuk *et al.*, "Chemical oxidation of multiwalled carbon nanotubes," *Carbon N. Y.*, vol. 46, no. 6, pp. 833–840, 2008.

[95]   M. Seifert *et al.*, "Role of grain boundaries in tailoring electronic properties of polycrystalline graphene by chemical functionalization," *2D Mater.*, vol. 2, no. 2, p. 24008, 2015.

[96]   S. W. Knipe, J. R. Mycroft, A. R. Pratt, H. W. Nesbitt, and G. M. Bancroff, "X-ray photoelectron spectroscopic study of water adsorption on iron sulphide minerals," *Geochim.*

Cosmochim. Acta, vol. 59, no. 6, pp. 1079–1090, 1995.

[97] S. Reiche *et al.*, "Reactivity of mesoporous carbon against water–An in-situ XPS study," *Carbon N. Y.*, vol. 77, pp. 175–183, 2014.

[98] D.-W. S. and J. H. L. and Y.-H. K. and S. M. Y. and S.-Y. P. and J.-B. Yoo, "A role of HNO 3 on transparent conducting film with single-walled carbon nanotubes," *Nanotechnology*, vol. 20, no. 47, p. 475703, 2009.

[99] U. Dettlaff-Weglikowska *et al.*, "Effect of SOCl2 Treatment on Electrical and Mechanical Properties of Single-Wall Carbon Nanotube Networks," *J. Am. Chem. Soc.*, vol. 127, no. 14, pp. 5125–5131, Apr. 2005.

[100] E. G. Gamaly and A. V Rode, "Physics of ultra-short laser interaction with matter: From phonon excitation to ultimate transformations," *Prog. Quantum Electron.*, vol. 37, no. 5, pp. 215–323, 2013.

[101] R. Le Harzic *et al.*, "Comparison of heat-affected zones due to nanosecond and femtosecond laser pulses using transmission electronic microscopy," *Appl. Phys. Lett.*, vol. 80, no. 21, pp. 3886–3888, 2002.

[102] P. B. Corkum, F. Brunel, N. K. Sherman, and T. Srinivasan-Rao, "Thermal response of metals to ultrashort-pulse laser excitation," *Phys. Rev. Lett.*, vol. 61, no. 25, p. 2886, 1988.

[103] M. Spellauge *et al.*, "Ultra-short-pulse laser ablation and modification of fully sprayed single walled carbon nanotube networks," *Carbon N. Y.*, vol. 138, pp. 234–242, 2018.

[104] J. M. Liu, "Simple technique for measurements of pulsed Gaussian-beam spot sizes," *Opt. Lett.*, vol. 7, no. 5, pp. 196–198, 1982.

[105] P. A. Danilov *et al.*, "Femtosecond laser ablation of single-wall carbon nanotube-based material," *Laser Phys. Lett.*, vol. 11, no. 10, p. 106101, 2014.

[106] S. X. Guo and A. Ben-Yakar, "Femtosecond laser nanoablation of glass in the near-field of single wall carbon nanotube bundles," *J. Phys. D. Appl. Phys.*, vol. 41, no. 18, p. 185306, 2008.

[107] S. Rapp, M. Domke, M. Schmidt, and H. P. Huber, "Physical mechanisms during fs laser ablation of thin SiO2 films," *Phys. Procedia*, vol. 41, pp. 734–740, 2013.

[108] S. Hermann, N.-P. Harder, R. Brendel, D. Herzog, and H. Haferkamp, "Picosecond laser ablation of SiO 2 layers on silicon substrates," *Appl. Phys. A*, vol. 99, no. 1, pp. 151–158, 2010.

[109] F. Loghin *et al.*, "Scalable spray deposition process for highly uniform and reproducible CNT-TFTs," *Flex. Print. Electron.*, vol. 1, no. 4, p. 045002, Dec. 2016.

[110] C. A. Furtado, U. J. Kim, H. R. Gutierrez, L. Pan, E. C. Dickey, and P. C. Eklund, "Debundling and dissolution of single-walled carbon nanotubes in amide solvents," *J. Am. Chem. Soc.*, vol. 126, no. 19, pp. 6095–6105, 2004.

[111] A. Peigney, C. Laurent, E. Flahaut, R. R. Bacsa, and A. Rousset, "Specific surface area of carbon nanotubes and bundles of carbon nanotubes," *Carbon N. Y.*, vol. 39, no. 4, pp. 507–514, 2001.

[112] Y. Murakami, E. Einarsson, T. Edamura, and S. Maruyama, "Polarization dependent optical absorption properties of single-walled carbon nanotubes and methodology for the evaluation of their morphology," *Carbon N. Y.*, vol. 43, no. 13, pp. 2664–2676, 2005.

[113] S. H. Jeong, K. K. Kim, S. J. Jeong, K. H. An, S. H. Lee, and Y. H. Lee, "Optical absorption spectroscopy for determining carbon nanotube concentration in solution," *Synth. Met.*, vol. 157, no. 13–15, pp. 570–574, 2007.

[114] C. Kerse *et al.*, "Ablation-cooled material removal with ultrafast bursts of pulses," *Nature*, vol. 537, no. 7618, p. 84, 2016.

[115] Z. Sun, M. Lenzner, and W. Rudolph, "Generic incubation law for laser damage and ablation thresholds," *J. Appl. Phys.*, vol. 117, no. 7, p. 73102, 2015.

[116] F. Di Niso, C. Gaudiuso, T. Sibillano, F. P. Mezzapesa, A. Ancona, and P. M. Lugarà, "Role of heat accumulation on the incubation effect in multi-shot laser ablation of stainless steel at high repetition rates," *Opt. Express*, vol. 22, no. 10, pp. 12200–12210, 2014.

[117] R. N. Oosterbeek, C. Corazza, S. Ashforth, and M. C. Simpson, "Effects of dopant type and concentration on the femtosecond laser ablation threshold and incubation behaviour of silicon," *Appl. Phys. A*, vol. 122, no. 4, p. 449, 2016.

[118] N. Souza, M. Zeiger, V. Presser, and F. Mücklich, "In situ tracking of defect healing and purification of single-wall carbon nanotubes with laser radiation by time-resolved Raman spectroscopy," *RSC Adv.*, vol. 5, no. 76, pp. 62149–62159, 2015.

[119] P. Corio, P. S. Santos, M. A. Pimenta, and M. S. Dresselhaus, "Evolution of the molecular structure of metallic and semiconducting carbon nanotubes under laser irradiation," *Chem. Phys. Lett.*, vol. 360, no. 5–6, pp. 557–564, 2002.

[120] A. H. Romero, M. E. Garcia, F. Valencia, H. Terrones, M. Terrones, and H. O. Jeschke, "Femtosecond laser nanosurgery of defects in carbon nanotubes," *Nano Lett.*, vol. 5, no. 7, pp. 1361–1365, 2005.

[121] N. Patil *et al.*, "Wafer-scale growth and transfer of aligned single-walled carbon nanotubes," *IEEE Trans. Nanotechnol.*, vol. 8, no. 4, pp. 498–504, 2009.

[122] W. S. Bacsa, A. Chatelain, T. Gerfin, R. Humphrey-Baker, L. Forro, and D. Ugarte, "Aligned carbon nanotube films: production and optical and electronic properties," *Science (80-.).*, vol. 268, no. 5212, pp. 845–847, 1995.

[123] S. D. Brotherton, *Introduction to Thin Film Transistors*. 2013.

[124] S. Ilani and P. L. McEuen, "Electron Transport in Carbon Nanotubes," *Annu. Rev. Condens. Matter Phys.*, vol. 1, no. 1, pp. 1–25, 2010.

[125] M. S. Purewal, B. H. Hong, A. Ravi, B. Chandra, J. Hone, and P. Kim, "Scaling of resistance and electron mean free path of single-walled carbon nanotubes," *Phys. Rev. Lett.*, vol. 98, no. 18, pp. 2–5, 2007.

[126] C. Zhou, J. Kong, and H. Dai, "Electrical measurements of individual semiconducting single-walled carbon nanotubes of various diameters," *Appl. Phys. Lett.*, vol. 76, no. 12, pp. 1597–1599, 2000.

[127] H. Klauk, "Organic thin-film transistors," *Chem. Soc. Rev.*, vol. 39, no. 7, pp. 2643–2666,

2010.

[128] F. Loghin *et al.*, "Scalable spray deposition process for highly uniform and reproducible CNT-TFTs," *Flex. Print. Electron.*, vol. 1, no. 4, 2016.

[129] J. Li, P. C. Ma, W. S. Chow, C. K. To, B. Z. Tang, and J. Kim, "Correlations between percolation threshold, dispersion state, and aspect ratio of carbon nanotubes," *Adv. Funct. Mater.*, vol. 17, no. 16, pp. 3207–3215, 2007.

[130] T.-J. Ha, K. Chen, S. Chuang, K. M. Yu, D. Kiriya, and A. Javey, "Highly uniform and stable n-type carbon nanotube transistors by using positively charged silicon nitride thin films.," *Nano Lett.*, vol. 15, no. 1, pp. 392–7, 2015.

[131] C. Wang *et al.*, "Device study, chemical doping, and logic circuits based on transferred aligned single-walled carbon nanotubes," *Appl. Phys. Lett.*, vol. 93, no. 3, p. 33101, 2008.

[132] D. D. Freeman, K. Choi, and C. Yu, "N-type thermoelectric performance of functionalized carbon nanotube-filled polymer composites," *PLoS One*, vol. 7, no. 11, p. e47822, 2012.

[133] Z. Li *et al.*, "Polymer functionalized n-type single wall carbon nanotube photovoltaic devices," *Appl. Phys. Lett.*, vol. 96, no. 3, p. 033110, 2010.

[134] L. Petti *et al.*, "Metal oxide semiconductor thin-film transistors for flexible electronics," *Appl. Phys. Rev.*, vol. 3, no. 2, p. 021303, Jun. 2016.

[135] N. Munzenrieder, K. H. Cherenack, and G. Troster, "The effects of mechanical bending and illumination on the performance of flexible IGZO TFTs," *IEEE Trans. Electron Devices*, vol. 58, no. 7, pp. 2041–2048, 2011.

[136] J. Lee *et al.*, "42.2: World's Largest (15-inch) XGA AMLCD Panel Using IGZO Oxide TFT," in *SID Symposium Digest of Technical Papers*, 2008, vol. 39, no. 1, pp. 625–628.

[137] J. S. Lee, S. Chang, S.-M. Koo, and S. Y. Lee, "High-Performance a-IGZO TFT With $\hbox{ZrO}_{2}$ Gate Dielectric Fabricated at Room Temperature," *IEEE electron device Lett.*, vol. 31, no. 3, pp. 225–227, 2010.

[138] N. Munzenrieder *et al.*, "Flexible a-IGZO TFT amplifier fabricated on a free standing polyimide foil operating at 1.2 MHz while bent to a radius of 5 mm," in *2012 International Electron Devices Meeting*, 2012, p. 5.2.1-5.2.4.

[139] L. Petti *et al.*, "Integration of solution-processed (7,5) SWCNTs with sputtered and spray-coated metal oxides for flexible complementary inverters," in *2014 IEEE International Electron Devices Meeting*, 2014, p. 26.4.1-26.4.4.

[140] L. Petti *et al.*, "Integration of Solution-Processed (7,5) SWCNTs with Sputtered and Spray-Coated Metal Oxides for Flexible Complementary Inverters," *Electron Devices Meet. (IEDM), 2014 IEEE Int.*, p. 26.4.1-26.4.4, 2014.

[141] L. Petti *et al.*, "Gain-Tunable Complementary Common-Source Amplifier Based on a Flexible Hybrid Thin-Film Transistor Technology," *IEEE Electron Device Lett.*, vol. 38, no. 11, 2017.

[142] N. Münzenrieder *et al.*, "Contact resistance and overlapping capacitance in flexible sub-micron long oxide thin-film transistors for above 100 MHz operation," *Appl. Phys. Lett.*, vol. 105, no. 26, p. 263504, Dec. 2014.

[143] J. Kong, "Nanotube Molecular Wires as Chemical Sensors," *Science (80-.).*, vol. 287, no. 5453, pp. 622–625, Jan. 2000.

[144] L. C. Wang *et al.*, "A single-walled carbon nanotube network gas sensing device," *Sensors*, vol. 11, no. 8, pp. 7763–7772, 2011.

[145] J. Zhao, A. Buldum, J. Han, and J. P. Lu, "Gas molecule adsorption in carbon nanotubes and nanotube bundles," *Nanotechnology*, vol. 13, no. 2, p. 195, 2002.

[146] T. Yamada, "Modeling of carbon nanotube Schottky barrier modulation under oxidizing conditions," *Phys. Rev. B - Condens. Matter Mater. Phys.*, vol. 69, no. 12, pp. 2–9, 2004.

[147] P. Bondavalli, P. Legagneux, D. Pribat, A. Balan, and S. Nazeer, "Gas fingerprinting using carbon nanotubes transistor arrays," *J. Exp. Nanosci.*, vol. 3, no. 4, pp. 347–356, 2008.

[148] A. Abdelhalim, A. Abdellah, G. Scarpa, and P. Lugli, "Metallic nanoparticles functionalizing carbon nanotube networks for gas sensing applications," *Nanotechnology*, vol. 25, no. 5, p. 55208, 2014.

[149] F. Loghin, A. Abdellah, A. Falco, M. Becherer, P. Lugli, and A. Rivadeneyra, "Time stability of carbon nanotube gas sensors," *Measurement*, vol. 136, pp. 323–325, 2019.

[150] L. Hu, D. Hecht, and G. Gruner, "Carbon nanotube thin films: Fabrication, properties, and applications," *Chem. Rev.*, 2010.

[151] E. Cagatay, A. Falco, A. Abdellah, and P. Lugli, "Carbon nanotube based temperature sensors fabricated by large-scale spray deposition," in *Microelectronics and Electronics (PRIME), 2014 10th Conference on Ph. D. Research in*, 2014, pp. 1–4.

[152] Z. Li *et al.*, "Recent Advances in Pen-Based Writing Electronics and their Emerging Applications," *Adv. Funct. Mater.*, vol. 26, no. 2, pp. 165–180, Jan. 2016.

[153] N. Dossi, R. Toniolo, E. Piccin, S. Susmel, A. Pizzariello, and G. Bontempelli, "Pencil-Drawn Dual Electrode Detectors to Discriminate Between Analytes Comigrating on Paper-Based Fluidic Devices but Undergoing Electrochemical Processes with Different Reversibility," *Electroanalysis*, vol. 25, no. 11, pp. 2515–2522, Nov. 2013.

[154] N. Kurra, D. Dutta, and G. U. Kulkarni, "Field effect transistors and RC filters from pencil-trace on paper," *Phys. Chem. Chem. Phys.*, vol. 15, no. 21, pp. 8367–8372, 2013.

[155] K. A. Mirica, J. M. Azzarelli, J. G. Weis, J. M. Schnorr, and T. M. Swager, "Rapid prototyping of carbon-based chemiresistive gas sensors on paper," *Proc. Natl. Acad. Sci.*, vol. 110, no. 35, p. E3265 LP-E3270, Aug. 2013.

[156] H. T. Mitchell *et al.*, "Reagent pencils: a new technique for solvent-free deposition of reagents onto paper-based microfluidic devices," *Lab Chip*, vol. 15, no. 10, pp. 2213–2220, 2015.

[157] J.-W. Han, B. Kim, J. Li, and M. Meyyappan, "Carbon nanotube ink for writing on cellulose paper," *Mater. Res. Bull.*, vol. 50, pp. 249–253, 2014.

[158] A. J. Bandodkar, W. Jia, J. Ramírez, and J. Wang, "Biocompatible Enzymatic Roller Pens for Direct Writing of Biocatalytic Materials: 'Do-it-Yourself' Electrochemical Biosensors," *Adv. Healthc. Mater.*, vol. 4, no. 8, pp. 1215–1224, Jun. 2015.

[159] A. Albrecht, A. Rivadeneyra, A. Abdellah, P. Lugli, and J. F. Salmerón, "Inkjet printing and

photonic sintering of silver and copper oxide nanoparticles for ultra-low-cost conductive patterns," *J. Mater. Chem. C*, vol. 4, no. 16, pp. 3546–3554, Apr. 2016.

[160] F. C. Loghin *et al.*, "A Handwriting Method for Low-Cost Gas Sensors," *ACS Appl. Mater. Interfaces*, vol. 10, no. 40, pp. 34683–34689, 2018.

[161] P. Lugli *et al.*, "Fabrication, characterization and modeling of flexible electronic components based on CNT networks," *Proc. - IEEE Int. Symp. Circuits Syst.*, vol. 2016–July, pp. 1362–1365, 2016.

[162] A. Falco, A. Rivadeneyra, F. C. Loghin, J. F. Salmeron, P. Lugli, and A. Abdelhalim, "Towards low-power electronics: self-recovering and flexible gas sensors," *J. Mater. Chem. A*, vol. 6, no. 16, pp. 7107–7113, 2018.

Publications

2019

- **Loghin, F.; Rivadeneyra, A.; Becherer, M.; Lugli, P.; Marco Bobinger, M.:** A Facile and Efficient Protocol for Preparing Residual-Free Single-Walled Carbon Nanotube Films for Stable Sensing Applications. **Nanomaterials** 2019, 9(3), 471 2019-03, 2019

- **Loghin, F.; Abdellah, A.; Falco, A.; Becherer, M.; Lugli, P.; Rivadeneyra, A.:** Time stability of carbon nanotube gas sensors. **Measurement** Volume 136, March 2019, Pages 323-325 2019-03, 2019

2018

- **Albrecht, A.; Rivadeneyra, A.; Bobinger, M.; Bonaccini Calia, J.; Loghin, F.; Salmeron , J.; Becherer, M.; Lugli, P.; Falco, A.:** Scalable Deposition of Nanomaterial-Based Temperature Sensors for Transparent and Pervasive Electronics. **Journal of Sensors** Volume 2018, Article ID 7102069 2018-10, 2018,

- **Bobinger, M.; Hinterleuthner, S.; Loch, M.; Albrecht, A.; Loghin, F.; Mock, J.; Rivadeneyra, A.; Becherer, M.; Keddis, S.; Schwesinger, N.; Lugli, P.:** Thermal and Mechanical Energy Harvesting based on PVDF. 8. MSE Kolloquium 2018 Advances in Energy Transition 2018, Munich School of Engineering TUM MSE, 201819 July 2018, München Garching, Germany 2018-07

- **Falco, A.; Lugli, P.; Loghin, F.; Rivadeneyra, A.; Larcher, L.; Bertacchini, A.:** Design and Simulation of Out-of-Plane Nanomaterial-Based Thermocouples. Proceedings of ALLSENSOR 2018 Conference, The Third International Conference on Advances in Sensors, Actuators, Metering and Sensing, IARIA, 2018 Rome, Italy, 25-29 Mar 2018 2018-03

- **Falco, A.; Rivadeneyra, A.; Loghin, F.C.; Salmerón, J.F.; Lugli, P.; Abdelhalim, A.:** Towards Low-Power Electronics: Self-Recovering and Flexible Gas Sensors. **Journal of Materials Chemistry A**, J. Mater. Chem. A. 2018 2018-03, 2018

- **Ivanovskaia, A.; Maier, A.; Loghin, F.; Becherer, M.; Albrecht, A.:** High–resolution, Screen–printed Interdigitated Electrodes for Biosensors and Gas Sensors. LOPEC 2018, Munich, 2018, 2018 München, Germany, 19-21 Mar 2018 2018-03

- **Loch, M.; Albrecht, A.; Bobinger, M.; Loghin, F.; Becherer, M.; Lugli, P.; Rivadeneyra-Torres,A.:** Cost-effective fabrication techniques for organic solar cells. 8. MSE Kolloquium 2018 Advances in Energy Transition 2018, Munich School of Engineering TUM MSE, 201819 July 2018, München Garching, Germany 2018-07

- **Loch, M.; Loghin, F.; Baghvand, K.; Lugli, P.; Becherer, M.:** Fully sprayed, ITO-free, flexible organic solar cells. DPG Verhandlungen DS: Fachverband Dünne Schichten DS 6: Thin Film Applications DS 6.3: Vortrag, Deutsche Physikalische Gesellschaft DPG, 2018Berlin, Germany, 14 Mar 2018 2018-03

- **Loghin, F.; Falco, A.; Bobinger, M.; Abdellah, A.; Becherer, M.; Lugli, P.; Rivadeneyra, A.:** Large-scale spray deposition of carbon nanotube-based thin-film devices. DPG-Verhandlungen DS: Fachverband Dünne Schichten DS 17: Poster Session I DS 17.61: Poster B, 2018Berlin, Germany, 14 Mar 2018 2018-03

- **Loghin, F.; Falco, A.; Albrecht, A.; Salmeron, J.F.; Becherer, M.; Lugli, P.; Rivadeneyra, A.:** A handwriting method for low-cost gas sensors. **ACS Appl. Mater. Interfaces**, ACS Applied Materials & Interfaces. Surfaces, Interfaces, and Applications 2018-09, 2018, 34

- **Rivadeneyra, A.; Loghin, F.; Falco, A.:** Technological Integration in Printed Electronics. In: Flexible Electronics, Chapter 5 2018-08. InTech Open, 2018

- **Spellauge, M.; Loghin, F.; Sotrop, J.; Domke, M.; Bobinger, M.; Alaa Abdellah, A.; Becherer, M.; Lugli, P.; Huber, H.P.:** Ultra-short-pulse laser ablation and modification of fully sprayed single walled carbon nanotube networks. **Carbon**, 2018-06, 2018

- **Vela-Cano, M.; Salmerón, J.F.; Rivadeneyra, M.A.; Loghin, F.; Becherer, M.; Gonzalez-Lopez, J.; Rivadeneyra, A.:** CO_2 sensor based on Carbon Nanotubes for detection of lactose fermentation. 11th International Symposium on Flexible Organic Electronics (ISFOE2018), 2018Thessaloniki, Greece, 02-05 July 2018 2018-07

2017

- **Albrecht, A.; Bobinger, M.; Bonaccini Calia, J.; Falco, A.; Loghin, F.; Rivadeneyra, A.; Becherer, M.; Lugli, P.:** Transparent thermocouples based on spray-coated nanocomposites. **SENSORS**, 2017 IEEE 2017-10, IEEE Xplore Digital Library, 2017 Glasgov Scotland UK, 29 Oct - 01 Nov 2017

- **Falco, A.; Lugli, P.; Loghin, F.; Bobinger, M. ; Gerlt, M.:** Spray deposition of polymeric thin-films for the inline encapsulation of organic photodiodes. Nanotechnology (IEEE-NANO), 2017 IEEE 17th International Conference on, IEEE Xplore Digital Library, 2017Pittsburgh PA USA, 25-28 July 2017 2017-07

- **Falco, A.; Salmerón, J.F.; Loghin, F.; Lugli, P.; Rivadeneyra, A.:** Fully Printed Flexible Single-Chip RFID Tag with Light Detection Capabilities**. Sensors** 2017, 17(3), 534 2017-03, 2017, 1-12

- **Petti, L.; Loghin, F.; Cantarella, G.; Vogt, C.; Münzenrieder, N.; Abdellah, A.; Becherer, M.; Haeberle, T.; Daus, A.; Salvatore, G.; Tröster, G.; Lugli, P.:** Gain-Tunable Complementary Common-Source Amplifier based on a Flexible Hybrid Thin-Film Transistor Technology. **IEEE Electron Device Letters** (Volume: PP, Issue: 99) 2017-09, 2017, 1-1

2016

- **Abdelhalim, A.; Falco, A.; Loghin, F.; Lugli, P.; Salmerón, J.F.; Rivadeneyra, A.:** Flexible NH3 sensor based on spray deposition and inkjet printing. **SENSORS**, 2016 IEEE, IEEE Xplore Digital Library, 2016 Orlando FL USA, 30 Oct-03 Nov 2016 2016-11

- **Colasanti, S.; Robbiano, V.; Loghin, F.C.; Abdelhalim, A.; Bhatt, V.D.; Abdellah, A.; Cacialli, F.; Lugli, P.:** Experimental and Computational Study on the Temperature Behavior of CNT Networks. **IEEE Transactions on Nanotechnology** (Volume:15 , Issue: 2) 2016-03, 2016, 171-178

- **Falco, A.; Salmerón, J.F.; Loghin, F.; Abdelhalim, A.; Lugli, P.; Rivadeneyra, A.:** Optimization of process parameters for inkjet printing of CNT random networks on flexible substrates. Nanotechnology (IEEE-NANO), 2016 IEEE 16th International Conference on, IEEE Xplore Digital Library, 2016Sendai, Japan, 22-25 Aug 2016 - 2016-11

- **Loghin, F.; Colasanti, S.; Weise, A.; Falco, A.; Abdelhalim, A.; Lugli, P.; Abdellah, A.:** Scalable spray deposition process for highly uniform and reproducible CNT-TFTs. **Flexible and Printed Electronics**, Volume 1, Number 4 1 (2016) 045002 2016-12, 2016

- **Lugli, P.; Abdellah, A.; Abdelhalim, A.; Albrecht, A.; Becherer, M.; Cagatay, E.; Colasanti, S.; Falco, A.; Loghin, F.; El-Molla, S.; Fernández Salméron, J.; Rivadeneyra, A.:** Fabrication, characterization and modeling of flexible electronic components based on CNT networks. Circuits and Systems (ISCAS), 2016 IEEE International Symposium on, IEEE Xplore Digital Library, 2016Montreal, Canada, 22-25 May 2016 2016-05

2015

- **Abdelhalim, A.; Loghin, F.; Winkler, M.; Zeiser, C.; Abdellah, A; Lugli, P.:** Carbon nanotube based gas sensor arrays on rigid and flexible substrates. Proceedings of the IEEE **SENSORS** 2015, IEEE Xplore Digital Library, 2015Busan, China, 01-04 Nov 2015 2015-11

- **Abdelhalim, A.; Winkler, M.; Loghin, F.; Zeiser, C.; Lugli, P.; Abdellah, A.:** Highly Sensitive and Selective Carbon nanotube-Based Gas Sensor Arrays Functionalized with Different Metallic Nanoparticles. **Sensors and Actuators B**: Chemical 220 2015-07 , 2015, 1288--1296

- **Colasanti, S.; Loghin, F. C.; Bhatt, V. D.; Abdellah, A.; Lugli, P.; Robbiano, V.; Cacialli, F.:** Experimental and computational study on the temperature behavior of CNT networks. Nanotechnology (IEEE-NANO) , 2015 IEEE 15th International Conference on 15, IEEE Xplore Digital Library, 2015Rome, Italy, 27-30 July 2015 2015-07

- **Haeberle, T.; Loghin, F.; Zschieschang, U.; Klauk, H.; Lugli, P.:** Carbon nanotube thin-film transistors featuring transfer-printed metal electrodes and a thin, self-grown aluminum oxide gate dielectric. Nanotechnology (IEEE-NANO) , 2015 IEEE 15th International Conference on , IEEE Xplore Digital Library, 2015Rome, Italy, 27-30 July 2015 2015-07

Acknowledgements

I would like to thank Prof. Paolo Lugli for the great opportunity and trust given to work with him and at the institute from my Bachelor days up until the finalization of this thesis. His continuous interest and support contributed to the success of the work presented here.

Prof. Dr.-Ing. habil. Markus Becherer, Thank you for your support and patience.

I want to thank my mentor, Dr. Ing. Alaa Abdellah, who took me in under his wing while I was a young lost bachelor student and has provided me with so much more than these short words could ever adequately describe. Thank you for being a fantastic mentor and an even better friend.

I want to thank my collaboration partners: Prof. Dr. Heinz P. Huber & Maximilian Spellauge at the Laserzentrum München and Prof. Tröster and Dr. Luisa Petti at ETH.

The office of the month: Dr. Ing Ahmed and Dr. Ing Aniello. Fantastic friends and colleagues. Our time in the office and more importantly outside, while not always productive will forever remain one of my fondest memories.

My friends from Granada: Pepe, Almu and Carlotta. Thank you for always motivating me especially Almu.

I want to thank Lucia, Katrin and Susi, for making my life easier while I made yours harder.

I want to thank Rosi for having the patience of an angel while dealing with me and my colleagues in the lab. We tried our best…

I would like to thank the Nano Sauf & Plausch office in Garching: Andy, Marco, Marius, Sepp & Mathias. Schee war's

My colleagues at the Institute that have come and gone during my long time at the institute.

The Herzig Group: Stephan, Oli, Michi & Jenny for their collaboration in the lab, help and support and the good times at the occasional bier.